Cavity-Vacuum System for Enhanced Ultra-Cold Atom Generation

By

Georgina Croft

A thesis submitted to
the University of Birmingham
for the degree of
DOCTOR OF PHILOSOPHY

Cold Atoms Research Group
School of Physics and Astronomy
College of Engineering and Physical Sciences
University of Birmingham
March 2021

ABSTRACT

A design of a proof-of-principle, all-optical method of generating the ultra-cold atoms required for space-based atom interferometry is presented. The system will evaporatively cool in an optical dipole trap (ODT) and employ an optical cavity to enhance the trapping power. This design proposes a novel hybrid single-beam/lattice ODT to reach ultra-cold temperatures, and ideally Bose-Einstein condensates (BECs). This project builds on heritage from the group by employing a compact 'prism MOT' which uses reflective prisms to generate the beams required for magneto-optical trapping (MOT). If successful, this project would demonstrate the first ODT and BEC loaded from a prism MOT. From simulation, a 4 mirror cavity is chosen with a finesse of 2991 which produces an initial ODT depth of 100 mW. This thesis presents the system design including: the cavity and initial building considerations; the vacuum system, the laser system and telescopes, and the magnetic field coils. This system will use only a single laser for all stages of ultra-cold atom generation (2D MOT, 3D MOT, ODT, BEC). This, as well as the compact prism MOT and low power ODT, is advantageous for the Size, Weight and Power of the system which is critical for a space-based experiment.

ACKNOWLEDGMENTS

I would firstly like to acknowledge my supervisor, Prof Kai Bongs, who provided helpful information and insights into the world of Quantum Technology. I would also like to thank the European Space Agency for funding my research and for selecting me to be the first ESA Networking/Partnering Initiative PhD student based in the UK. I owe my gratitude to the staff at RAL Space who were very welcoming whilst I was there on secondment. Specifically to my quantum colleague, Heleri Ramler: I really enjoyed our time working together and hold your one of a kind approach to physics and life in high regard. I would also like to add a special thanks to Stephen Brookes, Anthony Barnes and the other engineers from the mechanical workshop whose exceptional knowledge and willingness to share it was invaluable to the project.

Furthermore, I am grateful to the other PhD students in the School of Physics and Astronomy who provided me with a supportive community of like-minded people. Specifically Jonathan Bass, who has been with me on my entire physics journey, and Megan Grose, whose comedy stylings kept me going on many occasions. I would like to thank my parents, who funded my initial pursuits of physics and have always believed in me. As well as all the pets that have helped me along the way with much needed distractions at hard times.

Most of all I would like to thank Luuk Earl, a worthy partner in both physics and life.

CONTENTS

List of Figures **vi**

List of Tables **vii**

1 Introduction **1**

1.1 Gravimetry 2

1.1.1 Quantum Gravimetry 3

1.2 Gravimetry in Space 5

1.2.1 Earth Observation 6

1.2.2 Quantum Gravimeters in Space 9

2 Scientific Background **16**

2.1 Gravimetry: Atom Interferometry 16

2.1.1 Rabi Oscillations 17

2.1.2 The Atom Interferometry Sequence 18

2.1.3 Gravimetry & Sensitivity 19

2.2 Ultra-Cold Atom Sample Preparation 25

2.2.1 The Magneto-Optical Trap 25

2.2.2 The Optical Dipole Trap 38

2.2.3 Evaporative Cooling 53

2.2.4 Bose-Einstein Condensates 56

2.3 Summary of the Experimental Cycle 56

2.4 Optical Cavities 57
2.4.1 Cavity Resonance: Finesse & Q-factor 57
2.4.2 Cavity Beam Waist & Stability 60
2.4.3 Transmission, Reflection & Power Enhancement 63
2.4.4 Linear and Ring Cavities 69
2.4.5 Astigmatism 70
2.4.6 Hermite-Gaussian Modes 70
2.4.7 Impedance Matching 71
2.4.8 The Optical Lattice: Standing Waves 73
2.4.9 Atoms in Cavities 73

3 Cavity Design **74**

3.1 Main Design Criteria 74
3.1.1 Criteria 1: Trap Depth 75
3.1.2 Criteria 2: Trap Volume 76
3.2 Cavity in Vacuum 78
3.3 Number and Radius of Curvature of Mirrors 79
3.3.1 Linear vs Ring Cavity 79
3.3.2 Ring Cavity Design Options 80
3.3.3 Cavity Parameter Calculations 80
3.3.4 Atoms Captured in Cavity 85
3.3.5 Predicted Gravity Sensitivity 87
3.4 Cavity Building Considerations 89
3.4.1 Glue Requirements 90
3.4.2 Glue Parameters 91
3.4.3 Glue Selection 93
3.4.4 Suggested Gluing and Alignment Procedure 94

4 System Design **97**

4.1 Vacuum System 97

4.1.1 3D MOT Chamber 99

4.1.2 Prism & Cavity-Mounting Flange 101

4.1.3 Cavity Mount 102

4.1.4 2D MOT Chamber 108

4.1.5 Graphite Tube 111

4.1.6 Pump 113

4.1.7 Atom Interferometry Region 117

4.2 Magnetic Field Generation 117

4.2.1 3D MOT Magnetic Field 118

4.2.2 2D MOT Magnetic Field 122

4.3 Optical Delivery: Laser System & Telescopes 123

4.3.1 Fibre Laser System 123

4.3.2 Telescopes 127

4.4 Full Assembly 130

5 Conclusions **132**

5.1 Project Motivation and Goals 132

5.2 Summary of Work Completed 134

5.3 Future Work 136

References **139**

LIST OF FIGURES

1.1 Data taken by the Gravity Recovery and Climate Experiment (GRACE) mission 7

1.2 Geoid model taken during the Gravity field and steady-state Ocean Circulation Explorer (GOCE) mission 8

2.1 Rabi population oscillations in a two-level atom for several detunings 18

2.2 Atom interferometry sequence 20

2.3 Stimulated two-photon Raman transition for a three-level system 22

2.4 Laser cooling of atoms using red-detuned, counter-propagating beams 27

2.5 Force due to one-dimensional optical molasses 28

2.6 Total field created by σ^+-σ^- beams 30

2.7 Clebsh–Gordan coefficients for a $J_g = 1 \leftrightarrow J_e = 2$ transition . . 31

2.8 Energy level scheme for the D2 line of ^{87}Rb 33

2.9 Magnetic field gradient and counter-propagating beam geometry used in magneto-optical trap (MOT) creation 34

2.10 3D magneto-optical trap (MOT) generation with 6 separate beams vs. reflective prisms 36

2.11 Optical light shifts on a two level atom with red-detuned light . 45

2.12 Three types of optical dipole trap (ODT) 50

2.13 Evaporative cooling process schematic 54
2.14 Theoretical cavity transmission profile 58
2.15 Gaussian beam radial intensity profile 62
2.16 Transmission and reflection equations for a travelling wave bow-tie cavity 63
2.17 4 All-Curved-Mirror (ACM) cavity with beam profiles 65
2.18 Optical cavity modelled as series of lenses 67
2.19 Linear vs ring cavities 69
2.20 $TEM_{n,m}$ resonator modes 72

3.1 Prism and cavity mirror arrangement used to generate the magneto-optical trap (MOT) and optical dipole trap (ODT) . . 77
3.2 Experimental prism magneto-optical trap (MOT) 78
3.3 Ring cavity design options (schematic) 81
3.4 Ring cavity design options (3D CAD) 82

4.1 3D CAD design of the vacuum system 99
4.2 3D magneto-optical trap (MOT) & ultra-cold atom generator vacuum chamber 100
4.3 3D magneto-optical trap (MOT) chamber: port uses 101
4.4 Prism mounting flange 102
4.5 Prism and cavity mounts 103
4.6 Cavity mount 104
4.7 V-groove cavity mirror mounting design 105
4.8 Piezo placement in optical cavity mount 106
4.9 Kinematic mirror mount 109
4.10 Schematic showing the input angle of the 2D magneto-optical trap (MOT) in respect to the cavity mirrors 110

4.11 Graphite tube attachment to 3D magneto-optical trap (MOT) chamber via threading 112
4.12 Vacuum system conductance schematic 114
4.13 3D magneto-optical trap (MOT) simulated magnetic field 119
4.14 3D and 2D magneto-optical trap (MOT) coil mounts 121
4.15 Laser system design 124
4.16 Telescope lens geometry 128
4.17 3D CAD design of the full system assembly 131

LIST OF TABLES

3.1 Ring cavity design options and corresponding parameters. . . . 83

3.2 Cavity mirror reflectivities for undercoupled, overcoupled, and impedance matched cases. 85

3.3 Predicted gravity sensitivity for the system 88

3.4 Specifications of the epoxies considered for cavity building . . . 93

4.1 Piezo options 107

CHAPTER 1

INTRODUCTION

The field of quantum technology and sensing, although still in its early stages, has the potential to have a high impact on industry and society. Much of the work currently being undertaken is towards improving the Technology Readiness Level (TRL) of these quantum systems so that they are capable of working outside of the laboratory in 'real world' environments. This thesis presents the design of a novel proof-of-principle system which, if realised, would enable the relatively low-power and compact generation of the ultra-cold atoms required for space-based gravity sensing (using atom interferometry). First, the applications of measuring gravity in space and the existing classical technology being used to do so is presented in this introductory chapter. Then the advantages of using quantum methods in general and the specific system designed in this thesis are outlined. Note that the reader is not required to fully understand the techniques presented in this introductory chapter as they are used purely to explain the motivation behind the experiment and are explained subsequently in chapter 2. This scientific background chapter makes up a significant proportion of the thesis because it underpins the modelling and simulation that was required to complete the design of the system. Next the designs of the key component of the experiment and the rest of the system are presented in chapters 3 and 4

respectively. Finally, conclusions and the next steps to be taken for a practical realisation of this experimental design are discussed in chapter 5.

1.1 Gravimetry

As one of the four fundamental forces in the universe, gravity interacts with all 'massive' objects. Scientific research into measuring gravity, known as gravimetry, has been conducted for many years. In $\sim$ 1610, Galileo Galilei observed no detectable difference in the time taken for two balls of varying weight to roll down an inclined plane [1]. This was an early test of the universality of free fall. In 1774, Nevil Maskelyne conducted the 'Schiehallion experiment', an iteration of the work of French astronomers from 1738, where the tiny deflection of the vertical of a pendulum's plumb-bob due to the gravitational attraction of a nearby mountain was measured to determine the mean density of the Earth [2]. This value was improved upon in the late 1790s by Henry Cavendish who used two masses suspended from a wire on a torsion balance to make a remarkably sensitive measurement of the Earth's density [3]. The mutual gravitational attraction of the two masses caused the apparatus to rotate, twisting the supporting wire. The rotation stopped when the twisting force of the wire balanced the gravitational force. Since then, his experiment have been reformulated in modern terms to show that Newton's gravitational constant, G, could have been obtained from his results*. Later in 1878, John Henry Poynting performed an iteration of this experiment using an ordinary balance with an adjustable mass to further improve the valuation of G [4].

More recently, increasingly more accurate sensors have been used to measure gravity on a smaller, local scale. Chronologically, these devices include the

*The first reference to Newton's gravitational constant, G, was made $\sim$ 75 years after Cavendish's work.

mass-spring system, superconductors, laser interferometry free-fall, and MEMS * [5–7]. These 'classical gravimeters' have been used to observe important spatial and temporal changes in mass distributions and have enabled the creation of valuable underground gravity maps which have been used in a variety of applications and industries. For example, before the development of seismology, gravimetry was the first geophysical technique used in oil and gas exploration [8]. Although seismology has now become the dominant technique, gravimetry is still invaluable for particular ground compositions [9]. A further field where the use of gravimetry is well-establish is the mining industry where gravity data is widely employed to map subsurface geology and to estimate ore reserves [8]. Another field which is already benefiting, and has further potential to benefit, from gravity measurements is that of environmental monitoring. For example, international networks of gravity sensors have been used, in collaboration, after an earthquake to study how seismic activity attenuates and disperses [10]. Furthermore, there is suggestion that by monitoring regional gravitational anomalies, epicentres of future earthquakes could be predicted [11]. Similarly, monitoring of subsurface magma mass flow could be used to predict volcanic eruptions [12]. Hence, gravimeters have had many valuable uses in industry and society.

1.1.1 Quantum Gravimetry

As valuable as these classical devices have proven to be, they can have fundamental drawbacks or limits. Therefore, quantum technologies (devices that rely on the principles of quantum physics) have been proposed as a candidate for future gravimeter improvements.

In the latter half of the 20th century, the first quantum revolution, or

*MEMS = micro-electromechanical system

'quantum 1.0' took place [13]. This was the development of devices that relied on the effects of quantum, rather than classical, mechanics. Examples include the invention of the transistor and laser, which were respectively awarded the 1956 and 1964 Nobel Prize in Physics. The progression of these, and other, key technologies paved the way for a second quantum revolution, or 'quantum 2.0', which is currently taking place. This involves the creation of technology devices that generally rely on manipulating quantum states of matter and often exploit the quantum principles of superposition and entanglement [14].

As the underlying technologies became sufficiently mature, the feasibility of these quantum devices progressed and many governments, funding bodies, and industries worldwide began to invest in national programmes. One such example is the well-established UK National Quantum Technology Programme which was launched in 2013 and is now in its second stage and has received a total of $>$ £400 million funding commitment over the last 8 years [15]. The key goal of this programme is to use a collaboration between academia, industry, and government, to advance the technology readiness level of quantum devices in the UK to propel them from controlled laboratory conditions to a commercial field environment. The programme is split into four main 'hubs' which are identified as having potential to revolutionise different industries. These hubs are focused on quantum: communications; computing and simulation; enhanced imaging; and sensors and timing (formerly metrology). The potential applications of each respective quantum technology is high impact and varied, ranging from securing sensitive data transmissions such as bank transactions and health records, drastically improving computing processing speeds for large scale problems like facial recognition and mathematical problem solving, developing new medical imaging devices, and providing clocks with unprecedented precision for timing and navigation [16]. Although, all these devices still face some technology and

regulatory challenges on the route to market, quantum sensors, in particular, have made orders of magnitude level improvements in their Size, Weight and Power (SWaP) characteristics over the course of the first national programme and are starting to emerge commercially [17–19].

One example of such devices are cold atom interferometers for gravimetry. Here, a cloud of cooled/slowed atoms acts as a falling test mass to measure the absolute gravity signal. The advantages of this device over classical gravimeters can be exhibited by thinking about the basic principles of a gravimeter. To measure gravity, an object with mass, i.e. an object that experiences the gravitational force, must be monitored. A classical gravimeter uses a macroscopic test mass which could be a pendulum, a mass on a spring, or a falling mirror [20, 21]. These devices typically exhibit mechanical wear over time, require regular re-calibration, and some cannot provide an absolute gravity measurement. On the other hand, quantum gravimeters typically use an atom as the test mass. For example, in the case of atom interferometry, a falling cloud of cold atoms is used to measure the local absolute gravitational acceleration. This presents an immediate advantage over classical systems in that atoms act as an 'ideal' test mass and do not experience drift or wear over time. Hence, an absolute gravimeter can be developed with long term accuracy.

1.2 Gravimetry in Space

Similarly to on ground, there are valuable applications of gravimetry in space. This includes both fundamental physics applications, such as testing of Einstein's equivalence principle [22] or the detection of gravitational waves [23], as well as monitoring the gravitational field of the Earth itself. This latter application, encompassed by the field of Earth observation (EO), is the long-term

motivation for this work.

1.2.1 Earth Observation

Earth observation can be performed by placing a space compatible sensor on a satellite orbiting the Earth on a regular basis. Initially, Earth observation was performed using the transmission or reflection of electromagnetic (EM) waves to or from the Earth* i.e. with visible imaging [24]. Then, the addition of classical gravitational sensing allowed imaging of what is under the Earth's surface, rather than only what is on it. This allows the monitoring of large underground structures including the polar ice caps and the tectonic plates, as well as the development of a dynamic topographical geoid model. The geoid is the gravitational equipotential surface of the Earth that coincides with the mean level of the oceans. An accurate geoid is important as it is the model of the Earth used in climate research and navigation.

The first gravity based Earth observation was done by the Gravity Recovery and Climate Experiment (GRACE), a joint NASA and German Aerospace Center mission, which measured the Earth's gravitational field from launch in 2002 until October 2017. It used microwave ranging to measure the speed and distance between two identical satellites, which varied according to the gravitational pull of the Earth. GRACE measured the entire Earth's gravity field on a 30 day cycle which allowed periodic monitoring of the movement of tectonic plates, the polar ice caps, and large bodies of water [25, 26].

*surface or atmosphere

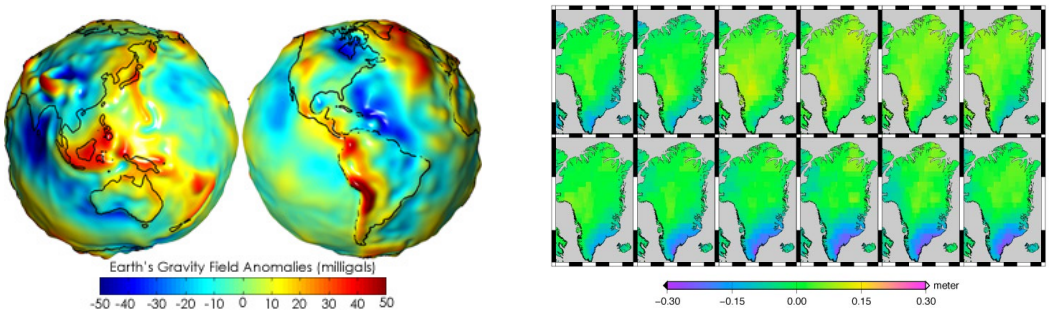

(a) Map of how the Earth's gravity varies from a smooth, featureless model [27].

(b) Monthly change of Greenland's ice sheet where blue indicates the largest mass loss [28].

Figure 1.1: Example data taken by the Gravity Recovery and Climate Experiment (GRACE) mission.

While the data obtained from the GRACE apparatus could measure a variety of gravitational phenomena from space with an unprecedented accuracy of several µGal*, the spatial resolution was of the order of several hundred km [25, 29] (see Figure 1.1). This spatial resolution was improved upon by a European Space Agency (ESA) mission launched in 2009 called Gravity field and steady-state Ocean Circulation Explorer (GOCE). GOCE used gravity gradiometry [30] to measure the geoid of the Earth to a precision on the order of mGal with a spatial resolution of ∼100 km [31] as can be observed in figure 1.2. However, this mission ended in 2013 and did not monitor any time variations in gravity, only the static field.

A GRACE follow on mission (GRACE-FO) launched in early 2018 has continued the work of its predecessor [33]. The design and orbit of the follow-on satellite is similar to the original. The main difference between the two is that, in addition to microwave ranging, GRACE-FO is equipped with lasers to demonstrate laser ranging interferometry (LRI) as a superior method of measuring the distance between the two satellites. This will not be able to

*$1\mu\text{Gal} = 1 \times 10^{-8}\text{ms}^{-2}$, $1\text{g} \sim 9.81\text{ms}^{-2} = 981\text{Gal}$

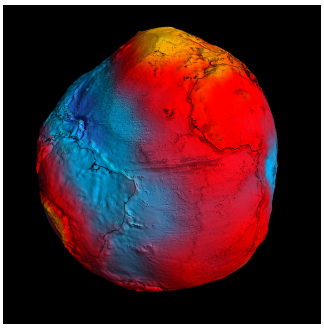

Figure 1.2: Geoid model taken during the Gravity field and steady-state Ocean Circulation Explorer (GOCE) mission. The colours represent the height deviations from a uniform geoid where blue represents negative heights (minimum -100 m) and red represents positive heights (maximum +100 m) [32].

record scientific data in this mission but could be implemented in future ones. The LRI was demonstrated, in 2019, to improve the distance measurement by a factor of ~ 20 compared to GRACE [34], mainly due to the laser wavelength being 10,000 times shorter than the microwave wavelength. This should, in turn, allow for an order of magnitude improvement in the accuracy of the gravity measurement, to $\sim 10^{-7}$ Gal [35]. However, there is no subsequent design to further improve on this precision and hence this mission will then be reaching its limit. Therefore, alternate solutions are being explored for long-term, higher precision Earth observation and quantum gravimeters have been identified as a key future technology by ESA [36, 37].

For completeness, note that other classical space-based accelerometers are in existence for under-the-surface planetary exploration. For example, the 'InSight' mission is currently using a MEMS based seismometer, developed by researchers at Imperial College, on a Mars rover to measure seismic activity and model of the planet's interior [38]. This MEMS sensor can measure accelerations to a sensitivity of 0.3 $\mu\text{Gal}/\sqrt{\text{Hz}}$ *[39] and it has many advantages including its low volume and robustness to vibrations and shock [40, 41]. However, MEMS

*Units of $\text{Gal}/\sqrt{\text{Hz}}$ represent the fact that averaging over multiple measurements can improve the sensitivity.

devices typically experience high levels of drift and hence are not employed as gravimeters without the use of an accompanying absolute sensor used for regular recalibration.

1.2.2 Quantum Gravimeters in Space

The advantages possessed by cold atom interferometry based gravimeters, outlined in section 1.1.1, are crucial in a space environment, where there is a requirement for long term operation and high precision. In fact, these sensors have a further added benefit when they are considered in space as opposed to on ground. This is because the sensitivity of a cold atom gravimeter scales with the square of the interferometry time, labelled T (see section 2.1 for a physical understanding of this parameter). In a microgravity environment, such as space, these T-times can be increased by 1-2 orders of magnitude as compared to a similar sized device on Earth, making the device substantially more sensitive. However, this advantage also creates a fundamental challenge with taking this technology to space: over this extra measurement time, the atom cloud will expand more causing a loss of contrast and ultimately the atoms would leave the measurement area entirely. To counter this process, the atoms must be sufficiently cooled, using techniques more advanced than the typical laser cooling techniques used on ground, to slow the expansion.

Ultra-cold Atom Preparation

Standard cold atom cloud generation uses a combination of lasers and magnetic fields to cool atoms trapped in a magneto-optical trap (MOT) (refer to chapter 2). These techniques of laser cooling and magneto-optical trapping won the 1997 Nobel prize for Physics and have become the workhorse of ground based cold atom experiments. However, cloud temperatures are limited to $\sim$ 1-100

µK (for Rb-87). Due to the long measurement times possible for spaced based cold atom interferometers, ultra-cold temperatures are required. For example, for a 2 s measurement time, temperatures of $\sim$ 50 nK are required and for a 10 s measurement time temperatures of $\leqslant$ 1 nK are needed [42]. Hence a technique called evaporative cooling can be performed on the pre-cooled atoms. The basic process of evaporative cooling is as follows: atoms are trapped in a potential; the hottest atoms have the largest kinetic energies and therefore rise higher in the potential; the potential is progressively reduced so that the hottest atoms are repeatedly 'evaporated' away; when the remaining atoms re-thermalize, their overall temperature is reduced. This technique is the method of cooling traditionally used to reach the physical phenomenon: a Bose Einstein condensate (BEC) which was awarded the Nobel Prize for Physics in 2001.

To provide the trapping potential for evaporative cooling, magnetic or optical dipole traps are commonly used. Initially, evaporative cooling was achieved in magnetic or hybrid optical-magnetic traps. Magnetic traps are based on the interaction of the atoms with an inhomogeneous magnetic field. However, evaporative cooling in magnetic systems faces issues including: it is relatively slow; trapping geometries are restricted by the available coil or magnet arrangements; and there are perturbations when the magnetic field is turned off [43]. Furthermore, atoms must be prepared in specific (weak field seeking) states and some atoms cannot be magnetically trapped at all.

Significant improvements were made with the invention of hybrid atom chips. Atom chips have all the required magnetic field coils, optical mirrors and electrical components for further trapping and cooling and can reach BECs in evaporation times of $<$ 1 s. The most advanced space focused cold atoms experiments to date have been based on atom chip technology. For example, the German collaboration QUANTUS, formed in 2004, creates

BECs using atom chips and have had several substantial achievements in improving the technology readiness level of cold atoms for space applications [44]. They achieved the first BEC in a microgravity environment in 2007 [45] and then, in 2010, a BEC was realised in the 146m drop tower at the Center of Applied Space Technology and Microgravity (ZARM) in Bremen where strong accelerations up to 50g are experienced [46]. This was followed in 2013 where atom interferometry was successfully performed in the same drop tower [47]. Then in 2017, the Matter-Wave Interferometry in Microgravity (MAUIS) experiment was placed on a sounding rocket. During the six-minute microgravity phase of the flight, a BEC was successfully produced and used to perform atom interferometry [48]. This was the first production of a BEC in space. This group is currently assembling two further payloads, MAIUS-2 and MAIUS-3, which will chronologically attempt to perform single-species atom interferometry and duel-species atom interferometry aboard a sounding rocket respectively for the underlying application of testing the universality of free fall [49].

Furthermore, in 2018 a Cold Atom Laboratory (CAL) was implemented on the International Space Station (ISS) to conduct a series of experiments investigating how cold atoms behave in a space environment. This mission successfully produced the first BEC in Earth orbit [50] and, in 2020, was upgraded to have the functionality to perform atom interferometry in space [51]. Similarly, there are plans for to launch a Bose-Einstein condensate and Cold Atom Laboratory (BECCAL) on the ISS in 2025 which builds on heritage from both CAL and the QUANTUS-MAIUS collaboration and aims to further investigate quantum and atomic physics in this unique environment [52]. Both of these systems use atom chips whilst cooling to BECs.

These fundamental physics experiments have made strong progress in prov-

ing the feasibility of space-based quantum sensors and have built space heritage for future missions. However, as well as the usual problems faced by magnetic traps, there are some inherent challenges with atom chips when considering them for atom-interferometry based Earth observation. Firstly, the atom cloud has to be prepared close to the chip surface for trapping. This limits cloud sizes which can, in turn, reduce the signal-to-noise ratio of a gravimetry measurement. Secondly, the chip must be supplied with a high current for magnetic field generation which could be problematic for an isolated EO satellite which may have a lower power availability than the ISS.

An alternative to atom chips is the optical dipole trap (ODT) which is based on the interaction of the atomic dipole moment induced in a light field with the field itself (as described in detail in section 2.2.2). These trap types have also been used to realise BECs, are much faster than conventional magnetic traps, and can realise a wide variety of trapping geometries (not restricted by the arrangement of coils or magnets). These ODTs can be used for atoms that cannot be magnetically trapped and give access to all the magnetic spin states (not just weak field seeking states). However, they have a significant drawback in the need for high laser powers (on the order of tens of W) to create a sufficient trapping depth to capture a significant number of atoms from the $\sim$ Maxwell-Boltzmann distributed MOT (refer to chapter 2). This has negative ramifications on the SWaP of the system and, in turn, on its possible use in space. The other significant issue with ODTs is that, to perform evaporation, the trap depth is reduced. However, this also reduces the collision rate which slows down re-thermalization and, in turn, evaporation. Whereas for the magnetic traps on atom chips, a RF 'knife' can be used to selectively remove the most energetic atoms from the trap which does not affect the collision rate [53].

The Solution: A Low Power All Optical Ultra-Cold Atom System

Through the use of highly reflective, beam shaping cavity mirrors, optical intensity can be amplified many times. This circumvents the need for a high power laser system which typically would impede the use of an optical dipole trap. Hence, this experiment will use such an optical cavity for power enhancement. Other cavity based optical dipole trapping experiments are described in literature for lithium [54], for Rb-85 [55], and Rb-87 where BECs are created in various cavity modes [56].

Furthermore, the cavity system is designed to perform fast evaporative cooling on a competitive scale with current atom chip systems. This will be done by using both a single beam ODT and optical dipole lattice for trapping. By splitting the power of the initial single beam into the two counter-propagating cavity directions required to form a lattice, a factor of two is gained in trap depth due to interference. This results in a higher (average) trapping frequency for the case of the optical lattice as opposed to the single beam optical trap. Furthermore, in the axial direction of the beam, the lattice trapping frequency is further amplified by a factor of $\sim 10^5$*. This is because trapping frequency is inversely related to the trapping distance which is given by $\sim$ half the wavelength of the laser light used to create the lattice, whereas for the single beam trap it is given by the 'effective Rayleigh distance' which is $\sim 10^5$ times larger [43]. This increase in trapping frequency equates to an increase in atom collision rate for the lattice which results in a decrease in atom re-thermalisation time (which is often the limiting factor in the speed of evaporative cooling in ODTs). However, too high a collision rate can result in too many atoms being removed from the trap and leaves a low final atom number which would detrimentally affect the signal to noise ratio in the subsequent gravity measurement. Therefore, for full

*assuming referring to Rb-87

flexibility, this project will realise a novel design where adjusting the amount of power split between the two cavity directions will allow the balance between the single beam trap and the lattice to be varied. This allows real time control of the trap depth and frequency so that the evaporative cooling process can be optimised for the starting point of the atom interferometry (i.e. gravity) measurements (in terms of atom number, temperature and speed). For example, if speed of test mass generation is the priority, more power could be split into the lattice. Whereas a slower evaporation, with more power split towards the single-beam trap, could produce a higher atom number for measurement. This process of balancing between a single beam ODT and lattice has not been used before to optimise the evaporation process*. In addition, by selecting a specific ODT light wavelength, the system can, for the first time*, perform laser cooling and optical dipole trapping based evaporative cooling to a BEC with a single laser. This significantly reduces the system complexity, SWaP requirements, and cost.

Finally, the atom chip systems presented earlier load their pre-cooled MOT cloud using 3-6 separate input beams. However, the system described in this thesis builds on heritage from the research group by using a single overhead beam, and reflective prisms, to create all the beams required for magneto-optical trapping. This is commonly referred to as the 'prism MOT' (see section 2.2.1). If this experiment is successful then it will be the first time an optical dipole trap will have been loaded, and a BEC generated, from a prism based system. These prism MOTs have the advantage of common noise compared to separate beam systems and crucially are more compact. Compactness is clearly an advantage for any deployable system however specifically for this experiment it may, along with the low power design and custom vacuum components, allow the system

*True according to available literature at time of writing

to undergo initial space testing on a miniaturised satellite named a 'CubeSat'. These satellites are significantly cheaper and easier to launch than full scale versions and they therefore enable much faster verification of and progression in TRL compared to the usual step-wise process described earlier for the QUANTUS-MAIUS experiments. Previous collaborations between the research group and external partners have already successfully miniaturised various components of a cold atoms system and fit them onto CubeSat technology [57]. Note that typically to take a system from concept to a launchable, space-qualified sensor takes significant time, resources, and iterations and hence, this project aims to be a proof-of-principle demonstrator which could secure further funding for future work.

CHAPTER 2

SCIENTIFIC BACKGROUND

The aim of this chapter is to explain the underlying scientific principles, and their significance to this experiment, so that the design decisions and experimental procedures discussed later in the thesis can be fully understood. I begin by describing how atom interferometry is used to measure gravity and the fundamental advantages, and problems, of taking such a device to space. Next, I outline how cold atoms are generated using the powerhouse for the field: the magneto-optical trap. Finally, I detail how the cold atoms are converted to the required ultra-cold atoms using an cavity based optical dipole trap and evaporative cooling.

2.1 Gravimetry: Atom Interferometry

In atom interferometry based gravimeters, a falling ensemble of cold atoms is used as the test mass. During the fall, the quantum wave nature of matter is exploited using light beams to split the atoms into two wave packets, which are sent along different 'paths' or 'arms', before being recombined. In this way the atoms can be made to interfere with themselves. The situation is analogous to a light interferometer but, in this case, we have atomic 'beam splitters' and

'mirrors' generated with the laser beams. A detailed analysis of this process, theoretically and experimentally, is given in many sources [58, 59]. Here, I present an overview of the key principles relevant to understand the motivation of the experiment.

2.1.1 Rabi Oscillations

By using the time dependent Schrödinger equation, it can be shown that applying a resonant light field to a two-level atom results in sinusoidal population oscillations between the two energy states. This is known as Rabi-oscillations as the populations fluctuate with the so-called Rabi frequency, Ω_{eg} where [60]:

$$\Omega_{eg} = -\frac{\langle e| \mathbf{d} \cdot \mathbf{E_0} |g\rangle}{\hbar} \tag{2.1}$$

where the $|e\rangle$ and $|g\rangle$ represent the excited and ground states of the two-level atom respectively, E_0 is the electric field amplitude of the light, and $\mathbf{d}$ is the electric dipole moment operator for the transition. These oscillations form the building blocks of an atom interferometer because specific population transfers can be created by selecting a specific pulse duration of the light. For example, assuming the atoms all start in the same initial state, a pulse of length $t\ \Omega_{eg} = \pi/2$ will create a superposition of both states with equal probabilities i.e. it splits the atoms into the two states equally. Whereas a pulse of length $t\ \Omega_{eg} = \pi$ will invert the population of the two states, or in other words, it will transfer all the atoms from one state to the other. Taking into account the momentum gained during population transfer, these 'π' and '$\pi/2$' pulses respectively act as the atomic 'mirror' and 'beam splitter' required for an atom interferometer. For a detuned (off-resonant) beam, the Rabi frequency and population equations are modified so that total population inversion can no

longer be achieved. The effect of this is illustrated schematically in figure 2.1. The oscillation rate is then given by the off resonant Rabi frequency, Ω_r where

$$\Omega_r = \sqrt{\Omega_{eg}^2 + \delta^2}. \tag{2.2}$$

where δ is the detuning.

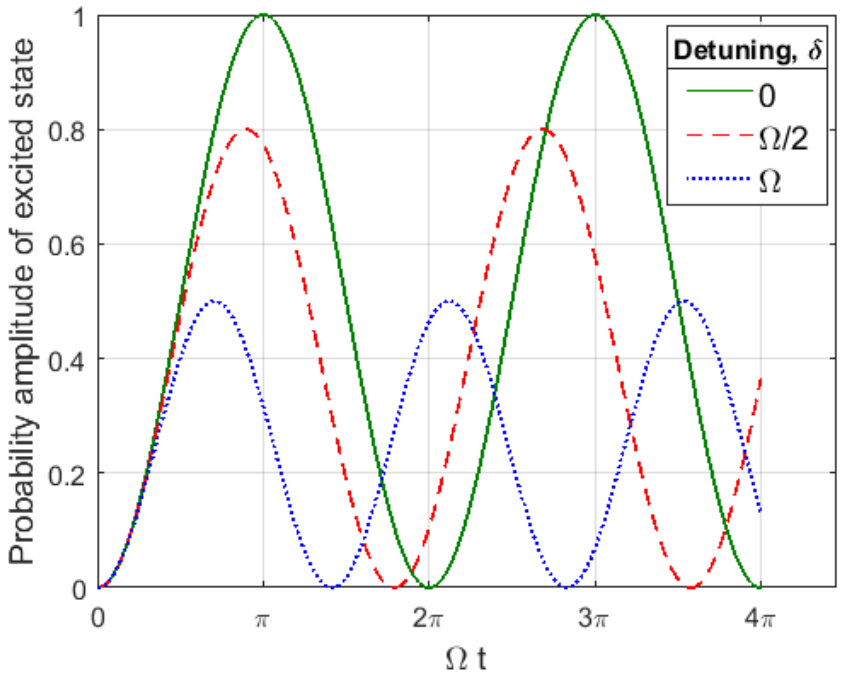

Figure 2.1: Rabi oscillations in the excited state population of a two-level atom for different detuning values, δ, given as a function of the on-resonance Rabi frequency, Ω. The probability amplitude represents the likelihood of finding an atom in the excited state. The light is applied continuously from time $t = 0$ and initially all atoms are in the ground state.

2.1.2 The Atom Interferometry Sequence

The key steps of a standard Mach-Zehnder [59] atom interferometer are as follows:

1. The atoms undergo **state selection** to ensure they all start in the same initial state.

2. Any trapping potentials are switched off to allow the **atoms to fall due to gravity**.
3. **$\pi/2$ pulse**: an initial light pulse of duration τ creates a superposition of atoms in the two population states. The atoms that experience a transition are spatially re-directed with respect to the unperturbed atoms due to photon recoil. Hence, a **superposition of both internal energy and external momentum states is obtained**.
4. **π pulse**: after allowing the atoms to evolve freely for time T, a second pulse is applied of length $\sim 2\tau$. This **inverts the internal and external states of the two wavepackets** so that after another time T, the atoms will all spatially overlap again.
5. **$\pi/2$ pulse**: a final pulse is applied, identical to the first, to **interfere the two states with each other** when they are overlapping.
6. Finally, the **output of the atom interferometer is measured** using resonant beams of light.

This sequence is visualised in figure 2.2 which shows the three-point parabola paths taken by the two atomic wavepackets. The atoms are assumed to begin in the ground state $|g\rangle$ with some initial momentum $\mathbf{p}$. The following sections will explain this figure in further detail.

2.1.3 Gravimetry & Sensitivity

During the measurement stage, the total phase accumulated during atom separation, entitled the interferometer phase Φ, can be read-out to provide a gravity measurement. This phase can be directly measured by evaluating the final populations in each energy state. If the phase is zero, or an integer multiple of 2π, then the atoms will all be in the initial state i.e. in the classical sense, the two 'arms' of the interferometer are the same length. If the atom inteferometry

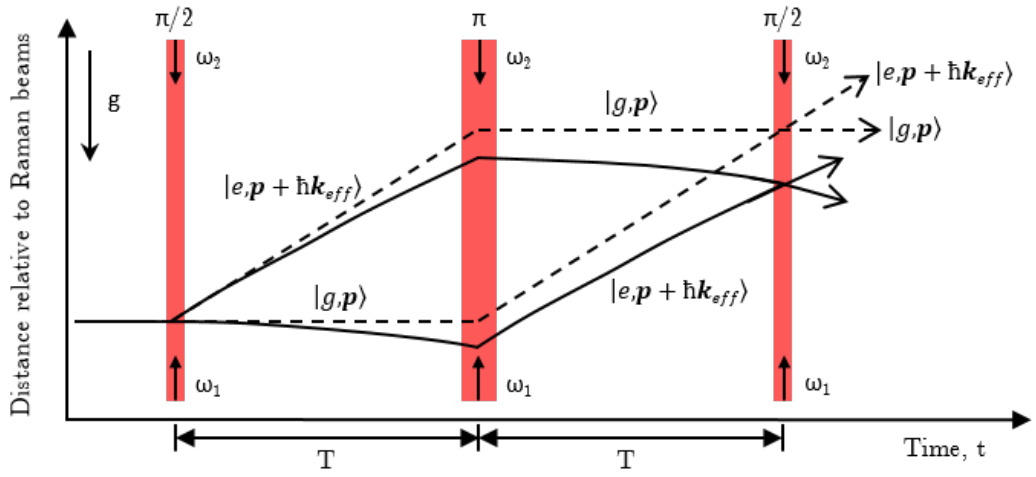

Figure 2.2: Visualisation of the atom interferometry sequence where atoms are split, inverted and recombined using a sequence of two beam light pulses with frequencies ω_1 and ω_2. The dashed and solid loops respectively represent the paths travelled by the atoms when there is no force of gravity and when they are in a uniform gravitational potential, $\mathbf{g}$. Refer to the text for more information. Adapted from [61].

region has a uniform gravitational potential, then the free evolution of the atoms creates no phase difference. Therefore, the only phase difference gained is due to the interaction with the three light pulses, which depends on the local gravitational acceleration, $\boldsymbol{g}$ [59]. By appropriate summation of each phase shift it can be shown that the total interferometry phase accumulated is

$$\boldsymbol{\Phi} = \boldsymbol{k_{eff}} \boldsymbol{g} T(T + 2\tau) \tag{2.3}$$

where $\boldsymbol{k_{eff}}$ is the effective wavevector of the transition. This laser phase shift imprinting is analogous to a classical gravity measurement where the position of a mass in free fall is measured three times. Since T and $\boldsymbol{k_{eff}}$ are fixed experimental parameters, a value for the local gravity can be obtained. To estimate the sensitivity of the gravity measurement, Δg, we temporarily neglect

the finite length of the Raman pulses so that equation 2.3 is simplified to $\boldsymbol{\Phi = k_{eff} g} T^2$. Assuming the interferometer noise is limited only by atom shot noise [62, 63], then the signal to noise ratio is given by SNR $\sim \sqrt{N}$ where N is the atom number participating in the measurement. This equates to a gravity measurement shot noise sensitivity of

$$\Delta g = g\frac{\Delta\Phi}{\Phi} \sim \frac{1}{\sqrt{N}|k_{eff}|T^2}. \tag{2.4}$$

The following sub-sections will focus on the different terms of this equation and how they shape the experiment.

Two-photon Transitions

The sensitivity of the gravity measurement depends linearly on the spatial separation achieved between the two wave-packets, or equivalently, on the area of the 'interferometer loop' (see figure 2.2). In equation 2.4, this is encapsulated in the $|k_{eff}|$ term, which we want to be as large as possible. To increase the momentum transfer in the splitting stage, two counter-propagating laser beams create a two-level stimulated Raman* process. To best understand this, observe the ground state $|g\rangle$ and excited state $|e\rangle$ in figure 2.3. Instead of applying a resonant beam with frequency ω_{eg}, two laser beams are applied with frequencies ω_1 and ω_2 to transfer the atom from one state to the other, via a virtual, intermediate state $|i\rangle$. The atom absorbs a photon from one beam and, via stimulated emission, emits a photon into the other. Population of the intermediate state is avoided by detuning both laser beams by Δ from resonance. By making the beams counter-propagating, the momentum gained by the atom will be in the same direction for both absorption and emission. This increases the momentum transfer by orders of magnitude compared to the

*The term Raman refers to an inelastic process

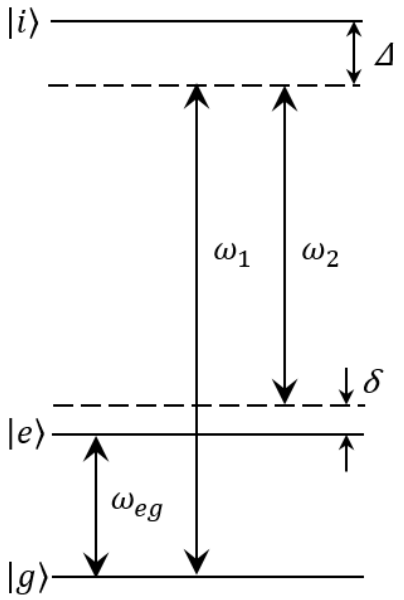

Figure 2.3: A two-photon transition uses lasers of frequencies ω_1 and ω_2 to drive transitions between energy levels $|g\rangle$ and $|e\rangle$ through an intermediate state $|i\rangle$. Sufficient detuning Δ on both beams means the intermediate state is virtual and unpopulated. Modified from [59].

direct excitation (or the co-propagating beam case). In this case the effective wavevector is defined by $\boldsymbol{k_{eff} = k_1 - k_2}$ where the subscripts refer to the laser beams.

For ^{87}Rb, the states used for atom inteferometry are typically the lower and upper hyperfine ground states: $\big(|g\rangle = 5^2S_{1/2}, F = 1 \rightarrow |e\rangle = 5^2S_{1/2}, F = 2\big)$. In this case, the direct transition is prohibited due to selection rules but, by using counter-propagating beams, the momentum transfer is increased by $\sim 10^5$ compared to the co-propagating case. These ground states have the advantage of sufficiently long lifetimes (compared to excited states) so that natural decay does not affect the populations and, hence, gravity measurement.

It should be noted that the derivation for the populations in each energy state can be extended from a two-level to three-level system and similar sinusoidal fluctuations are obtained but the populations now oscillate with the generalised Rabi frequency. This is a quadrature combination of the two-photon Rabi

frequency and two-photon detuning, δ which is the overall detuning of the transition when both laser frequencies are taken into account [59]. This detuning is required because, as the atoms free fall, they will experience a time-dependent Doppler shift of the light which would take them out of resonance. Therefore, the detuning is used to cancel out the phase shift imprinted by gravity. The rate at which the detuning must be swept, called the chirp rate α, is linked to the local gravitational acceleration by:

$$2\pi\alpha = \boldsymbol{k_{eff}} \cdot \boldsymbol{g}. \tag{2.5}$$

It is by measuring this chirp rate that the local gravitational acceleration is calculated.

Interferometry Time & Atom Temperature

From equation 2.4, it is observed that the sensitivity of the gravity measurement scales with the time between the interferometry pulses, or the T-time, squared. On ground systems are limited to $\sim$ 200 ms by the height of the system and the relatively large gravitational acceleration of the Earth [59]. However, in the low gravity environment of space, this value can be increased to $\sim$ 1-10 s which, in turn, increases the atom inteferometry sensitivity by up to a factor of 10,000. This highlights one potential advantage of taking such devices to space, especially for high sensitivity applications such as testing Einstein's equivalence principle [22] or gravitational waves [64].

However, the longer the experimental duration, the higher the likelihood that the thermal expansion of the atom cloud will limit the contrast of the interferometer. This is because the atoms towards the edge of the cloud will experience a lower beam intensity, caused by the Gaussian shaped laser beams. Due to the intensity dependence of the Rabi frequency (see equation 2.1), this

causes non-perfect splitting and inversion of the populations during the π and $\pi/2$ pulses. At the interferometer output, this results in a significant fraction of the atoms being in the 'wrong' energy state which has detrimental effects on the measurement. Two ways to counter this problem are to create a more uniform beam profile or to lower the temperature, and hence expansion, of the atoms. Work with large beam sizes or flat top beam profiles is in development for ground-based systems [65]. However, these methods are: power inefficient; in the latter case underdeveloped; and over the long T-times of space, they become impractical due to the requirement of large optics and vacuum systems to accommodate such beams. Hence, the favoured option is to produce lower temperature atoms. As detailed by Carraz et al., a T-time of 5 s requires a maximum temperature of 10 nK which equates to a cloud expansion of 1mm/s (in fact temperatures < 1 nK are likely be required for this T-time) [42]. As will be shown in the following section, the usual laser cooling method is not sufficient to reach these temperatures and hence further cooling stages must be used. This is the motivation for the two-stage cooling process employed in this experiment.

Atom Number

The final term in equation 2.4 is the atom number taking part in the measurement which we want to be as high as possible to maximise gravity sensitivity. As will be described later in the chapter, the two-stage cooling process is lossy in terms of the atom number retained in the cloud. Hence it's essential to maximise cold atom transfer between each stage of trapping. Details on this process will be given in section 2.2.2.

2.2 Ultra-Cold Atom Sample Preparation

2.2.1 The Magneto-Optical Trap

The three-dimensional magneto-optical trap is the starting point for the majority of cold and ultra-cold atom experiments, including atom interferometry based gravimeters. Since initial demonstration in 1987 [66], they have been used in both fundamental physics and in practical applications [67] [68]. These '3D MOTs' produce confined clouds of neutral atoms at temperatures on the order of tens of mK [66]. In this section, the 3D MOT is discussed, with specific focus given to the cooling limitations of this process.

Laser Cooling & Optical Molasses

The magneto-optical trap relies on the principle of laser cooling which was theorised in 1975 [69], inspired by the invention of narrow linewidth tunable lasers [70]. Theory became reality in 1978 with the laser cooling of ions [71, 72], followed by neutral atoms in 1981 [73]. This cooling process is based on the scattering force that a laser light field exerts on an atom.

The Scattering Force

When an atom absorbs a photon from a laser, it gains momentum $\hbar\mathbf{k}$ in the direction of the beam, where $\mathbf{k}$ is the wavevector of light [53]. This excited atom will then de-excite via either stimulated or spontaneous emission. A fundamental result of quantum mechanics is that photons produced by stimulated emission are emitted in the same direction as the initial stimulating photons [74, 75]. Therefore, in the former process of excitation and stimulated emission, there is no net momentum imparted on the atom. Whereas, during spontaneous emission, each photon is released in a random direction: uncorrelated to the

initial absorption. Hence, over many absorption-emission cycles, the recoil momentum accumulated by the atom due to spontaneous emission has no preferred direction and it averages to zero. This means the only net force acting on the atom is due to the initial photon absorption i.e. in the direction of the laser beam. This is the scattering force.

It is clear that this force, $\mathbf{F}$, will be equal to the rate at which these spontaneous scattering processes occur, γ, times the momentum absorbed by a single photon: $\mathbf{F} = \hbar\mathbf{k}\gamma$. Assuming a two level atom initially at rest, this equation becomes [53]:

$$\mathbf{F} = \frac{h\Gamma}{2\lambda_0} \frac{s}{1 + s + 4((\omega_0 - \omega)/\Gamma)^2} \hat{u} \tag{2.6}$$

where λ_0 and Γ are the resonant wavelength and natural linewidth of the transition respectively, ω_0 is the resonant angular frequency of the transition, ω is the laser angular frequency, $\hat{u}$ is a unitary vector along the direction of propagation of the beam, and for simplicity the saturation parameter is defined as $s = I/I_s$ where I_s is the saturation intensity of the transition [53].

Doppler Cooling

To explain how this force can result in cooling, imagine two counter propagating, equal intensity laser beams that are red-detuned by $\Delta = \omega - \omega_0$ with respect to the atomic transition frequency*. If an atom is at rest, it observes no difference in the laser's frequencies and hence there is no preferential absorption from either beam. However, if the atom is travelling towards one beam with velocity v, the frequency of that beam will be Doppler shifted towards resonance in the rest frame of the atom (and vice versa for the beam it is moving away from). Hence, the atom will preferentially absorb from the beam it is moving

*Not to be confused with the detuning parameter used in atom interferometry

towards, obtaining an overall momentum kick that opposes its direction of motion. Therefore, the atom is gradually slowed down. This is dubbed Doppler cooling due to the crucial role of the Doppler shift effect and is demonstrated in figure 2.4.

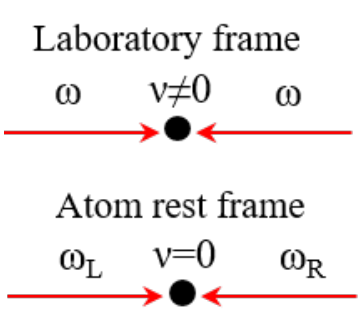

(a) In the rest frame of a moving atom, the left and right laser beam frequencies are shifted to ω_L and ω_R respectively.

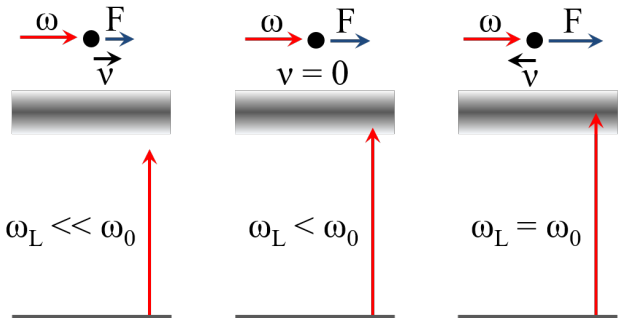

(b) Demonstrates how the Doppler shift affects the force, F, exerted by a laser beam on an atom moving at velocity ν. The resonant frequency of the atom is ω_0 and the laser frequency is ω.

Figure 2.4: Illustrates how two counter-propagating, red-detuned laser beams can be used to cool moving atoms.

Mathematically, this cooling process is demonstrated by examining the total force acting on the atom. Using equation 2.6, this force is given by:

$$\mathbf{F} = \frac{h\Gamma}{2\lambda_0}\left[\frac{s}{1+s+\alpha^2(\Delta c/\omega - v)^2} - \frac{s}{1+s+\alpha^2(\Delta c/\omega + v)^2}\right]\hat{u} \tag{2.7}$$

where, for ease, we define the parameter $\alpha = (2\omega/\Gamma c)^2$ *. By Taylor expansion of equation 2.7, it can be shown that this force acts as a viscous damping force with a linear dependence on velocity when the Doppler shift is small compared to the detuning i.e. $F \approx -\beta v$ where β is a positive constant [76]. This restoring force is represented by the red dashed line in figure 2.5 where the slope is given by $-\beta$.

*Not to be confused with the chirp rate in atom interferometry

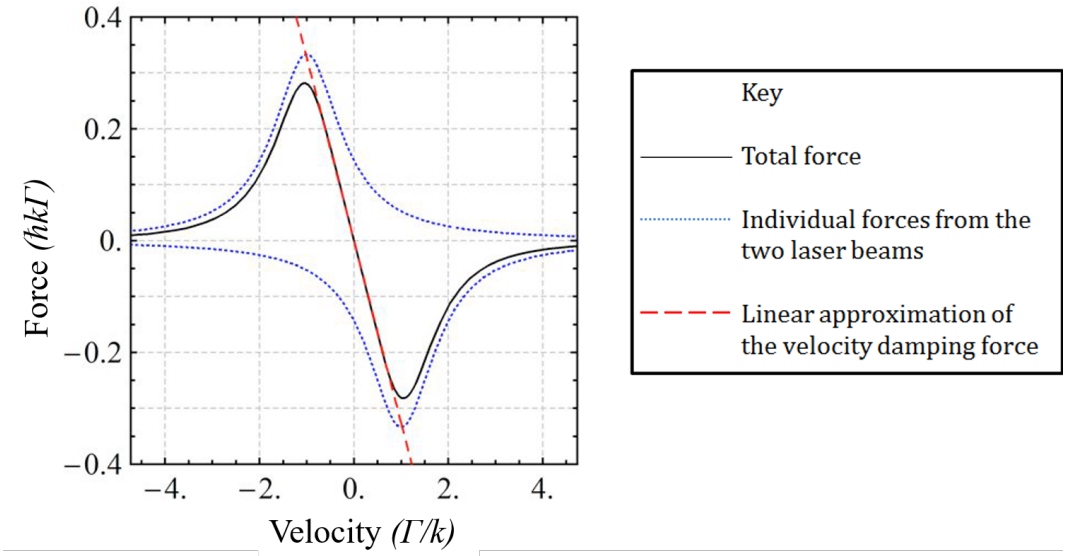

Figure 2.5: The time averaged force experienced by a two-level atom in one-dimensional optical molasses where the detuning is assumed to be $\Delta = -\Gamma/2$. [76].

Three-Dimensional Optical Molasses

By using three pairs of these red-detuned, counter propagating lasers, cooling can be achieved in all three dimensions in the overlap region of the beams. This is known as three-dimensional optical molasses.

The Doppler Limit

There is a theoretical limit to the minimum temperature achievable with this Doppler cooling process. This occurs when the damping force, removing kinetic energy, balances the heating due to the stochastic nature of the absorption and emission process. These absorption-emission cycles are seen by the atom as a random walk, and by modelling this walk the cloud temperature can be defined as [76]:

$$T = \frac{\hbar\Gamma}{4k_B}\frac{1 + I/I_{sat} + (2\Delta/\Gamma)^2}{2|\Delta|/\Gamma}. \tag{2.8}$$

The theoretical minimum temperature is therefore reached when $\Delta = -\Gamma/2$. For

the D2 transition of rubidium atoms this equilibrium, or Doppler temperature, is equal to $T_D \approx 146$ µK.

Sub-Doppler Cooling

To the surprise of the scientific community, temperatures below the Doppler limit were experimentally observed in 1988 [77]. To understand this 'sub-Doppler' cooling process, the picture presented previously must be extended to include the interference of the counter-propagating beams and the multi-level (hyperfine) structure of atoms. In a spatially variant light field, optical pumping between sub-levels will occur and this provides a new mechanism for cooling. The qualitative description that follows is based on "Laser cooling below the Doppler limit by polarisation gradients" by Dalibard and Cohen-Tannoudji (1989) [78].

As described subsequently, optical molasses, used to form magneto-optical traps, typically use σ^+ and σ^- polarisations for the counter-propagating beams. Interference of the beams gives a standing wave in the total polarisation. As can be seen in figure 2.6, the resulting electric field has a constant magnitude (same intensity for all z) and is linearly polarised everywhere. Therefore, only π transitions are allowed between different magnetic sub-levels (i.e. $\Delta\, m_F = 0$). Hence, an atom in the ground state with a particular m_F can only be excited to the same corresponding $\mathrm{m}_{F'}$ level. However, once excited, the atom can decay via spontaneous emission back to any allowed ground state. For an atom at rest, this results in the population being higher for the $\mathrm{m}_F = 0$ states than in the $\mathrm{m}_F = \pm$ 1, 2, etc. states because of the inequality of the Clebsh–Gordan coefficients, as can be seen in figure 2.7. This is referred to as atoms being 'optically pumped' towards the $\mathrm{m}_F = 0$ state.

However, although the light is linearly polarised everywhere, the polarisation

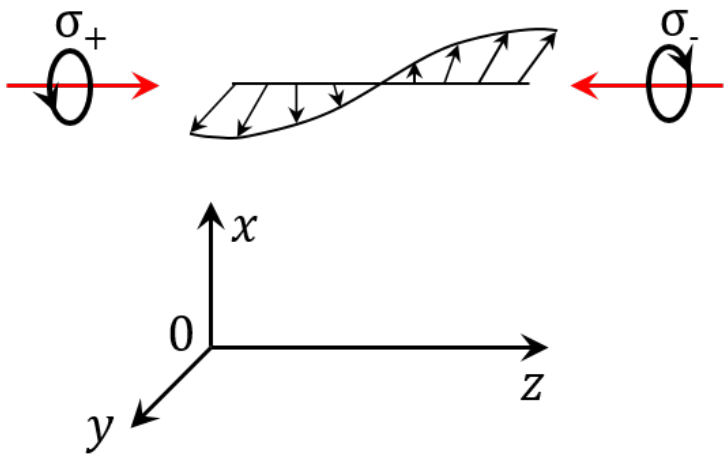

Figure 2.6: Two counter-propagating σ^+-σ^- beams results in a total field with linear polarisation that rotates in space. Adapted from [78].

direction rotates through 2π over one wavelength. Therefore, moving atoms experience a rotating linear polarisation. When the Hamiltonian of the moving atom is formulated in the rotating frame, it is found that it contains an inertial term that allows coupling between the various ground state sub-levels and results in asymmetric population distributions between the $m_F = \pm 1$ levels. It is found that, when the detuning is negative or red (as it is for our optical molasses), an atom moving towards the $z > 0$ will populate the m_F = -1 sub-level more than the $m_F = +1$ sub-level. Also, in this regime, an atom in m_F = -1 moving with $z > 0$ has a 6 times higher probability of absorbing a σ^- photon than a σ^+ photon. Hence, the atom scatters more σ^- photons (travelling in the opposite direction to its motion) than σ^+ photons (travelling in the same direction as its motion), which causes an imbalance in radiation pressures and reduces its velocity. It should be emphasised that this damping and imbalance in photon absorption is not due to the Doppler shift that induces Doppler laser cooling but due to the difference in ground state populations induced by the rotating polarisation gradient. This requirement of polarisation gradients results in this process being referred to as 'σ^+- σ^- polarisation gradient cooling'.

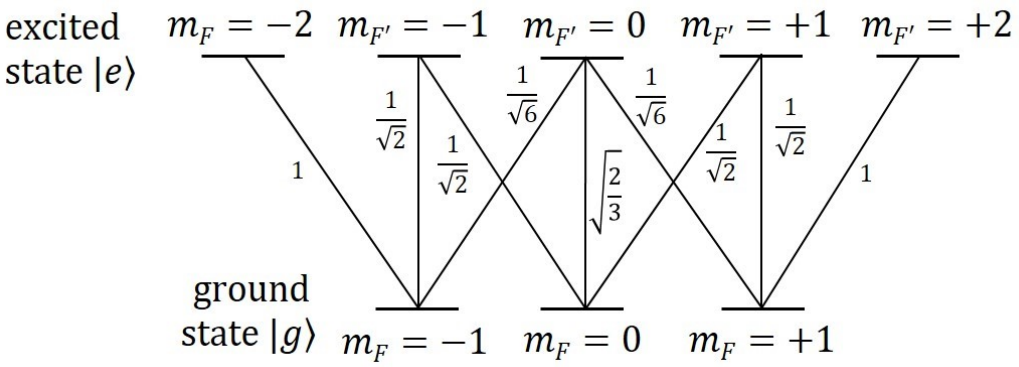

Figure 2.7: Clebsh–Gordan Coefficients for a $J_g = 1 \leftrightarrow J_e = 2$ Transition.

Note, in the regime of interest, both the Doppler and sub-Doppler cooling processes depend linearly on the velocity but the former is proportional to the light intensity whilst the latter is independent of it. Hence, at low laser powers, the sub-Doppler cooling parameter is much larger than the Doppler cooling parameter, and therefore, this sub-Doppler process works at lower velocities and allows lower temperatures to be reached. Whereas, at higher velocities, the total cooling force approximates to the Doppler force and the sub-Doppler contribution is negligible. The sub-Doppler force is calculated to be at a theoretical maximum when $\Delta = \sqrt{5/4}\Gamma$.

The Recoil Limit

The limit to the sub-Doppler cooling processes is determined by the momentum of a single photon i.e. the minimum kinetic energy an atom can have corresponds to one photon recoil = $\hbar k$. Typically the recoil limit is $\sim$ 0.1 µK [53] which is 100 times larger than the low temperatures required (see 2.1.3). Furthermore, to reach this limit experimentally is practically difficult due to heating mechanisms. Therefore, to fully utilise a space-based cold atom interferometer, further cooling mechanisms must be employed. This will be discussed in 2.2.3.

Atomic Species & Repumping

The energy transferred by an individual photon in the cooling process is small compared to the initial kinetic energy of the atom. Therefore, many absorption-emission cycles are required to obtain the low-temperature atoms required. Hence, alkali metals are often chosen because they display (nearly) closed two-level transitions so the atom can remain in the cooling process over many cycles. One such transition is the D2 line $\left(5^2\mathrm{S}_{1/2} \rightarrow 5^2\mathrm{P}_{3/2}\right)$ of rubidium-87 whose energy level structure is given in figure 2.8. From this diagram, and by noting the selection rule for the hyperfine splitting quantum number $\Delta F = 0, \pm 1$ [53], we observe that an atom excited from the upper ground state to the upper excited state ($F = 2 \rightarrow F' = 3$) can only de-excite back down to the initial level. This cooling transition is illustrated by the red arrows in the figure. However, due to the finite width of the excited states, excitations to the $F' = 2$ level are also allowed. From there, the atom can de-excite either to the initial level or to the lower energy ground state ($F = 1$) from which it will be unable to re-excite (black arrows). Therefore, the atom can be trapped in this 'dark state' and removed from the cooling cycle. Hence, we add a proportional amount of re-pumping light (blue arrow) to continuously remove atoms out of this state. A further advantage is that the hyperfine excited state has a sufficiently long natural lifetime so it is unlikely to decay over a single atom interferometry cycle.

Historically, rubidium was chosen over other alkali metals as its transition frequency was accessible by pre-existing, readily available lasers and optical components [80]. Furthermore, the temperature required to achieve sufficient vapour pressure with a heat activated dispenser is relatively low and can be achieved with a current of 5.3 A to a SAES rubidium metal dispenser [81]).

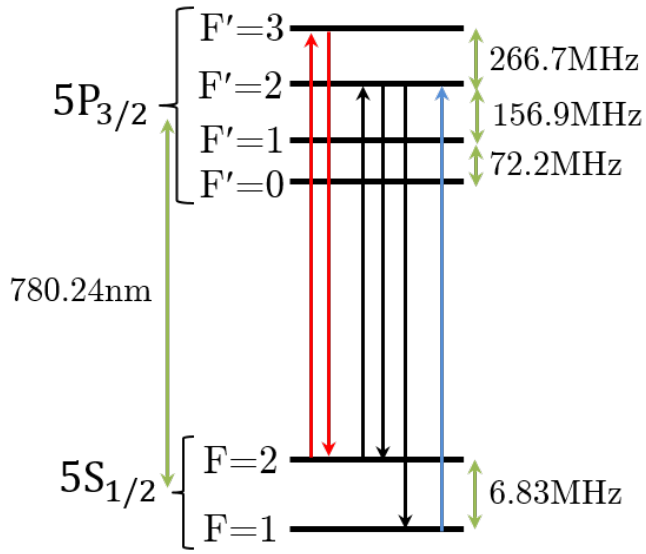

Figure 2.8: Energy level scheme of the D2 line of rubidium-87. Values are reproduced from literature [79]. The red arrows illustrate the cooling cycle. The black arrows are the undesired transitions that may result in the atom becoming trapped in the 'dark', F=1 state. The blue arrow shows the re-pumping light.

The rubidium-87 isotope is typically selected over rubidium-85, even though the latter is in larger abundance, because it has advantages for the production of Bose-Einstein condensates (see section 2.2.4). The key advantage is it's large positive scattering length which causes mutual repulsion at low temperatures. This prevents the collapse of all but the smallest condensates and facilitates forced evaporative cooling. Rubidium-85, however, has a negative scattering length which hinders both condensate stability and evaporate cooling [82].

The Three-Dimensional Magneto-Optical Trap

The previously described scattering force is velocity, but not spatially, dependent. To create a test mass for atom interferometry, both cooled and trapped atoms are required. A spatial dependence is added to the force using a magnetic field. For understanding this concept, initially assume a transition from a $J = 0$ ground state to a $J' = 1$ excited state.

Consider the linearly inhomogeneous magnetic field produced by a spherical quadrupole. In one-dimension, the form of the field is $\mathbf{B} = bz$ where b is a constant. Due to the Zeeman shift, this magnetic field perturbs the energies of the magnetic sub-levels according to:

$$\Delta E = g\mu_B m_j B = g\mu_B m_j bz \tag{2.9}$$

where g is the Landé g factor of the state, μ_B is the Bohr magneton, and m_j is a quantum number representing the projection of the total angular momentum of the atom along a specified axis. For the ground state, $m_j = 0$ only and hence there is no perturbation. However, the excited state has allowed values of $m_j = 0, \pm 1$ and hence the energy degeneracy is removed. This is demonstrated schematically in figure 2.9.

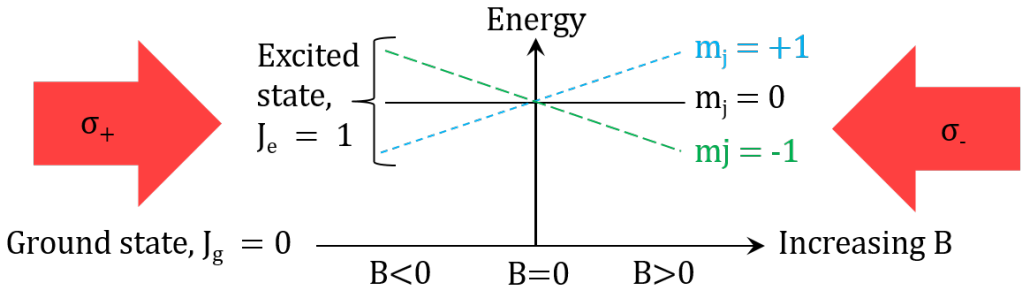

Figure 2.9: A magnetic field B, that is increasing linearly in the positive z direction, creates energy perturbations in the magnetic sub-levels of the excited state of a two level atom. Red-detuned, counter-propagating laser beams are then used to cool and push the atoms towards $z = 0$ ($\equiv B = 0$).

Now consider the counter-propagating optical molasses beams to be circularly polarised so that the beams propagating in the positive and negative z directions have σ^+ and σ^- polarisations respectively. Due to the red-detuning and magnetic field gradient, an atom on the positive z side will view photons from the σ^- beam (moving towards it) to be closer to resonance than those from the σ^+ beam. Therefore, the atom will scatter more σ^- photons and

be pushed towards the centre of the field (at $z = 0$). This effect is stronger, the further from $z = 0$ the atom is. Vice versa is true for an atom with a negative z coordinate which results in the cooling force given earlier obtaining a directional component:

$$F \approx -\beta v - kz \tag{2.10}$$

where the 'spring constant' k is:

$$k = \frac{\beta g \mu_B b}{\hbar k_B}. \tag{2.11}$$

By using three pairs of red-detuned, counter-propagating, circularly polarised beams, the 3D magneto-optical trap is obtained.

It is well established in literature how MOT parameters (atom number, temperature, density, loading time, and lifetime) depend on: background vacuum conditions; the strength of the magnetic field gradient; and laser beam size, power and detuning [83–87]. Experimentally these factors will be used to optimise the MOT/molasses for optical dipole trap loading.

Capture Velocity

There is a maximum atom velocity that can be captured in the 3D MOT due to the finite region over which the atoms are cooled, set by the size of the cooling beams. This capture velocity can be approximated as [88]:

$$v_c \sim \sqrt{\frac{2DF_{\max}}{m}} \tag{2.12}$$

where D is the diameter of the cooling beams, $F_{\max}$ is the maximum radiation pressure force, and the magnitude of the scattering force, and m is the mass of the rubidium atom.

The Prism Magneto-Optical Trap

For practical gravimeters, including space-based ones, minimising the size of the system is an important priority. Therefore, the 6 separate counter-propagating beams required to generate a 3D MOT can be replaced with a single overhead beam reflected by four prisms and a mirror. Figure 2.10 shows how this 'prism MOT' system generates the required beams with the correct polarisations. Note that an additional waveplate is needed for the mirror reflected beam for polarisation correction.

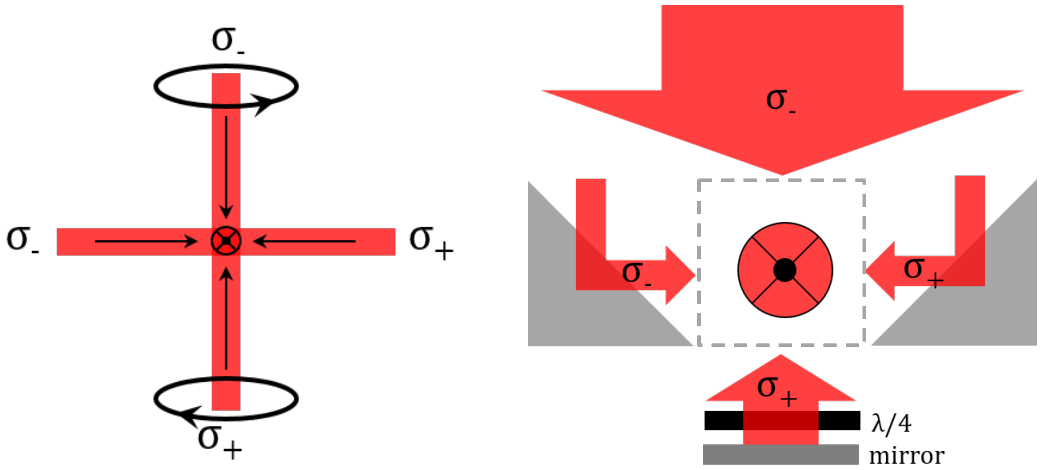

(a) 6 Beam MOT **(b)** Prism MOT

Figure 2.10: Illustrates how a 3D MOT can be generated with either (a) 6 separate input beams (3 counter-propagating pairs) or (b) one larger overhead beam, reflective prisms, a half-waveplate, and a mirror. The final 2 beams and prisms are in and out of the page.

This design reduces the size of the 3D MOT generator and has an additional advantage of common noise between the 3D MOT beams. These single beam reflective MOT generation techniques were first developed and utilised in the 1990s by various groups [89–91]. However, the more recent availability of highly reflective, flat surface quality, off-the-shelf prisms has enabled this technique to be realised more easily. Prism MOT systems have become well-established

within the group at the University of Birmingham [92].

Atom Loading: The Two-Dimensional Magneto-Optical Trap

To obtain a 3D MOT, atoms must be 'loaded' into a vacuum chamber for cooling and capture. For rubidium-87, the simplest method is to use a dispenser where atoms are evaporated from a metallic strip by applying a heating current. However, there is a maximum atom velocity which can be captured in the 3D MOT (as outlined in 2.12) and alkali metals evaporate at temperatures of several hundred °C. Therefore, only a small fraction of the dispensed atoms will be captured which is detrimental to the atom interferometry measurement statistics. To improve the captured number, the background atom pressure can be increased (by increasing the current) but this also increases the collisional losses and hence reduces the MOT lifetime. Furthermore, in this experiment, mirrors are also required inside the vacuum (see 3.2) and a high background pressure would coat these mirrors and reduce their reflectivity.

An alternative loading method is to generate a pre-cooled beam of atoms in a separate chamber (using a dispenser) and then direct them into the 3D MOT region through a narrow tube that limits the background conductance. One advantageous option is the two-dimensional magneto-optical trap (2D MOT). This is similar to the 3D version except it uses a 2D quadrupole magnetic field (instead of a spherical quadrupole). This 2D field has a line of zero magnetic field (rather than a point) to which the atoms are confined. This generates two counter-propagating beams of atoms. One of which can be used to load the 3D MOT chamber. Furthermore, to enhance the flux of the atomic beam, some of the atoms in the beam moving away from the 3D MOT chamber can be redirected with an additional 'pushing' beam. In addition to the ability to maintain a low background pressure in the 3D MOT chamber, using a 2D

MOT for loading has further advantages including loading a high atom number in a shorter time with an increased 3D MOT lifetime [93].

2.2.2 The Optical Dipole Trap

As previously explained, the laser cooling present in a 3D MOT does not create sufficiently low temperature atoms for the application of this experiment. Therefore, further cooling is required. In a 3D MOT the trapping and cooling mechanisms are combined and hence an alternative trapping method is required to accommodate further cooling.

One method of trapping neutral atoms is the optical dipole trap (ODT), first demonstrated in 1986 [94]. As has been previously described in chapter 1, these traps have been chosen for this experiment due to certain key advantages over other trapping mechanisms. Optical dipole traps rely on the optical dipole force created by the electric dipole interaction with far-detuned light [43]. This large detuning from resonance is chosen to achieve a low spontaneous scattering rate. Note that these traps are a type of Far-Off Resonance Trap (FORT) and are sometimes referred to as such.

To derive the key equations for this optical dipole interaction, we model atoms as simple oscillators. This follows the description outlined in 'Optical dipole traps for neutral atoms' by R. Grimm (2000) [43] and 'An optical dipole trap for transport of Rubidium-87 atoms' by S. Meyer Viol (2014), as does the rest of the ODT section.

Oscillator Model

To create an ODT, a cloud of pre-cooled atoms is subject to a laser beam with an intensity gradient. The electric field of the laser is given by:

$$\mathbf{E}(\mathbf{r},t) = \hat{\mathbf{e}}\, E(\mathbf{r}) \exp(-i\omega t) \tag{2.13}$$

where $\hat{\mathbf{e}}$ is the unit polarisation vector, and E and ω are the amplitude and frequency of the electric field respectively. This field results in the positive and negative charges in the atom experiencing opposing forces. This causes the charges to separate which induces an atomic dipole moment, $\mathbf{p}$, that oscillates at the driving frequency ω according to:

$$\mathbf{p}(\mathbf{r},t) = \hat{\mathbf{e}}\, p(\mathbf{r}) \exp(-i\omega t) \tag{2.14}$$

where p is the amplitude of the dipole moment. The dipole moment is related to the electric field by $\mathbf{p} = \alpha\mathbf{E}$ where α defines the complex polarisability which depends on the driving frequency ω, i.e. $\alpha(\omega)$.

The interaction potential of the dipole moment in the field is given by:

$$U_{\text{dip}} = -\frac{1}{2}\langle \mathbf{pE} \rangle = -\frac{1}{2\epsilon_0 c}\,\text{Re}(\alpha) I(\mathbf{r}) \tag{2.15}$$

$$\text{where the field intensity,} \quad I(r) = \frac{\epsilon_0 c}{2}|E|^2, \tag{2.16}$$

where $\langle . \rangle$ denotes the time average over many oscillations, and ϵ_0 is the vacuum permittivity. The real part of the polarisability is the component of the dipole oscillation that is in phase with the driving field and is responsible for the dispersive properties of the interaction. The dipole force can then be written

as the gradient of the interaction potential:

$$\mathbf{F}_{\mathrm{dip}}(\mathbf{r}) = -\nabla U_{\mathrm{dip}}(\mathbf{r}) = \frac{1}{2\epsilon_0 c}\,\mathrm{Re}(\alpha)\nabla I(\mathbf{r}). \tag{2.17}$$

This is an approximately conservative force proportional to the intensity gradient of the driving field i.e. the force is higher at the focus of the laser where the intensity is highest (assuming the polarisability is positive).

The other key parameter in an optical dipole trap is the scattering rate which is proportional to the power absorbed by the oscillator from the driving field (and re-emitted as dipole radiation), P_{abs}, given by the change in dipole potential over time:

$$P_{\mathrm{abs}} = \left|\dot{U}_{\mathrm{dip}}\right| = \langle \dot{\mathbf{p}}\mathbf{E} \rangle = 2\,\omega\,\mathrm{Im}(pE^*) = \frac{\omega}{\epsilon_0 c}\,\mathrm{Im}(\alpha) I(\mathbf{r}). \tag{2.18}$$

The imaginary part of the polarisability describes the component of the dipole oscillation that is out of phase with the driving field and hence causes absorption. This power is then divided by the energy of a single photon, $\hbar\omega$, to obtain the scattering rate, Γ_{sc}:

$$\Gamma_{\mathrm{sc}}(\mathbf{r}) = \frac{P_{\mathrm{abs}}}{\hbar\omega} = \frac{1}{\hbar\epsilon_0 c}\,\mathrm{Im}(\alpha) I(\mathbf{r}). \tag{2.19}$$

Note that the equations that have been derived are valid for any polarizable neutral particle in an oscillating electric field, regardless of whether the atom is in a near-resonant or far off-resonant field.

Polarisability

To calculate the polarisability, α, first consider the atom in the classical Lorentz oscillator model [95]. In this classical model, an electron is elastically bound to

the atom core, oscillating with an eigenfrequency ω_0 which corresponds to the optical transition frequency. The driving force causing the oscillations is the laser's electric field. The classical equation of motion for the electron is then [96]:

$$F = m_e\ddot{x}(t) = -eE(t) - m_e\Gamma\dot{x}(t) - m_e\omega_0^2 x(t). \tag{2.20}$$

The first term on the right hand side of equation 2.20 is the driving force and contains the electronic charge, e. The second term is a damping term representing the rate at which the polarisation will decay once the electric field is removed. This term includes the classical damping rate Γ and the mass of the electron, m_e. The third term is the restoring force of the electron which is analogous to a spring force with spring constant ω_0^2 (imagining the electron is connected by a spring to the heavy nucleus). Equation 2.20 is a second order differential equation which can be solved using the substitution $E(t) = E_0 \exp(-i\omega t)$ and $x(t) = x_0 \exp(-i\omega t)$ to give:

$$x_0 = \frac{-eE_0}{m_e}\frac{1}{\omega_0^2 - \omega^2 - i\omega\Gamma}. \tag{2.21}$$

Then, using the relation $p(t) = -ex(t) = \alpha E(t)$, a solution for the polarisability can be found as:

$$\alpha(\omega) = \frac{-e^2}{m_e}\frac{1}{\omega_0^2 - \omega^2 - i\omega\Gamma}, \tag{2.22}$$

$$\text{where} \quad \Gamma = \frac{e^2\omega_0^2}{6\pi\epsilon_0 m_e c^3} \tag{2.23}$$

is the on-resonance damping rate due to the radiative energy loss.

Now considering a semi-classical approach, the polarisability can be calculated by modelling the atom as a two-level quantum system interacting with the classical radiation field. In ODTs, saturation effects can be neglected because they operate at large detunings and hence the atom is generally in the ground

state. With this allowed neglection, the semi-classical model gives the exact same result as the classical one except with a modification to the damping rate, which now must be calculated using the dipole matrix element between the ground and excited state, $|\langle \mathrm{e}|\mathbf{d}|\mathrm{g}\rangle|^2$:

$$\Gamma = \frac{\omega_0^3}{3\pi\epsilon_0\hbar c^3}|\langle \mathrm{e}|\mathbf{d}|\mathrm{g}\rangle|^2. \tag{2.24}$$

However, the classical equation for Γ given in equation 2.23 does provide a reasonable approximation for many atoms including the D lines of the alkali atoms Na, K, Rb, and Cs where the classical result agrees with the real decay rate to within a few percent.

With the expression for the polarisability, the final formulae for the dipole potential and scattering rate can be derived. By separating the real and imaginary parts of the polarisability and substituting it into equations 2.15 and 2.19, we obtain the results:

$$U_{\mathrm{dip}}(\mathbf{r}) = -\frac{3\pi c^2}{2\omega_0^3}\left(\frac{\Gamma}{\omega_0-\omega}+\frac{\Gamma}{\omega_0+\omega}\right)I(\mathbf{r}), \tag{2.25}$$

and

$$\Gamma_{\mathrm{sc}}(\mathbf{r}) = \frac{3\pi c^2}{2\hbar\omega_0^3}\left(\frac{\omega}{\omega_0}\right)^3\left(\frac{\Gamma}{\omega_0-\omega}+\frac{\Gamma}{\omega_0+\omega}\right)^2 I(\mathbf{r}). \tag{2.26}$$

To understand the implications of these equations, we simplify them using the rotating wave approximation (RWA) [97]. This is valid when the laser frequency is relatively close to the resonant frequency i.e. $\omega \approx \omega_0$ and the detuning $\Delta = \omega_0 - \omega \ll \omega_0 + \omega$. Note that this approximation is used only to conceptualise the physical properties of ODTs because the ODT presented in this thesis is relatively far from resonance and is designed using the non-

simplified equations. In the RWA, the above equations become:

$$U_{\mathrm{dip}}(\mathbf{r}) = -\frac{3\pi\Gamma c^2}{2\omega_0^3\Delta} I(\mathbf{r}), \tag{2.27}$$

and

$$\Gamma_{\mathrm{sc}}(\mathbf{r}) = \frac{3\pi c^2}{2\hbar\omega_0^3}\left(\frac{\Gamma}{\Delta}\right)^2 I(\mathbf{r}). \tag{2.28}$$

These equations highlight two important consequences for ODTs:

1. *Sign of detuning and potential:* Firstly, the sign of the dipole potential is dependent on the detuning, $\Delta = \omega_0 - \omega$. For red-detuned beams ($\Delta < 0$), the potential is negative. Hence, potential minima are found where the light intensity is maximum and atoms can therefore be trapped at the beam focus. Conversely, blue detuned traps ($\Delta > 0$) create positive potentials and trapping minima occur at intensity minima. These are the two main classes of dipole traps. In this experiment red detuning is used to turn the $\sim$ Gaussian laser beam into an ODT.
2. *Scaling with intensity and detuning:* The dipole potential scales with I/Δ but the scattering rate scales as I/Δ^2. This explains why large detuning is typically used in ODTs: to ensure that the trapping dipole force dominates over scattering. Then a high intensity is used to create a sufficient trapping potential depth.

Multi-level Atoms

In real atoms used in dipole traps, the electronic transitions have a complex sub-structure. To describe this, we use a quantum mechanical approach which provides useful information on the motion of multi-level atoms in far-detuned light. The effect of this far-detuned light field on the atomic energy levels is

treated as a second order perturbation of the electric field. From perturbation theory, interaction of the atom with the light field leads to an energy shift of non-degenerate atomic states $|i\rangle$ given by:

$$\Delta E_i = \sum_{j \neq i} \frac{|\langle j|\mathcal{H}_{AL}|i\rangle|^2}{\varepsilon_i - \varepsilon_j} \tag{2.29}$$

where ε_i is the unperturbed energy of the i-th state and $\mathcal{H}_{AL} = -\hat{\mu}\,\mathbf{E}$ is the interaction Hamiltonian between the atom and light with $\hat{\mu} = -e\,\mathbf{r}$ representing the electric dipole operator. Here we use a 'dressed state' approach [98] considering the combined system of the atom and the light field. For a two-level atom in the ground state, g, the atom has zero internal energy whereas the light field has energy $n\,\hbar\,\omega$ where n is the number of photons. This results in the total energy of the unperturbed state, $\varepsilon_g = n\,\hbar\,\omega$. When the atom absorbs a photon and moves to the excited state, e, the internal energy $\hbar\,\omega_0$ and field energy $(n-1)\hbar\,\omega$ combines to become $\varepsilon_e = \hbar\,\omega_0 + (n-1)\hbar\,\omega = -\hbar\,\Delta + n\,\hbar\,\omega$. Therefore, the denominator of equation 2.29 becomes $\varepsilon_i - \varepsilon_j = \hbar\,\Delta$. Then for our two-level atom with the incident light represented by an oscillating electric field, equation 2.29 simplifies to:

$$\Delta E = \pm\frac{|\langle e|\mu|g\rangle|^2}{\hbar\,\Delta}|E|^2 = \pm\frac{3\pi c^2}{2\omega_0^3}\frac{\Gamma}{\Delta}I(\mathbf{r}) \tag{2.30}$$

where the plus and minus signs represent the energy shifts of the excited and ground states respectively and equations 2.16 and 2.24 have been used to substitute the dipole matrix element with the damping rate. From the above equation, we can see that the energy shift is dependent on the intensity of the laser beam. For the case of low saturation, the atom spends most of its time in the ground state and therefore the light-shifted ground state can be interpreted as the potential for the motion of the atoms. This is illustrated in figure 2.11

which demonstrates the energy level shifts in a two-level atom created by a Gaussian beam.

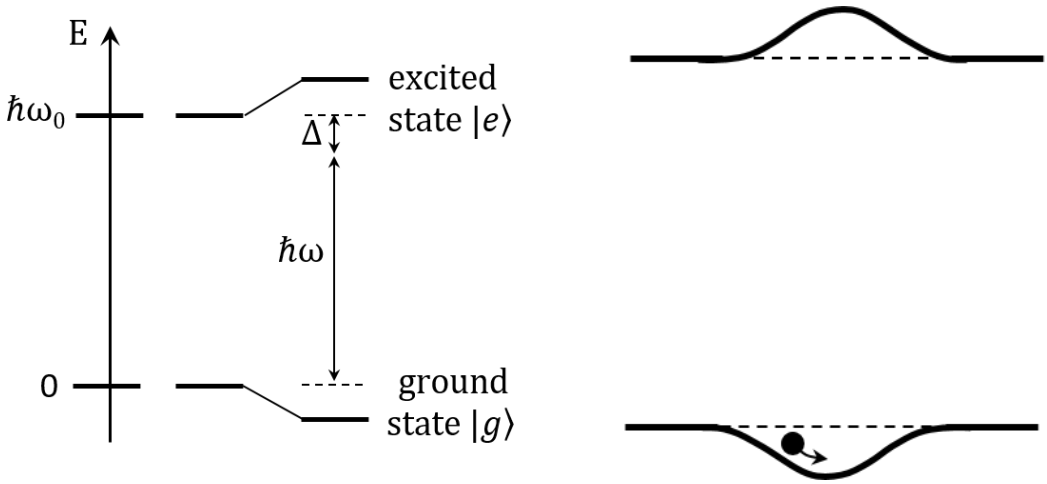

(a) Energy Shifts **(b)** Gaussian Beam Profile

Figure 2.11: Optically induced light shifts for a two-level atom. (a) Light detuned below resonance with $\Delta < 0$ (i.e. red-detuned) shifts the ground state energy down and the excited state energy up equally. (b) A Gaussian beam, with inhomogenous intensity, can be used to create a potential well for atom trapping. [43]

To apply equation 2.29 to a multi-level atom, all possible dipole matrix elements $\mu_{ij} = \langle e_j|\mu|g_i\rangle$ between specific electronic ground $|g_i\rangle$ and excited states $|e_j\rangle$ have to be taken into account. For a specific transition, these matrix elements become [99]:

$$\mu_{ij} = c_{ij}\|\mu\| \tag{2.31}$$

where $\|\mu\|$ is a reduced matrix element and c_{ij} is the real transition or Clebsch-Gordan coefficient. This coefficient accounts for the coupling strength between specific sub-levels i and j and depends on laser polarisation and the electronic and nuclear angular momenta. We can now write the energy shift of the

electronic ground state of a multi-level atom in the form:

$$\Delta E_i = \frac{3\pi c^2 \Gamma}{2\omega_0^3} I(\mathbf{r}) \sum_j \frac{c_{ij}^2}{\Delta_{ij}} \tag{2.32}$$

where the summation is performed over all electronically excited states $|e_j\rangle$. Therefore, to calculate the state-dependent ground-state potential, $U_{\mathrm{dip},i} = \Delta\varepsilon_i$, we must sum the contributions from all coupled excited states, taking into account the relevant line strengths c_{ij} and detunings Δ_{ij}.

Alkali Atoms Rb specifically

As previously described in section 2.2.1, alkali atoms have certain advantages that result in them often being used in laser cooling and trapping experiments. These atoms possess the well-known and relevant D-line doublet (D1 and D2 transitions) due to spin-orbit coupling in the excited state. Coupling of nuclear spin then produces hyperfine structure in both the ground and excited states. Specifically in this experiment, the D2 line of Rb-87 is used (see figure 2.8 for the level scheme).

Using equation 2.32, we can generally derive the potential of a ground state with total angular momentum F and magnetic quantum number m_F:

$$U_{\mathrm{dip}}(\mathbf{r}) = \frac{\pi c^2 \Gamma}{2\omega_0^3} \left(\frac{1 - \mathcal{P} g_F m_F}{\Delta_1} + \frac{2 + \mathcal{P} g_F m_F}{\Delta_2} \right) \tag{2.33}$$

and the scattering rate is:

$$\Gamma_{\mathrm{sc}}(\mathbf{r}) = \frac{\Gamma}{\hbar \Delta} U_{\mathrm{sc}} = \frac{\pi c^2 \Gamma^2}{2\hbar \omega_0^3} \left(\frac{1 - \mathcal{P} g_F m_F}{\Delta_1^2} + \frac{2 + \mathcal{P} g_F m_F}{\Delta_2^2} \right) \tag{2.34}$$

where g_F is the Landé factor (calculated from the various relevant quantum numbers [100]), $\mathcal{P}$ characterises the polarisation of the laser ($\mathcal{P} = 0, \pm 1$ for

linearly and circularly $\sigma^{\pm}$ light respectively), and Δ_i is the detuning of the Di transition (i.e. the two terms in the brackets in the above equations represent the contributions from the D2 and D1 lines to the total dipole potential respectively). The above equations are valid for both linearly and circularly polarized light as long as all optical detunings are large compared to the excited-state hyperfine splitting.

Types of Optical Dipole Traps

This section describes the three geometries of ODT that can be generated using Gaussian beams.

Focused beam: The simplest set-up for an optical dipole trap with three-dimension spatial confinement is a focused Gaussian beam red-detuned far from resonance (FB trap). This trapping geometry can be seen in figure 2.12 (a). The spatially dependent intensity of this beam is given by:

$$I_{\mathrm{FB,circ}}(r,z) = \frac{2P}{\pi w^2(z)} \exp\left(\frac{-2r^2}{w^2(z)}\right), \tag{2.35}$$

assuming it's propagating along the z-axis with power P, and where r represents the radial coordinate and $w(z)$ denotes the $1/e^2$ radius of the beam which is dependent on the axial coordinate z according to:

$$w(z) = w_0 \sqrt{1 + \left(\frac{z}{z_R}\right)^2} \tag{2.36}$$

where $z_R = \pi w_0^2/\lambda$ is the Rayleigh length, and w_0 is the radius of the beam at the focus i.e. the beam 'waist'. Notice that z_R is larger than w_0 by a factor of $\pi w_0/\lambda$. Hence, the atoms are confined more strongly in the radial than in the longitudinal direction. This is a result of a larger intensity gradient in the

radial direction. By substituting the intensity distribution into equation 2.27, we can obtain an equation for the dipole potential of the focused beam trap. To find the trapping frequency in the axial and radial directions, the potential can be approximated by a cylindrical symmetric harmonic oscillator. This assumption can be made as long as the thermal energy of the atomic ensemble, $k_B T$, is significantly lower than the potential depth, U_0. Then, the potential becomes [43]:

$$U_{\mathrm{FB,circ}}(r,z) \simeq -U_0\left(1-2\left(\frac{r}{w_0}\right)^2-\left(\frac{z}{z_R}\right)^2\right) = -U_0+\frac{1}{2}m\omega_r^2 r^2+\frac{1}{2}m\omega_z^2 z^2 \tag{2.37}$$

where the trap depth, $U_0 = |U(r=0,z=0)|$, is the magnitude of the potential at the centre of the trap where $w = w_0$, and ω_r and ω_z are the trapping frequencies in the radial and axial directions respectively, determined by:

$$\omega_r = \sqrt{\frac{4U_0}{mw_0^2}}, \tag{2.38}$$

and

$$\omega_z = \sqrt{\frac{2U_0}{mz_R^2}}. \tag{2.39}$$

For non-circularly symmetric beams where $w_{0x} \neq w_{0y}$, the intensity of the beam is modified to:

$$I_{\mathrm{FB,ellip}}(x,y,z) = \frac{2P}{\pi w_x w_y}\exp\!\left(\frac{-2x^2}{w_x^2(z)}+\frac{-2y^2}{w_y^2(z)}\right). \tag{2.40}$$

The harmonic approximation of the trapping potential then becomes:

$$\begin{aligned} U_{\mathrm{FB,ellip}}(x,y,z) \simeq & -U_0\left(1-\frac{2x^2}{w_x^2}-\frac{2y^2}{w_y^2}-\frac{1}{2}z^2\left(\frac{1}{z_{Rx}^2}+\frac{1}{z_{Ry}^2}\right)\right) \\ & = -U_0+\frac{1}{2}m\omega_x^2x^2+\frac{1}{2}m\omega_y^2y^2+\frac{1}{2}m\omega_z^2z^2, \end{aligned} \tag{2.41}$$

with trap frequencies:

$$\omega_x = \sqrt{\frac{4U_0}{mw_x^2}}, \tag{2.42}$$

$$\omega_y = \sqrt{\frac{4U_0}{mw_y^2}}, \tag{2.43}$$

and

$$\omega_z = \sqrt{\frac{2U_0}{m}\left(\frac{1}{2z_{Rx}^2} + \frac{1}{2z_{Ry}^2}\right)} = \sqrt{\frac{2U_0}{mz_{R\text{eff}}^2}}, \tag{2.44}$$

where the effective Rayleigh range for this elliptical Gaussian beam is given by:

$$z_{R\text{eff}} = \frac{z_{Rx}z_{Ry}}{\sqrt{1/2\left(z_{Rx}^2 + z_{Ry}^2\right)}}. \tag{2.45}$$

Note that the average trapping frequency is simply given by the geometric mean:

$$\omega_{av} = \left(\omega_x\omega_y\omega_z\right)^{\frac{1}{3}} \tag{2.46}$$

The atom trapping volume can be approximated as a cylinder with radius and length determined by the beam waist and atom temperature according to [101]:

$$V = \pi w_x w_y z_{R\text{eff}} \ln\left(\frac{1}{1-\eta}\right)\sqrt{\frac{1-\eta}{\eta}} \tag{2.47}$$

where $\eta = k_B T/|U_0|$.

Standing wave: If instead of having a simple red-detuned Gaussian beam, where atoms are trapped at the focus, we have two red-detuned Gaussian beams opposing each other to form a standing wave, then the atoms are trapped at the antinodes (SW trap). This provides extremely tight confinement in the axial direction as can be observed in figure 2.12 (b). Assuming the standing

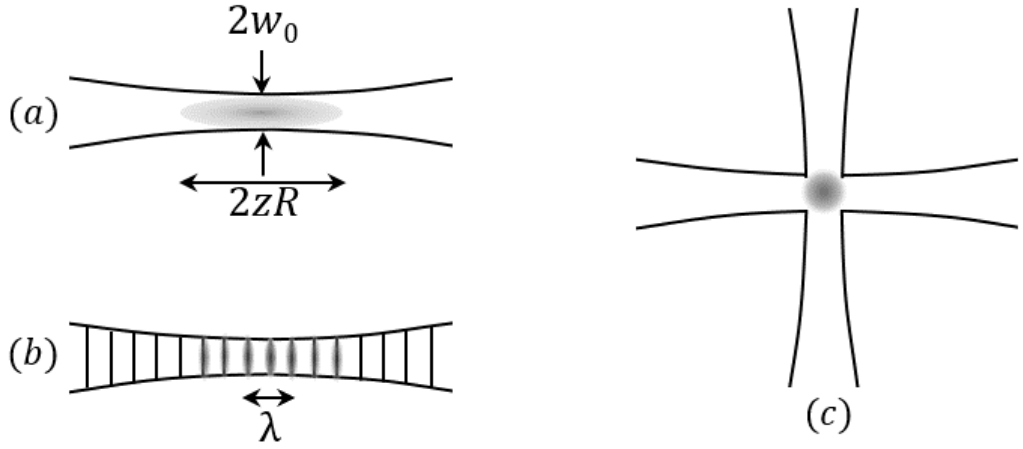

Figure 2.12: Optical dipole trap geometries including (a) single-beam, (b) standing wave, and (c) crossed-beam. The atoms trapped are shown in grey.

wave is orientated along the z-axis, the potential can be written as:

$$U_{SW}(r,z) \simeq -U_0 \cos^2(kz) \left(1 - 2\left(\frac{r}{w_0}\right)^2 - \left(\frac{z}{z_R}\right)^2\right). \tag{2.48}$$

Due to interference, the potential depth is four times larger than that of the single focused beam trap discussed previously with the same power in each beam (or double the trap depth if you split the single beam power to create the two beams). The axially trapping potential is spatially modulated with period $\lambda/2$. This results in a one-dimensional lattice of flat, elongated atomic sub-ensembles. The tight confinement along the axial direction creates large oscillation frequencies at the trap centre:

$$\omega_z = \sqrt{\frac{4U_0}{m(\lambda/2)^2}}. \tag{2.49}$$

This frequency decreases as you travel further along the z-axis due to the decreasing light intensity. Note that by comparing equation 2.49 to equation 2.44, it can be observed that the z direction trapping frequency will be orders

of magnitude larger for the lattice than for the single beam. This is because, in addition to the factor of 2 doubling to a factor of 4, the distance parameter in the denominator is half the wavelength rather than the Rayleigh distance. Note that for Rb-87 in our experiment, the axial trapping frequency is 10^5 times larger for the lattice than the single beam trap.

The obvious advantage of this trap is that with a strong trapping force in the axial direction, a lower intensity beam can be used to trap atoms resulting in smaller photon scattering rates, as compared to the single focused beam trap. Furthermore, the high atom density in a subensemble creates favourable conditions for further cooling via evaporation (see section 2.2.3). However, the subensembles encompass a relatively small spatial area as compared to the FB trap and radial confinement is still relatively weak, resulting in fewer atoms being initially trapped from the pre-cooled MOT.

Crossed beam: The single focused beam trap, with weak confinement in the axial direction and strong confinement in the radial direction, results in a highly anisotropic atomic cloud. Furthermore, in a standing wave trap, the already anisotropically distributed FB trap is further split into anisotropic subensembles, with very tight confinement in the axial direction. One solution to obtain an approximately isotropic atom cloud is to add a second trapping beam perpendicular to the first, with the same waist and the foci aligned: see figure 2.12 (c). Note that the second beam requires orthogonal polarisation to the first to avoid interference effects [43]. For this crossed-beam trap (CB trap), the dipole potential is approximated as:

$$U_{CB,\mathrm{circ}}(x,y,z) \simeq -U_0\left(1-\frac{x^2+y^2+2z^2}{\omega_0^2}\right) \tag{2.50}$$

where it has been assumed that we have circularly symmetric beams. The

geometry of a crossed beam trap results in a strong, almost isotropic trapping frequencies. Note that the effective potential depth here is $U_0/2$ because atoms with energies larger than this can leave the trap along one of the beams. However, this central trap depth still has the same magnitude as the single focused beam trap as here we have double the intensity.

If the beams are elliptical instead of circular the equation for the potential becomes:

$$\begin{aligned} U_{\mathrm{CB,ellip}}(x,y,z) \simeq & -U_{0_1}\left(1-\frac{2x^2}{w_{x_1}^2}-\frac{2y^2}{w_{y_1}^2}-\frac{1}{2}z^2\left(\frac{1}{z_{Rx_1}^2}+\frac{1}{z_{Ry_1}^2}\right)\right) \\ & -U_{0_2}\left(1-\frac{2x^2}{w_{x_2}^2}-\frac{2y^2}{w_{y_2}^2}-\frac{1}{2}z^2\left(\frac{1}{z_{Rx_2}^2}+\frac{1}{z_{Ry_2}^2}\right)\right), \end{aligned} \tag{2.51}$$

where the subscripts 1 and 2 refer to the two beams. In the harmonic approximation, the trap frequencies are:

$$\omega_x = \sqrt{\frac{4U_{0_1}}{mw_{x_1}^2}+\frac{4U_{0_2}}{mw_{x_2}^2}}, \tag{2.52}$$

$$\omega_y = \sqrt{\frac{4U_{0_1}}{mw_{y_1}^2}+\frac{2U_{0_2}}{mz_{R\mathrm{eff}_2}^2}}, \tag{2.53}$$

and

$$\omega_z = \sqrt{\frac{4U_{0_2}}{mw_{x_2}^2}+\frac{2U_{0_1}}{mz_{R\mathrm{eff}_1}^2}}. \tag{2.54}$$

The atoms in this trap are localised to the overlapping volume of the two beams and the atom density in this region is high. Therefore, these crossed beam traps provide a compromise between trapping volumes and tight confinements/ atom densities. However, they are not always practically feasible due to the requirement of an additional beam input. This is the case in this experiment where lack of optical access prevented this trap type from being used, as can be

observed in the system design section 4.1. However, if the ODT proposed in this work produces insufficient atoms (after evaporative cooling) for the gravimetry measurement, then future iterations could modify the vacuum system design to accommodate a cross-beam ODT.

2.2.3 Evaporative Cooling

This description follows Luiten (1996): 'Kinetic theory of evaporative cooling of a trapped gas' [102].

Evaporative cooling is based on removing higher than average energy atoms from a trapped gas. In a trap of finite depth, atoms with energy larger than the trap depth can leave i.e. they are 'evaporated' away. The remaining atoms then rethermalise via elastic interatomic collisions to a new equilibrium with a lower average energy and, therefore, with a lower temperature. These collisions also increase the energies of some atoms to above the trap depth, allowing the evaporation to continue. However, as the temperature decreases, the number of atoms able to leave the trap decreases exponentially. Therefore, the cooling is eventually either balanced by an opposing heating process or becomes negligibly small. To allow the evaporation to proceed, the trap depth can be continuously lowered as the gas cools, this is called 'forced evaporation'. This process is depicted schematically in figure 2.13. Note that this process is intrinsically lossy in terms of atom number. However, as the atoms sink lower in the potential, the density can remain the same or even increase which allows runaway evaporation to occur.

It is described in Luiten that the evaporating gas can, to good approximation, be described as a Boltzmann distribution truncated at the trap depth. To do so, it is assumed that the distribution of atoms in phase-space (refer to 2.2.4) obeys "sufficient ergodicity" i.e. that their distribution depends only on their

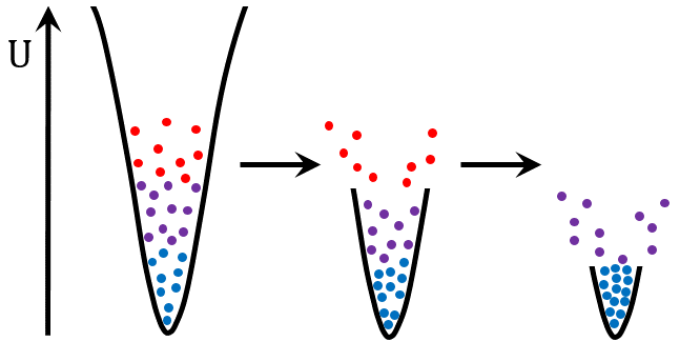

Figure 2.13: The evaporative cooling process: atoms are trapped in a potential where the coldest atoms sink lower in the well. By reducing the trap depth, the hottest atoms are selectively evaporated from the trap. The remaining atoms then rethermalise to lower temperatures.

energy. The motion is sufficiently ergodic if most atoms with a total energy higher than the trap depth are removed before colliding with another atom. This is the case when the collision mean free path length of the atoms is much larger than the size of the gas cloud: generally correct for cold atom trapped gases. Furthermore, the gas is assumed to be classical which is true if the temperatures are significantly higher than the quantum level spacing of an atom in the trap.

This approach leads to equations for: the rate of evaporation; the atom number decrease over time; and the energy (temperature) decrease over time, which show a good agreement with experimental results [103].

Evaporative Cooling in Optical Dipole Traps

The previously described optical dipole trap (section 2.2.2) can be used as the trapping potential for evaporative cooling. Then forced evaporative cooling can be performed by simply lowering the laser power to decrease the trap depth.

Evaporative Cooling using Optical Lattices

An issue when evaporative cooling in optical dipole traps* is that, as the trap depth U_0 decreases, so does the average trapping frequency ω_{av} (according to $\omega_{av} \propto U_0^{2/3}$, see 2.46). In turn, the elastic collision rate will also decrease which has the negative consequence of slowing the rethermalization. This is normally the limiting time factor in producing ultra-cold atoms in ODTs.

However, as previously described (see 2.2.2), optical dipole lattice traps create atomic sub-ensembles with double the trap depth compared to the single beam ODT (assuming the single beam power is split in two). Furthermore, the trapping frequency in the axial direction ω_z is increased by a factor of $\sim 10^5$ (for the specific wavelength of light and transition in question) due to the dramatically decreased trapping distance. This results in a much higher average trapping frequency for the optical lattice trap and hence an increased atom collision rate. This is favourable for reducing the time of evaporation.

However, too high a collision rate can result in too many atoms being ejected from the trap and result in a low final atom number which is not ideal for a high resolution atom interferometry based gravity measurement (see 2.1). Hence, for full flexibility, this experiment is designed so that the amount of power split between the beams can be varied to change the balance between a dipole trap and a lattice. This allows control of the trap depth and frequency so that by optimisation the most favourable conditions for atom interferometry can be found (in terms of atom number, temperature and speed of generation). Once built, this balance would be found experimentally.

*This is not an issue for magnetic traps whose trap depth can be decreased without affecting the trap frequency

2.2.4 Bose-Einstein Condensates

Effective evaporative cooling leads to compression in phase space. Therefore, it can be used as a method to reach a Bose-Einstein Condensate (BEC). A BEC, described in literature [84], is a state of matter where a bosonic gas has been cooled close to absolute zero and exhibits quantum degeneracy. The transition to a BEC occurs at a specific phase-space density*, D [53]:

$$D = n\lambda_{dB} \geqslant 2.612 \tag{2.55}$$

where n is the atomic number density and λ_{dB} is the thermal de Broglie wavelength, for an atom of mass m, which is given by:

$$\lambda_{dB} = \sqrt{\frac{2\pi\hbar^2}{mkT}}. \tag{2.56}$$

BECs have been shown to have no adverse affects on the atom interferometry measurement and, due to the decreased expansion of these ultra-cold condensates, have experimentally produced an improved measurement contrast when compared to a thermal source [104].

2.3 Summary of the Experimental Cycle

A summary of the experimental process that would (ultimately) be employed in this project to generate the required ultra-cold atoms and perform a gravity measurement is as follows. Firstly, a 2D MOT of pre-cooled atoms is generated and used to load a 3D MOT in a few seconds. The 3D MOT will be optimised for transfer to the ODT by implementing compression and additional cooling.

*Phase-space density = the number of atoms in a box with sides of one thermal de Broglie wavelength [85]

The MOT can be compressed to increase the cloud's density, by increasing the magnetic field gradient and detuning of the cooling beams, before loading into the ODT is performed. The intensity of the cooling beam is then reduced and the detuning is also optimised so that sub-Doppler cooling processes can dominate over laser cooling (refer to 2.2.1). This allows the atoms to reach cooler temperatures which will allow a higher proportion to be captured in the finite trap depth ODT. Note that simultaneously, the repump beam intensity must also be reduced/ turned off as the photons impart enough energy to be able to escape the ODT. These methods of compressing and cooling a MOT to load an ODT have been performed successfully in literature [56, 105, 106].

After loading, evaporative cooling can be performed to further reduce the atom temperature. This will be done in a hybrid single-beam - lattice ODT to optimise speed of evaporation and final number trapped. Once cooled, ideally to quantum degeneracy, the atoms can be released from the trap and allowed to free fall. This enables the final step of atom interferometry based gravimetry measurements. This process can then be repeated to obtain multiple measurements and build up a gravity map.

2.4 Optical Cavities

2.4.1 Cavity Resonance: Finesse & Q-factor

An optical cavity, or resonator, is formed when light repeatedly reflects in a closed path between two, or more, reflecting surfaces i.e. between mirrors. Due to interference, only specific radiation frequencies will be allowed within the cavity, with the rest being suppressed due to destructive interference. These are the longitudinal (or axial) cavity eigenmodes [107]. These cavity modes

occur when the round-trip phase shift is equal to an integer multiple of 2π as expressed by the following equation

$$\frac{\omega L}{c} = 2\pi n \tag{2.57}$$

where ω is the angular frequency of the light, L is the total round trip distance, and n is an integer [107]. At these 'resonant frequencies', there is a peak in the transmission of light through the cavity as illustrated in figure 2.14. From equation 2.57, it can be shown that the frequency spacing between resonant cavity modes is given by

$$\Delta\nu = \frac{c}{L}. \tag{2.58}$$

This is known as the cavity Free Spectral Range (FSR) which is also equal to the inverse of the round trip time, T.

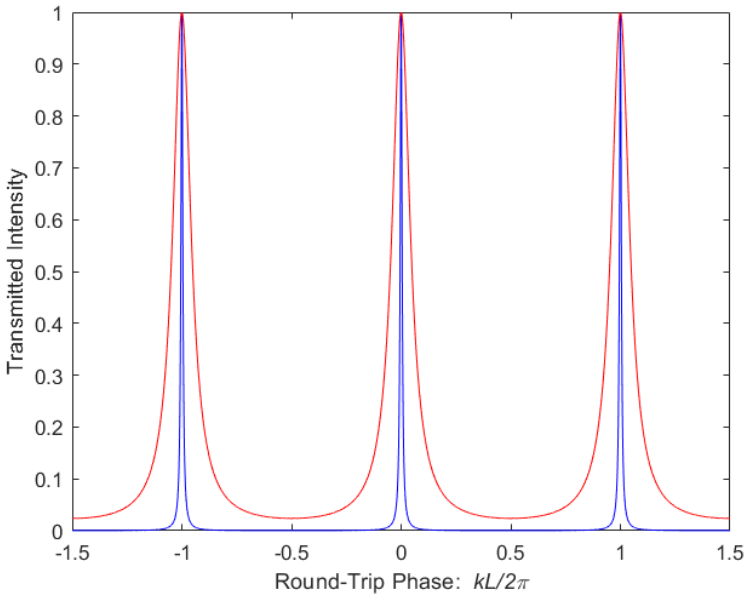

Figure 2.14: Theoretical transmitted profile of a field incident on a cavity. On resonance there is a sudden spike in transmitted intensity. Red and blue curves show finesses of 10 and 100 respectively.

Another parameter of note is the Full Width at Half Maximum (FWHM)

which describes the width of the resonant peak when it falls to half its maximum value. In frequency space it describes the linewidth (or bandwidth) of the resonances. A smaller FWHM makes it easier to distinguish different cavity resonances. This can be generated from e.g. higher radius of curvature mirrors which result in narrower resonances.

By taking the ratio of the FSR to the FWHM, a quantity is obtained known as the cavity finesse [107], $\mathcal{F}$, where

$$\mathcal{F} = \frac{\text{FSR}}{\text{FWHM}} = \frac{\pi}{2\arcsin\left(\frac{1-\sqrt{\rho}}{2\sqrt[4]{\rho}}\right)}. \tag{2.59}$$

where ρ is the fractional field amplitude remaining after each round-trip. The finesse determines the resolution of the cavity i.e. it describes its ability to resolve spectral features. Equivalently, for an infinitely narrow input, the finesse defines the width of the measured spectrum [108]. From equation 2.59 notice that the finesse is dependent only on the cavity losses, but not on the length of the cavity. Note that, in reality, the total cavity finesse has several contributing factors including finesse due to mirror surface quality and illumination conditions. However, for a well machined and aligned cavity, the 'reflectivity' finesse described previously will be the dominant factor [108].

By multiplying the finesse by the resonant frequency and dividing by the FSR, the quality factor, or Q factor, of a cavity is defined. This can be shown to be equal to the ratio of the resonant frequency to the cavity bandwidth. It is a dimensionless quantity that describes the losses of the cavity and it is proportional to the average lifetime of a photon in the cavity, $\tau = \frac{T}{1-\rho}$ where T is the time is takes to complete one round trip. A higher Q factor equates to lower losses [107].

2.4.2 Cavity Beam Waist & Stability

The following description follows closely to that in Chapter 1 of "Quantum Electronics for Atomic Physics and Telecommunication" by W. Nagourney [109].

The Paraxial Wave Equation

In free space, electromagnetic waves are described by the scalar wave equation

$$\nabla^2 u - \frac{1}{c^2}\frac{\partial^2 u}{\partial t^2} = 0 \tag{2.60}$$

where u is any Cartesian field component i.e. E_x, E_y, or E_z. If the wave is monochromatic, this equation becomes

$$\nabla^2 u + k^2 u = 0 \tag{2.61}$$

where k is the magnitude of the wave vector. The paraxial approximation requires that there is a small angle between the normal of the wavefront and a fixed beam axis, which is chosen as the z-axis of the Cartesian coordinate system. It is assumed that the beam can be modelled as a plane wave which is spatially modulated by a slowly varying function, $\psi(x, y, z)$. Therefore,

$$u(x, y, z) = \psi(x, y, z)e^{-ikz}. \tag{2.62}$$

For the paraxial approximation to be satisfied, $\psi(x, y, z)$ must vary significantly more slowly along the z-axis than the $x-$ and y-axes. Hence, $\partial^2\psi/\partial z^2$ is negligible compared to the other second derivatives of x and y. Therefore, when substituting equation 2.62 into the the wave equation 2.60, we obtain the

Paraxial wave equation:

$$\nabla_t^2 \psi - 2ik\frac{\partial \psi}{\partial z} = 0 \tag{2.63}$$

where ∇_t^2 is the transverse Laplacian $= \partial/\partial x^2 + \partial/\partial y^2$.

Gaussian Waves

One simple solution to the Paraxial wave equation, can be found by substituting a trial solution of the form

$$\psi(x, y, z) = P(z) \exp\left(-ik\frac{x^2 + y^2}{2q(z)}\right) \tag{2.64}$$

where $P(z)$ is the phase term and $q(z)$ is the complex beam parameter. This complex beam parameter can be written as

$$\frac{1}{q(z)} = \frac{1}{R(z)} - i\frac{\lambda}{\pi w(z)^2} \tag{2.65}$$

where $R(z)$ and $w(z)$ are two real parameters describing the wavefront radius and waist radius respectively.

By substituting equation 2.65 into the beam equation 2.62 and our trial solution, equation 2.64, we find that this solution of the wave equation has a Gaussian radial dependence, i.e. it is a Gaussian beam, whose properties are described entirely by the complex beam parameter, $q(z)$. Therefore, this complex beam parameter can be used to specify the properties of the Gaussian beam at any point along the z-axis. Figure 2.15 demonstrates that a Gaussian beam never focuses to a point, but to a minimum size, defined as the beam waist with $1/e^2$ radius, w_0. This occurs when the wavefront has infinite radius, $R = \infty$, i.e. it is a plane. By setting this R value in equation 2.65, the value of

q at the waist is found:

$$q_0 = i\frac{n\pi w_0^2}{\lambda}. \tag{2.66}$$

Furthermore, if z is defined as the distance from the waist, then q as a function of the distance from the waist, z, is:

$$q(z) = q_0 + z = i\frac{n\pi w_0^2}{\lambda} + z. \tag{2.67}$$

Using equations 2.65 and 2.67, we find the corresponding evolution of w and R along the z-axis

$$w(z) = w_0\sqrt{1 + \left(\frac{z}{z_R}\right)^2} \tag{2.68}$$

$$R(z) = z + \frac{z_R^2}{z} \tag{2.69}$$

where we remember the Rayleigh length, $z_R = n\pi w_0^2/\lambda$, which here is the distance from the waist ($z = 0$) to the z value where the beam size increases by a factor of $\sqrt{2}$. This is illustrated in figure 2.15.

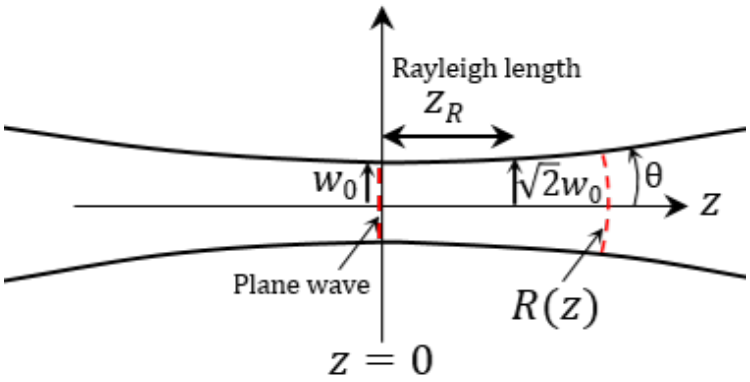

Figure 2.15: Gaussian beam radial intensity profile where the beam focuses to a waist w_0. Wavefronts are shown in red dash.

2.4.3 Transmission, Reflection & Power Enhancement

As previously described in chapter 1, a key advantage of using a cavity in this experiment is the power enhancement capabilities it possesses. To quantify this, imagine four concave mirrors separated by distance d with radii of curvature, R_i, where the subscript i refers to a particular mirror in the cavity. Assume each mirror has reflectivity and transmission coefficients r_i and t_i respectively where, for lossless mirrors, $r_i^2 + t_i^2 = 1$. Therefore, the fractional field amplitude remaining after each round-trip, ρ, is given by $\sqrt{\rho} = r_1 r_2 r_3 r_4$. This 'bow-tie cavity' arrangement is shown in figure 2.16.

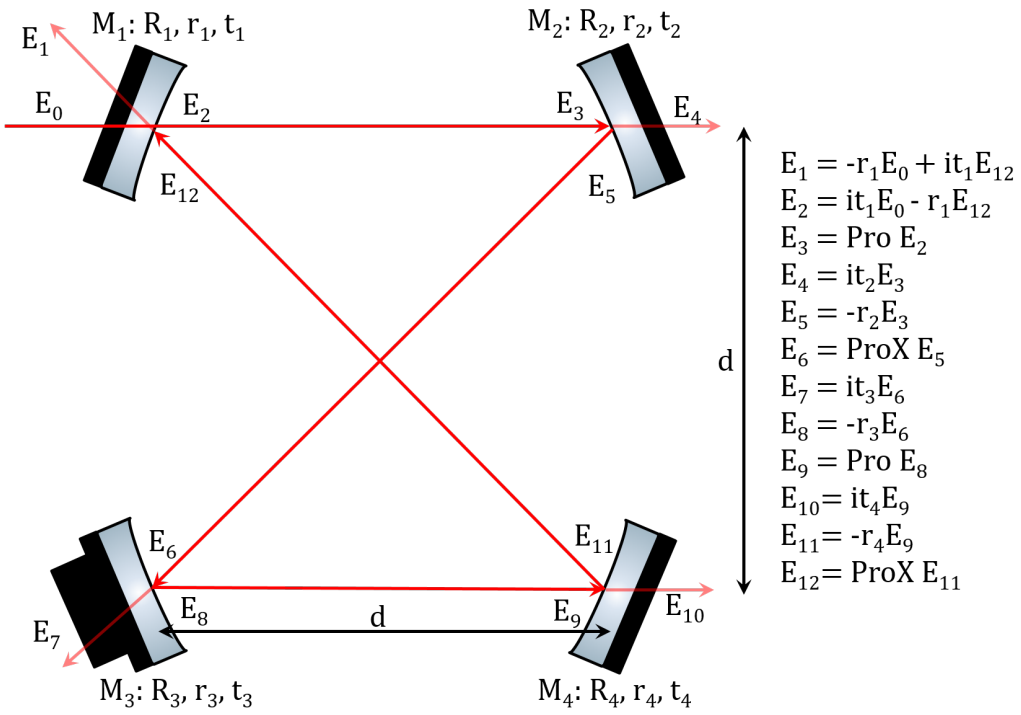

Figure 2.16: A four mirror, bow-tie cavity set-up with a distance d in-between mirrors. Electric field amplitude, E_0 is incident upon mirror 1 and an amount, E_2 is transmitted into the cavity. The light then continues to circulate around the cavity and the equations for the electric field at various ports are given on the right hand side. Each mirror has a radius of curvature R_i, reflectivity coefficient r_i, and transmission coefficient t_i where the subscript i represents the mirror number. Pro= e^{-ikd} and ProX= $e^{-\sqrt{2}ikd}$ represent the phase shift gained through travelling a distance of d and $\sqrt{2}d$ respectively.

The extent by which the input power is magnified within this cavity is named the 'enhancement factor', EF, and is given by

$$\mathrm{EF} = \frac{|E_{12}|^2}{|E_0|^2} \tag{2.70}$$

where E_0 is the input electric field amplitude, E_{12} is the steady state electric field circulating within the cavity and the complex conjugate has been taken to convert electric field into intensity. Using the equations given in figure 2.16 and the fact that the Pro and ProX terms are equal to unity on resonance, equation 2.70 becomes

$$\mathrm{EF} = \frac{(1 - r_1^2)(r_2 r_3 r_4)^2}{(1 - r_1 r_2 r_3 r_4)^2}. \tag{2.71}$$

This equation can be used to calculate the mirror reflectively's required to meet a desired enhancement factor. For example, if we assume for simplicity that the mirrors are identical, then to enhance the input power by a factor of 100, a reflectivity coefficient of $r^2 \sim 0.9988$ (=99.88%) is required per mirror. Note that, in reality, there are additional cavity losses due to: absorption in the mirrors; diffraction due to the finite mirror sizes; scattering from mirror surface irregularities; alignment imperfections etc.

ABCD Matrices

Consider a 4 mirror cavity with the same mirror radii of curvature, R_i=R_c, or equivalently focal length, $f = R_c/2$ (for spherical mirrors), and with equal mirror spacing, d. The cavity is symmetric and several waists will be created: at the central point of the cavity and in-between mirrors. This is shown schematically in figure 2.17. To find the value of the waists, standard ray tracing optics can be used to visualise the path the beams take through the

cavity. However, a simpler method can be used when working in the paraxial approximation, as we have been doing. This method, called ABCD matrix analysis assigns a 2x2 matrix to each optical component and combines them, with basic matrix multiplication, to find the overall 'ray transfer matrix' (RTM) of the optical system [110]. This method can describe the propagation of an incoming Gaussian beam through the entire cavity and allows calculation of the beam waist and cavity stability as will be shown subsequently.

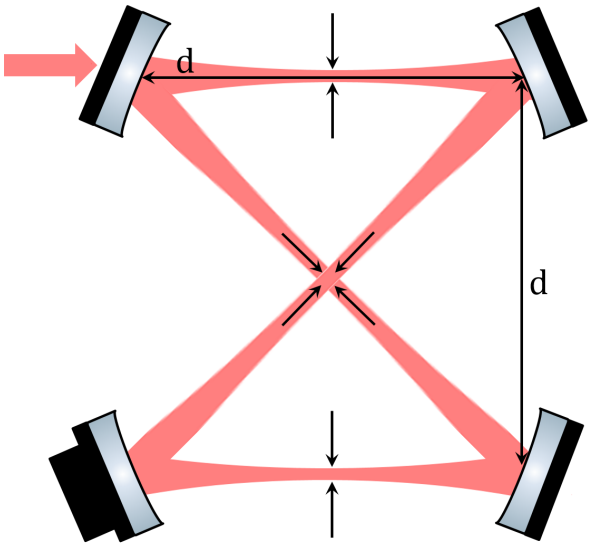

Figure 2.17: Highlights the beam waists in a 4 all-curved-mirror cavity.

First, we describe a single paraxial ray with a two element column vector consisting of the height of the ray above the axis, y, and the slope of the ray, y': $\begin{pmatrix} y \\ y' \end{pmatrix}$. When the ray vector passes through an optical component, it is subject to a linear transformation depicted by an ABCD matrix which causes changes in the height and slope of the ray according to:

$$\begin{pmatrix} y_2 \\ y_2' \end{pmatrix} = \begin{pmatrix} A & B \\ C & D \end{pmatrix} \begin{pmatrix} y_1 \\ y_1' \end{pmatrix}. \tag{2.72}$$

where the subscripts $_{1,2}$ represent the ray before and after transformation respec-

tively. Below are described the ABCD matrices for the simple transformations of free space propagation, propagation through a slab, thin lens, and mirror.

Free space propagation: For propagation over a distance d, use the equation for a straight line to find the ray matrix:

$$y_2' = y_1', \quad y_2 = y_1 + y_1' d \quad \longrightarrow \quad \begin{pmatrix} A & B \\ C & D \end{pmatrix} = \begin{pmatrix} 1 & d \\ 0 & 1 \end{pmatrix}. \tag{2.73}$$

Propagation through a slab of thickness d: From Snell's law in the paraxial regime [107] and assuming the slop does not change (for parallel exit and entry faces):

$$y_2' = y_1', \quad y_2 = y_1 + y_1' \frac{d}{n} \quad \longrightarrow \quad \begin{pmatrix} A & B \\ C & D \end{pmatrix} = \begin{pmatrix} 1 & d/n \\ 0 & 1 \end{pmatrix} \tag{2.74}$$

where n is the refractive index of the medium.

Thin lens: The height is unchanged and the slope conversion can be found using the lens formula [109]:

$$y_2 = y_1, \quad y_2' = y_1' - \frac{y_1}{f}, \quad \longrightarrow \quad \begin{pmatrix} A & B \\ C & D \end{pmatrix} = \begin{pmatrix} 1 & 0 \\ -1/f & 1 \end{pmatrix}. \tag{2.75}$$

Thin spherical mirror: The mirror can be modelled as a thin lens with $f = R_c/2$:

$$y_2 = y_1, \quad y_2' = y_1' - \frac{y_1}{f}, \quad \longrightarrow \quad \begin{pmatrix} A & B \\ C & D \end{pmatrix} = \begin{pmatrix} 1 & 0 \\ -2/R_c & 1 \end{pmatrix}. \tag{2.76}$$

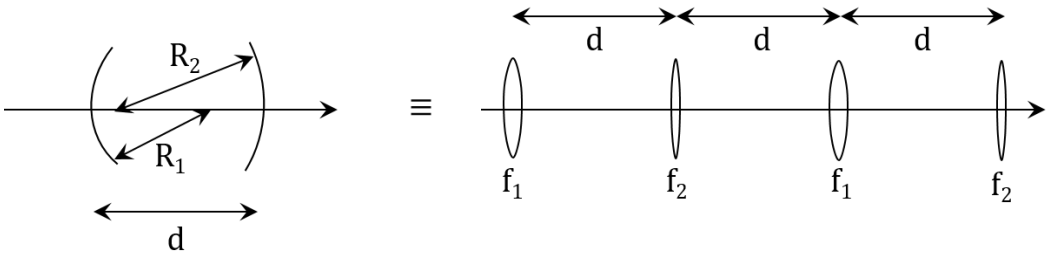

Figure 2.18: A 2 mirror cavity is modelled as a series of lenses where the radii of curvature of mirrors 1 and 2 are related to the focal length of the lenses by $R_1 = 2f_1$ and $R_2 = 2f_2$ respectively.

For our mirror system, light reflecting around the cavity will experience a periodic focusing action. This is equivalent to a period sequence of lenses [111] as demonstrated in figure 2.18. The fundamental transverse mode of a cavity is a Gaussian beam (as discussed in section 2.4.6) which is, as previously explained, described completely by a complex beam parameter, $q(z)$. This beam can be propagated through an optical system using the ray transfer matrix via:

$$\begin{pmatrix} q_2 \\ 1 \end{pmatrix} = \begin{pmatrix} A & B \\ C & D \end{pmatrix} \begin{pmatrix} q_1 \\ 1 \end{pmatrix} \tag{2.77}$$

so that the ABCD law is obtained:

$$q_2 = \frac{Aq_1 + B}{Cq_1 + D}. \tag{2.78}$$

This rule is valid for composite systems and allows us to quickly determine the q-transformation for a Gaussian beam in the presence of an optical system. For our optical cavity, light propagates in a closed path and therefore q must replicate itself after one round trip i.e. $q_2 = q_1 = q$. Therefore, the above ABCD rule becomes:

$$q = \frac{Aq + B}{Cq + D}. \tag{2.79}$$

The subsequent quadratic equation can be solved with the solutions:

$$\frac{1}{q} = \frac{D-A}{2B} \pm \frac{1}{2B}\sqrt{(A-D)^2 + 4BC}. \tag{2.80}$$

Since the ABCD elements are real, the first term in equation 2.80 is related to the real part of $1/q$ and the second term must be imaginary and is related to the imaginary part. Therefore, by comparing this solution to equation 2.65, the wavefront and waist radii can be found to be:

$$R = \frac{2B}{D-A} \tag{2.81}$$

$$\text{and} \quad w = \sqrt{\frac{2\lambda|B|}{n\pi\sqrt{4-(A+D)^2}}} \tag{2.82}$$

respectively. The values obtained using these equations are valid only at the particular chosen reference point where the round trip is (arbitrarily) chosen to begin and end. Values at other points can then be found by using the transformation equations 2.68 and 2.69.

The elements of the ABCD matrix are defined only by parameters of optical components (radius of curvature, focal lengths, distances etc.) and are therefore real. Hence, in order to obtain a real value for the beam waist (as is physically required), equation 2.82 generates the following criterion:

$$4-(A+D)^2 \geqslant 0 \longrightarrow |A+D| \leqslant 2. \tag{2.83}$$

If this 'stability criterion' is violated then it is impossible for the field to replicate itself after a single round trip and hence the cavity will be unstable.

The final solutions given in this section can be reverse engineered so that for a particular wavelength of light and desired beam waist, the required cavity

mirror radii of curvature and distances between mirrors can be calculated. This was the approach used to design the cavity in section 3.3.3

2.4.4 Linear and Ring Cavities

There are two types of optical cavity: linear and ring. A linear cavity is formed of 2 end mirrors (potentially with additional intermediate mirrors) and the input light has to reflect back upon itself to get back to the start. The output beam overlaps with the input beam and, assuming the light is continuously circulating, it results in a standing wave pattern in intensity. Whereas a ring cavity, formed by > 2 mirrors, has no end mirrors and the light gets back to its starting point without reflecting back upon itself. This is demonstrated in figure 2.19. In this case, a single input can be used to create a single beam circulating in one direction only around the cavity (travelling wave) or two inputs can be used to allow light to travel independently in both directions around the cavity. If the two inputs are identical and opposing, then a standing wave can be formed in a ring cavity.

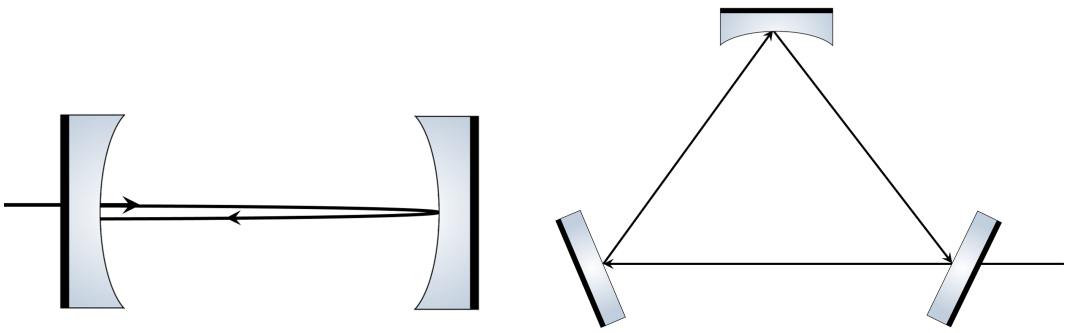

(a) Linear 2 Mirror Cavity **(b)** Ring 3 Mirror Cavity

Figure 2.19: Examples of the two main cavity types: (a) a linear cavity where a standing wave is always formed; and (b) a ring cavity with a single input.

2.4.5 Astigmatism

For ring cavities, the beams will not hit the mirrors at normal incidence i.e. the light will reflect off at some angle to the normal, as can be observed in figure 2.19 (b). If the mirrors are curved, this causes two different focal lengths and, in turn, two different mode waists in the tangential (horizontal) and sagittal (orthogonal) planes. This is entitled cavity astigmatism.

If θ is the angle (from the normal) at which the beam is hitting the mirror then the two focal lengths are given by:

$$f_t = \frac{R_c \cos(\theta)}{2} \tag{2.84}$$

and

$$f_s = \frac{R_c}{2\cos(\theta)} \tag{2.85}$$

where f_t and f_s are the tangential and sagittal focal lengths respectively and R is the radius of curvature of the mirror.

For an astigmatic cavity, the elliptical optical dipole trap equations 2.40 - 2.46 must be used instead of the circular ones (2.35 - 2.39) because the different cavity waists will lead to a non-circular trapping geometry in the x-y plane.

2.4.6 Hermite-Gaussian Modes

It was previously mentioned that cavities possess longitudinal modes which occur along the axis of the cavity (along the direction of travel of the wave). However, they also have transverse modes which are perpendicular to the axis due to boundary conditions and interference. Whereas the longitudinal modes differ only in frequency, the transverse modes differ in both frequency and shape. The most stable shapes (field distributions) are the ones that stay the

same after many cycles around the cavity: these are the modes.

Each mode allowed in an optical cavity can be described by a linear combination of a set of functions, each of which satisfies the paraxial wave equation [112]. The solution is a product of Hermite and Gaussian functions, hence they are referred to as Hermite-Gaussian modes. These modes can also be referred to as transverse electromagnetic (TEM) modes because neither the electric nor magnetic field are in the direction of propagation. Specifically the notation $\mathrm{TEM}_{n,m}$ is used where n and m are integers that describe the order of the Hermite polynomials in question. Figure 2.20 shows the cross-sectional profile of the $\mathrm{TEM}_{n,m}$ modes with the n nodes in the horizontal direction and the m modes in the vertical direction. Note that the number of zeros in a mode pattern is equal to the corresponding mode number.

The simplest, or fundamental, mode is the $\mathrm{TEM}_{0,0}$ mode which describes a Gaussian beam. The mathematical form of this mode was previously described in section 2.4.2 and this is the mode that will be used in this experiment. Note that the Hermite-Gaussian solutions contain a phase term, referred to as the 'Gouy phase shift', which causes a mode dependent phase shift per round-trip of the cavity. This results in each mode having its own set of longitudinal modes (resonant frequencies). For the simple Gaussian beam case, this was seen in the phase term, $P(z)$, in equation 2.64.

2.4.7 Impedance Matching

Maximal light is coupled into an optical cavity when the round trip power loss is equal to the transmission of the input mirror [109]. This is referred to as impedance matching.

As before, we use: r_1 as the reflectivity of the input mirror; r_2, r_3, r_4, etc. as the reflectivities of the subsequent mirrors; and r_m as the fraction of the

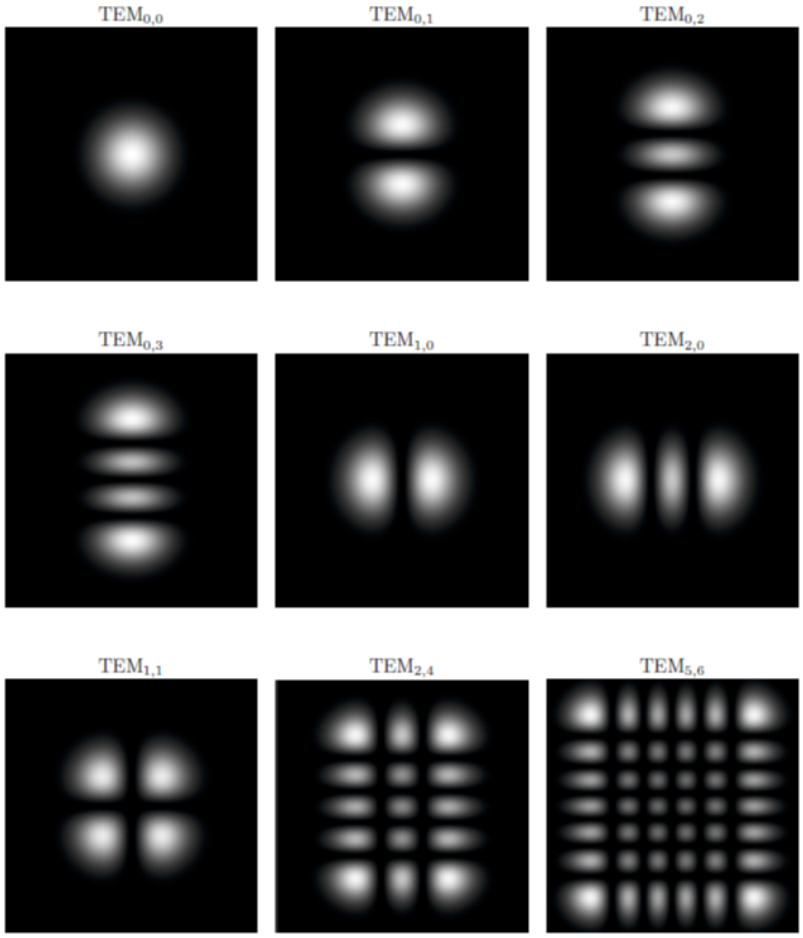

Figure 2.20: Cross-sectional intensity profile of the $\text{TEM}_{n,m}$ modes of an optical resonator [112].

cavity power remaining after one round trip (ignoring the transmission through the input mirror). Then in the impedance matched case $r_1 = r_m$ and excluding absorption and scattering losses, $r_1 = r_2 r_3 r_4 ...$

Compared to the equal reflectivities cavity ($r_1 = r_2 = r_3 = r_4 = ...$), impedance matching can achieve the same total circulating power but with a significantly reduced finesse; making the cavity building and stability more manageable.

However, the impedance matched case is not the one in which the most power enhancement is achieved. To get more power, an 'over-coupled' cavity can be used where $r_1 < r_2 r_3 r_4 ...$ In this case the finesse is increased compared

to the impedance matched case however it is still lower than the original equal reflectivity scenario and more circulating power is achieved. These principles are used to determine the exact reflectivity required for each mirror in an optical cavity (see table 3.2 in the cavity design chapter). Note that the equal reflectivity case is an 'under-coupled' cavity and in this case: $r_1 > r_2 r_3 r_4 ...$

2.4.8 The Optical Lattice: Standing Waves

Until now, we have only imagined a travelling wave cavity where light circulates the cavity in one direction only. However, in this experiment a standing wave cavity will also be used where equivalent beams circulate the cavity in opposite directions to form a standing wave. This is always the case for a 2 mirror cavity where the light bounces back upon itself but a standing wave can also be created in a 3 or 4 etc. mirror cavity by inputting equal beams into two different mirrors or 'ports'.

2.4.9 Atoms in Cavities

Note that when atoms are present inside an optical resonator, they can absorb photons from, and emit them back into, the cavity mode. Hence, the atom and cavity are coupled and they can be described by the well-known Jaynes-Cummings model [113]. However, in this experiment, the cavity light is far-detuned from the atomic resonance and hence, the coupling effect is negligible.

CHAPTER 3

CAVITY DESIGN

This chapter starts by describing the optical cavity's design, which is determined by theory outlined in the previous chapter as well as the vacuum system of the experiment which is discussed in chapter 4. Then, how this cavity might be experimentally built is discussed, including the method of fixing the cavity mirrors in place and suggested alignment procedure.

3.1 Main Design Criteria

The starting criteria for the cavity design is that it must create optimal conditions for atom capture from the magneto-optical trap (MOT) to the optical dipole trap (ODT), where evaporative cooling is performed. The former is relatively 'hot' and 'large' and this creates two design criteria for effective transfer to the latter:

1. The optical dipole trap must have a sufficient trap depth to capture a large proportion of the $\sim$ Maxwell-Boltzmann temperature distributed MOT atoms.
2. The optical dipole trap must be large enough to spatially capture a significant proportion of the MOT atoms.

The pros and cons of these conditions will be discussed in detail before the rest of the chapter explains how the cavity was designed to meet them.

3.1.1 Criteria 1: Trap Depth

To quantify the depth required for optical dipole trapping, one must consider the temperature of the initial MOT atoms. The atoms have a $\sim$ Maxwell-Boltzmann temperature distribution but with the long shallow tail at the upper end of the temperature scale truncated by the maximum velocity atom that can be captured in the 3D MOT (see section 2.2.1). As explained in section 2.2.2, during optical dipole trapping hotter atoms will rise up higher in the trap and therefore require higher 'trap walls' to be captured. Hence, the initial trap depth should be $\gtrsim$ the average atom temperature in the MOT to allow a significant fraction of the atoms to be captured. Typical average MOT temperatures for Rb-87 are on the order of 100 µK. However $\sim$ 5 µK can be reached by briefly turning off the MOT magnetic field and reducing the MOT beam intensity, and increasing its detuning, after loading (this is discussed in 2.3).

Equation 2.15 states that the trap depth is proportional to the beam intensity and hence, to achieve a trap depth of 100 µK requires a high circulating cavity power of 77 W (assuming 150 µm beams - see the following discussion on Trap Volume). Space compatible lasers with this power output are not commercially available and if they were, the input power required would be impractical for a space experiment where low 'SWaP' is essential, as discussed in 1.2.2. Hence, a high cavity mirror reflectivity is used to amplify an initially lower power laser to the required magnitude. For example, a typical input beam of 100 mW would have to be amplified 770 times to reach the required trap depth.

3.1.2 Criteria 2: Trap Volume

The second consideration is that the initial ODT must be large enough to spatially capture a significant number of atoms from the relatively 'large' MOT. From previous experiments in the group, a 1σ MOT size of < 1.4 mm is expected (where the MOT atoms follow a Gaussian distribution so $> 99\%$ of the atoms are contained in $6\sigma < 8.5$ mm [114, 115]). In the longitudinal z direction (axial to the cavity beams), the ODT can trap atoms contained within the 'Rayleigh length', $\pm z_R$, (see 2.2.2) which is calculated to be larger than the 3σ MOT length (~ 45 mm compared to 4.25 mm). Therefore, in the z direction, the ODT should be able to capture atoms from the entire MOT length, as demonstrated in figure 3.1.

However, figure 3.1 also shows that in the tangential x and y directions (radial/transverse to the cavity beams), the ODT is limited by the cavity beam size. To make the cavity beams $\gtrsim$ the MOT size is impractical because larger cavity beams are less stable and, as explained in the previous section, larger beams require a higher power to achieve sufficient trapping. Hence the cavity beams were chosen to be as large as possible whilst still being able to produce the required trapping depth of 100 µK. With an input power of 100 mW, the largest allowable cavity beam waist was then calculated to be $\sim$150 µm = 0.15 mm using equations outlined in the theory section. The cavity was hence designed to create beams with approximately this waist as discussed in section 3.3. To ensure as many atoms as possible are contained within these cavity beams, the MOT atoms can be compressed before loading into the ODT as described in 2.3. From literature [84, 86, 116–118], the MOT atom clouds can be compressed several times with these methods. Furthermore, this problem is slightly reduced in the vertical y axis because the MOT cloud is 'flattened'

in this direction. This is due to the MOT being created via a single Gaussian beam incident on reflective prisms, rather than 6 individual MOT beams (see section 2.2.1). Hence, the beam profiles of our reflected beams are not Gaussian (instead they are 'cut out' of the initial beam). Therefore, the expected 1.4 mm MOT size applies to the z and x directions but in the y direction, the atoms will be confined to $\sim$ 0.9 mm (experimentally the z and x directions are typically found to be 1.5 $\times$ the y direction). This 'flattened' MOT is shown schematically in figure 3.1 (b) and experimentally in figure 3.2.

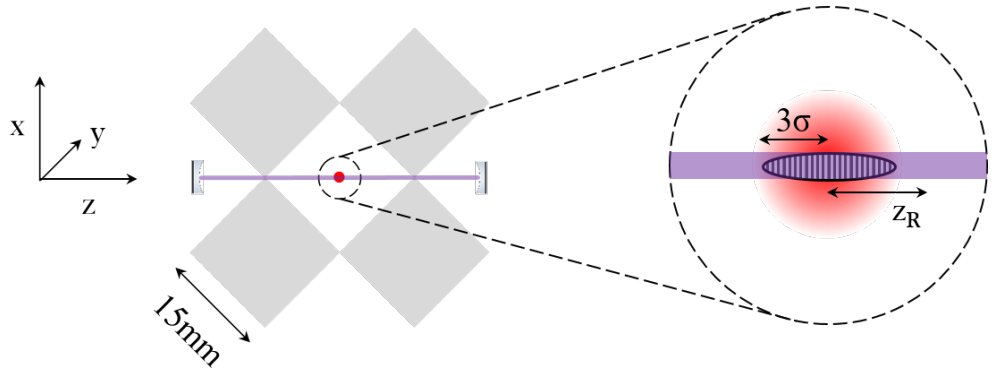

(a) Top down view

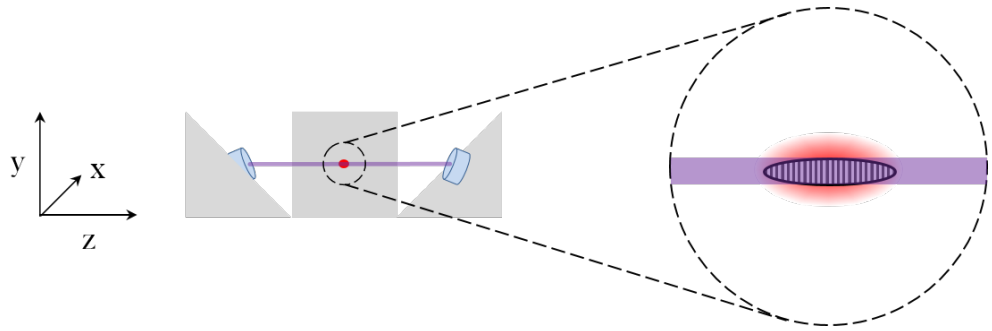

(b) Side view

Figure 3.1: Prism and cavity mirror arrangement (left) illustrating the approximate magneto-optical trap (MOT) region that is captured by the optical-dipole trap (ODT) (right). Prisms, MOT, cavity mirrors, and cavity beam are shown in grey, red, blue, and purple respectively. The ODT trapping region is superimposed on the MOT via the dashed region. The 3σ distance contains $> 99\%$ of the MOT atoms whereas the Rayleigh distance, z_R is the defining distance for the ODT in the z axis. The divergence of the cavity beam is not shown.

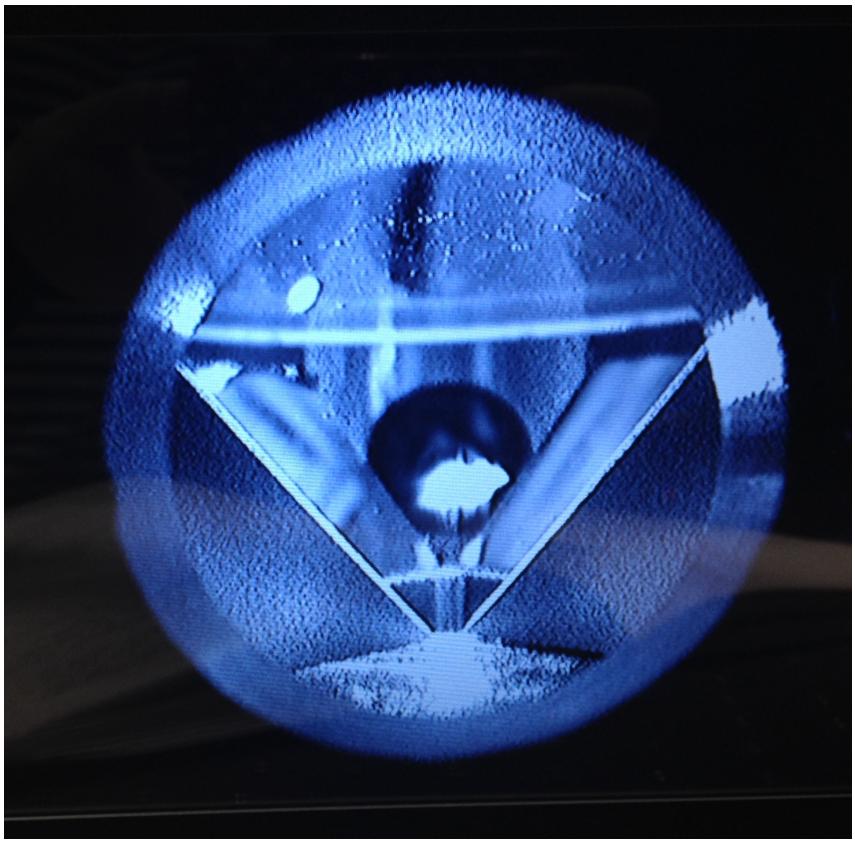

Figure 3.2: Prism-based magneto-optical trap (MOT) obtained experimentally by the author outside of this project [119].

3.2 Cavity in Vacuum

The aforementioned high ODT beam enhancement factor of ~ 770 requires the cavity to be placed in vacuum conditions because particles and dust in an open air environment would scatter the beams and coat the cavity mirrors, destroying the high reflectively required. In addition, the vacuum system windows purchased have losses of $\lesssim 0.25\%$ [120] which for a 2 mirror cavity causes up to 1% loss per round trip, hindering the power enhancement. An advantage of housing the cavity inside the vacuum is the potential for a compact system. This means a smaller cavity length which translates to a higher curvature of mirror to get the required beam divergence for a 150 µm

trap.

A disadvantage is that the cavity is not easily adjustable and will have to be aligned and mounted accurately outside the vacuum system in a 'clean' environment before being transferred with minimal movement. Piezo actuators can be used to make small alignment adjustments once inside. However the piezos themselves, as well as the glue required to fix them, will be detrimental on the vacuum quality. Therefore, a rigid and precise mounting structure was designed and custom built as is described in chapter 4.1.1.

3.3 Number and Radius of Curvature of Mirrors

To determine the number of cavity mirrors required, we first consider the different types of cavities.

3.3.1 Linear vs Ring Cavity

As previously described in section 2.4.4, there are two types of optical cavity: linear and ring. The simplest optical resonator is a linear resonator created by 2 concave reflecting mirrors which results in a standing wave in intensity. The theoretical description of ODTs (2.2.2) explains that a standing wave ODT creates a one-dimensional lattice of atomic sub-ensembles with a size on the order of the wavelength of the light. These small trapping sites make this trap type not ideal for initial atom capture from the MOT. Hence, a ring cavity (with > 2 cavity mirrors) is required in this experiment to allow for a large atom transfer.

3.3.2 Ring Cavity Design Options

The four ring cavity design schematics considered are shown in figure 3.3. They consist of: a 3 mirror cavity with 2 flat mirrors and 1 curved; a 4 mirror cavity with 4 equally curved mirrors (sometimes referred to as an All-Curved-Mirror (ACM) cavity); a 4 mirror cavity with 2 flat and 2 curved mirrors where the waist between the curved mirrors is used for the ODT; and a 4 mirror cavity with 2 flat and 2 curved mirrors where the waist between the flat mirrors is used. These are labelled a-d respectively. A crossed beam cavity was not considered (4 mirrors where the cross of the beams is used for the ODT) because it would require the 4 cavity mirrors to be in the gaps in-between the 4 MOT prisms and therefore there would be no horizontal optical access to the atoms for e.g. imaging (assuming an octagonal vacuum chamber is used - see figure 4.3). Figure 3.4 shows how each of these cavity designs would fit around the prism MOT system.

3.3.3 Cavity Parameter Calculations

For each option a-d, the cavity parameters were calculated including the beam size, stability, and power enhancement required to achieve sufficient ODT depth.

A MATLAB programme was created to vary the mirror radii of curvature for the various designs and calculate the corresponding cavity beam waists and stability parameters. This was done using the ABCD matrix analysis method outlined in section 2.4. For each design, a custom code had to be created to represent the specific set of optical components used in that design. Table 3.1 gives the radii of curvature for each design that allowed for a cavity waist closest to the chosen 150 µm whilst simultaneously maintaining cavity stability. Note

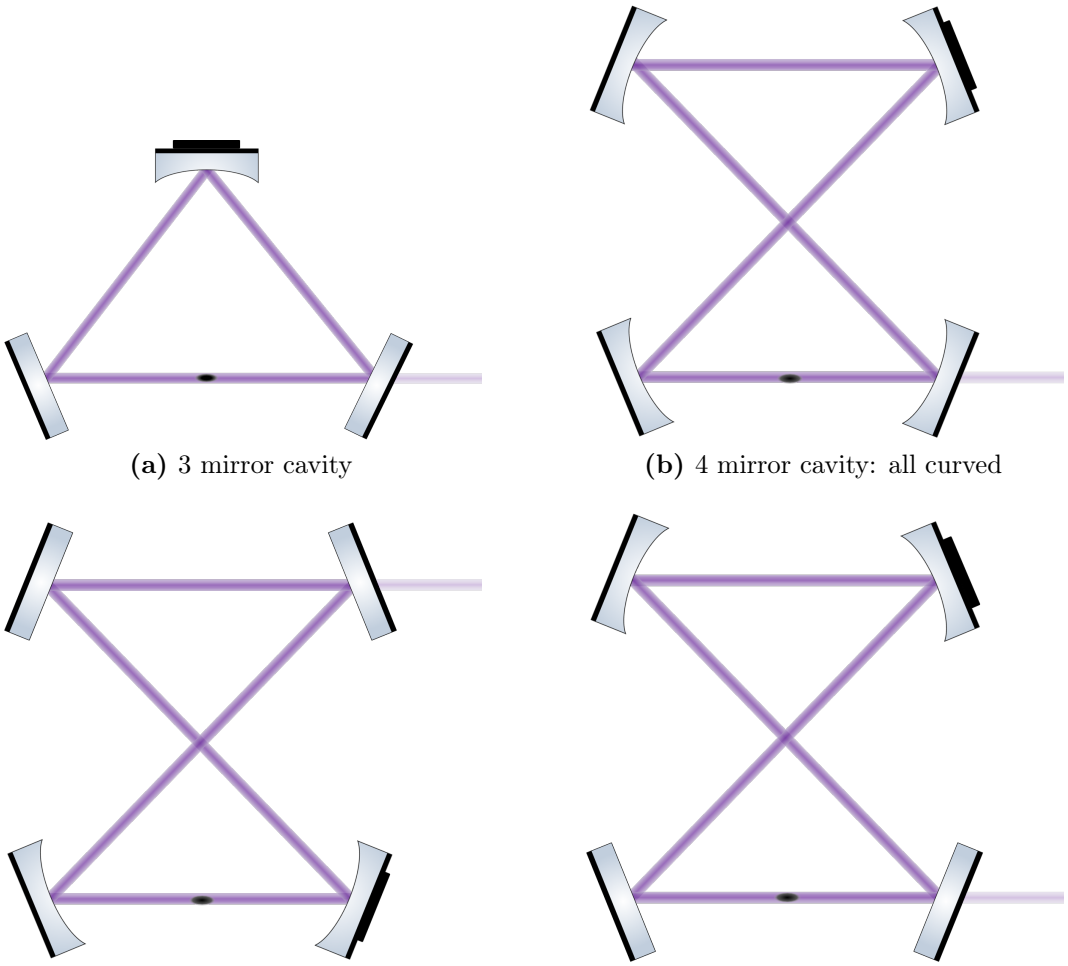

(a) 3 mirror cavity

(b) 4 mirror cavity: all curved

(c) 4 mirror cavity: 2 curved, 2 flat

(d) 4 mirror cavity: 2 flat, 2 curved

Figure 3.3: Ring cavity design schematics considered for the generation of an optical dipole trap (black) via the power enhancement of an incoming beam (purple).

that the beam waist and stability parameters are different in the tangential (horizontal) and sagittal (orthogonal) cavity directions due to the astigmatism caused by the cavity beams not hitting the mirrors at normal incidence which is described in section 2.4.2. Also, the mirror separation is set to 40 mm by the vacuum design because the cavity was designed to be mounted on a CF63 flange for easy removal and adjustments (see chapter 4).

Then, to determine which design provides the most appropriate ODT, the cavity parameters were converted to the corresponding cavity enhancement

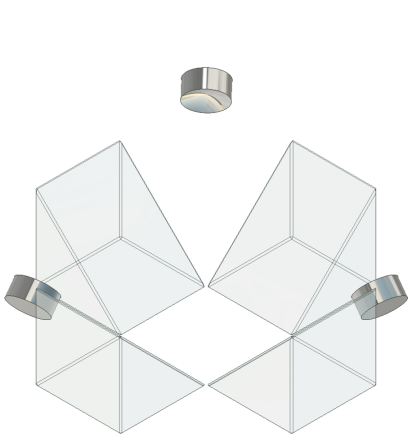

(a) 3 mirror cavity

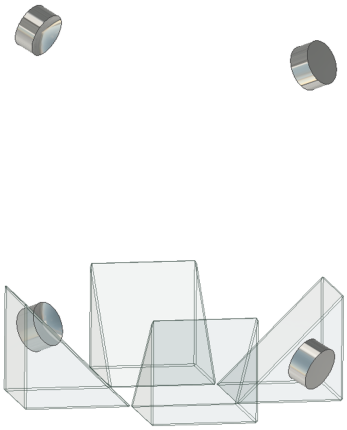

(b) 4 mirror cavity: all curved

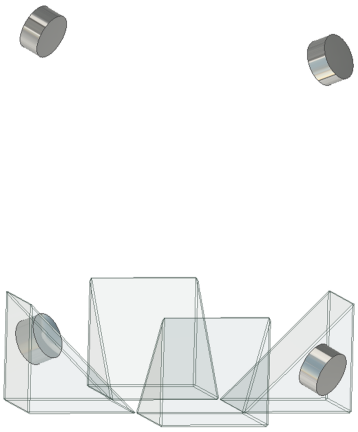

(c) 4 mirror cavity: 2 curved, 2 flat

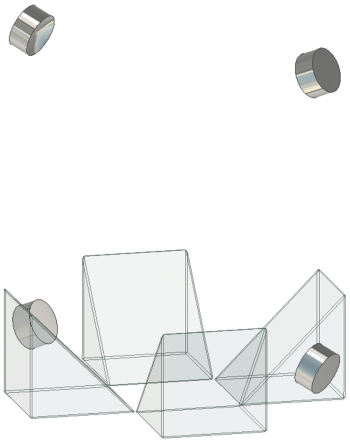

(d) 4 mirror cavity: 2 flat, 2 curved

Figure 3.4: Ring cavity options: rendered 3D CADs. The reflective prisms are transparent to highlight the cavity mirror arrangements.

factor (EF) and in turn, the circulating beam power and mirror reflectivity, required to achieve the chosen initial trap depth of 100 µK (assuming an input power of 100 mW). This was done using equations 2.41 and 2.70 and the results of which can been seen in table 3.1.

Table 3.1: Ring cavity design options considered for the generation of the optical dipole trap. Includes the calculated key cavity parameters including mirror radii of curvature, beam waist, stability, and enhancement factor and corresponding mirror reflectivities required to achieve an optical dipole trap depth of 100 µK with an single input beam of power = 100 mW.

Design	**Radii of curvature, R_c [mm]** [i]	**Beam waist in sagittal plane, w_{0s} [µm]** [ii]	**Beam waist in tangential plane, w_{0t} [µm]** [ii]	**Stability parameter in sagittal plane** [iii]	**Stability parameter in tangential plane** [iii]	**Enhancement factor, EF** [iv]	**Reflectivity, r^2** [v]
a	150	210	162	0.54	0.09	1165	0.99962
b	75	155	158	-0.04	0.43	828	0.99970
c	375	283	278	0.11	-0.01	2692	0.99991
d	200	168	141	-0.52	-0.73	810	0.99959

[i] The only radii of curvatures considered were those commonly available as substrates. For the designs with flat mirrors, the radii of curvatures given in the table are referring to the curved mirrors.
[ii] The sagittal and tangential directions refer to the axial and radial cavity beam directions respectively, as is described in section 2.4.2.
[iii] Although anywhere between -1 and +1 is technically considered 'stable', a stability parameter closer to 0 denotes a higher degree of stability and therefore puts less stringent requirements on the alignment accuracy.
[iv] EF = circulating power/input power.
[v] Assuming all mirrors have the same reflectivity i.e. impedance matching is not taken into account. Note that designs with a larger beam waist naturally result in a higher required mirror reflectivity to reach the same intensity and hence trap depth.

From the results in table 3.1, design b with 4 curved mirrors was chosen. This design generates the desired beam waist with achievable enhancement factor and stability parameters. Design c was the most stable however it would require highly reflective mirrors of > 0.9999 to achieve sufficient power enhancement. Design d has similar beam waists and enhancement factors as design b, but was less stable. A further advantage of a 4 mirror over a 3 mirror cavity is that it has lower astigmatism due to a smaller angle of light incidence on the mirrors.

Impedance Matching

Previously in table 3.1, the reflectivities of the 4 cavity mirrors were calculated assuming they were equal i.e. $r_1 = r_2 = r_3 = r_4$ where the subscripts 1-4 refer to the various cavity mirrors with 1 being the input mirror. However, in section 2.4.7, it is explained that maximal power is coupled into the cavity when the reflectivities are impedance matched ($r_1 = r_2 r_3 r_4$) and, moreover, maximum power is enhanced within the cavity when the cavity is 'overcoupled' compared to the impedance matched case i.e. $r_1 < r_2 r_3 r_4$. Table 3.2 compares the three cases: undercoupled ($r_1 > r_2 r_3 r_4$ e.g. $r_1 = r_2 = r_3 = r_4$); impedance matched; and overcoupled. This table shows that by 'impedance matching' the cavity mirrors, the same circulating power, and therefore optical dipole trap depth, can be obtained with lower reflectivities (compared to the equal reflectivity case). However, by overcoupling the cavity, a higher circulating power and trap depth can be obtained with only a slight increase in reflectivities or, equivalently, a lower input power can be used to obtain the same trap depth. Hence, this design was chosen. Mirrors matching this reflectivity (for 1560 nm at the required angle of 22.5°) were purchased from LAYERTEC, as well as an additional flat mirror for steering the cavity beam (described in 4.1.3). The

Table 3.2: Cavity mirror reflectivities and corresponding finesse and optical dipole trap depth for undercoupled, impedance matched, and overcoupled cavities. Assuming an input power of 100 mW for a 4 mirror cavity with 4 cm in-between mirror centres and equal radii of curvature of 75 mm.

Cavity coupling	$\mathbf{r_1^2}$ **[%]**	$\mathbf{r_{2,3,4}^2}$ **[%]**	**Finesse**	**Trap depth with input power of 100 mW [μK]**
Undercoupled	99.97	99.97	5235	100
Impedance Matched	99.88	99.96	2618	100
Overcoupled	99.88	99.97	2991	131

coatings are specified to be accurate to $< 0.02\%$ with the radii of curvature specified to 0.5%. The mirrors were also dual coated on the atomic resonance at 780 nm with a reflectance of 0.9985 at this wavelength. Note that because the price of the mirrors is determined by the cost of the coating run, rather than the relatively cheap fused silica substrate, the maximum number of mirrors that could be coated in one run were ordered. Hence, as an alternative option, mirrors for design d with 2 flat and 2 curved mirrors were also purchased.

3.3.4 Atoms Captured in Cavity

The number of atoms initially transferred into the cavity-based optical dipole trap can now be estimated by modelling the percentage of atoms that can be captured both spatially and thermally from the magneto-optical trap. By comparing to literature of other 2D MOT loaded 3D MOTs [88] and prism MOTs [92, 114, 115], $\sim 1{\times}10^8$ atoms are expected to be available after all pre-cooling stages have been complete with an average temperature of 1-5 μK (see 2.2.1). A Maxwell-Boltzmann distribution, with this average temperature (and truncated at the capture velocity (see 2.2.1) can then be modelled to calculate what percentage of these atoms could be captured in the ODT potential well.

The atoms in the M-B distribution have peak velocities of 0.013-0.03 m/s (note that the very 'hottest' atoms have velocities of ∼0.04-0.1 m/s but few atoms are at this 'tail' of the distribution). The initial ODT depth in the beam centre of $\sim$ 131 µK corresponds to maximum trapping velocity of 0.16 m/s and therefore, it should be sufficient for trapping. However, in the x and y directions, the ODT beams fall of in intensity as you move radially away from the z axis and this reduces the trap depth. Hence the spatially variant ODT trap depth was modelled and overlapped with the Gaussian atom distribution to calculate a capturable atom percentage.

The atom cloud should have a $\sim$ Gaussian distribution with a 1σ size of 1.4×0.9×1.4 mm in the x, y, and z directions respectively. Whereas the ODT can capture over ∼0.3×0.3×45 mm in the same axes (determined by the cavity waist size and Rayleigh length). By factoring in typical MOT cloud compression ratios (see 2.3) and accounting for the temperature considerations described above, it is calculated that 5% of the atoms should be captured in the ODT from the MOT. This gives a starting number of atoms in the ODT of $\sim 5\times10^6$ atoms. This number is comparable with other optical dipole trapping experiments from the past 20 years that managed to successfully reach Bose-Einstein condensates in 2-3 s of forced evaporation [103, 105]. At this time they were typically left with clouds of $10^4 - 10^5$ atoms with temperatures on the order of 1-100 nK which is sufficient for the proposed application of space-based atom interferometry (see 2.1). However, these experiments predominantly used a crossed-beam ODT (see 2.2.2) to optimise the evaporative cooling process whereas this experiment plans to use a novel hybrid single-beam - lattice system and so the final atom numbers achievable after evaporation in our system will be determined experimentally. Note that the comparative atom chip for space based atom interferometry technology produces atom clouds of 5×10^4 atoms

with $\leqslant$ 1 s evaporation or $5{\times}10^5$ atoms with $\sim$ 2 s evaporation [44].

3.3.5 Predicted Gravity Sensitivity

To ensure that this system design is suitable for the proposed application of Earth observation (EO), its expected sensitivity was calculated and compared to the existing classical sensors currently performing EO (described in section 1.2.1). This was done by modelling the atom interferometry (AI) process in MATLAB using theory outlined in chapter 2. Firstly, the range of Rabi frequencies experienced by the atoms over the area of cloud (due to the spatially variant Raman beam intensity) was summed and the corresponding AI fringe contrast was modelled. Then for a particular average atom temperature, and hence thermal expansion rate, the maximum interferometry time (or T-time) that ensured a specific fringe contrast was calculated. This T-time can then be converted to an expected gravimetry sensitivity, Δg, using equation 2.4 as long as the effective wavevector of the two-photon Raman transition, k_{eff}, and the number of atoms taking part in the measurement, N, are known. The former can be calculated to be:

$$k_{eff} = 2 \times \frac{2\pi}{\lambda} = 1.61 \times 10^7 \mathrm{m}^{-1} \tag{3.1}$$

for the transition in question. In terms of the latter, after evaporative cooling, typically between 1-10% of the initial atoms are retained, hence with a predicted starting number of $5{\times}10^6$ atoms in the ODT, between $5 \times 10^4 - 5 \times 10^5$ atoms should be available as a 'test mass' for the measurement. Table 3.3 shows the possible sensitivities achievable for these atoms numbers for a variety of T-times. Note that the exact minimum temperature, and hence maximum T-time, available in this system will be found experimentally.

Table 3.3: Predicted atom interferometer gravimeter precision for the system designed in this thesis. Refer to the text for further details.

Atom temp. [nK]	***T*-time [s]**	**Atom no., N [$\times 10^4$]**	**Sensitivity, $\Delta g/g$**	**Sensitivity, Δg [Gal]**
100	1	5	3×10^{-10}	3×10^{-8}
		50	9×10^{-11}	9×10^{-9}
50	2	5	7×10^{-11}	7×10^{-9}
		50	2×10^{-11}	2×10^{-9}
10	3	5	3×10^{-11}	3×10^{-9}
		50	1×10^{-11}	1×10^{-9}
1	10	5	3×10^{-12}	3×10^{-10}
		50	9×10^{-13}	9×10^{-11}

From table 3.3, this system has a predicted sensitivity of 10^{-8} - 10^{-11} Gal dependent on experimental parameters reached. This is several orders of magnitude better than the current GRACE-FO mission of $\sim 10^{-6}$ Gal and even the future improved sensitivity of the next mission which is predicted to achieve $\sim 10^{-7}$ Gal (refer to section 1.2.1). This validates this design as a potential successor of high-precision Earth observation.

Furthermore, improvements could be made to the single shot noise limited sensitivity by integrating over multiple measurements or by using techniques such as large momentum transfer (LMT) which increases the relative splitting of the 2 atomic wavepackets in atom interferometry [121]. Although, it should be noted that these calculations are for the shot noise AI sensitivity and do not account for additional losses of contrast due to e.g. any laser instabilities in intensity or frequency.

Note that although this system is designed for a space application, it must be tested on ground and hence the sensitivity capable in this environment was

also calculated. In this case, the interferometry time is limited by the available drop distance which is 150 mm (from the centre of optical dipole trap position to the atom interferometry measurement region). Using equations of motion and assuming the atoms are initially approximately stationary, this distance should be traversed by the atoms in 0.175 s due to the gravitational pull of the Earth on ground. Removing the interferometry pulse times and the initial waiting time required to allow the atoms to start falling ($\sim$ 10 ms), this gives a maximum interferometry time on ground of $\sim$ 80 ms. This equates to a gravity sensitivity of $4 \times 10^{-8} g$ ($\approx 4 \times 10^{-6}$ Gal) for 5×10^4 atoms or $1 \times 10^{-8} g$ ($\approx 1 \times 10^{-6}$ Gal) for 5×10^5 atoms.

These sensitivities are estimated assuming the full cycle of optical dipole trapping and evaporative cooling is performed (for testing purposes). However, as the T-time is orders of magnitude reduced compared to in a space environment, these additional cooling stages can be removed to increase the number of atoms and, in turn, the gravity sensitivity, without reducing the interferometry contrast. In this case, a sensitivity of $\Delta g = 6 \times 10^{-10} g$ ($\approx 6 \times 10^{-8}$ Gal) can be achieved.

3.4 Cavity Building Considerations

The high mirror reflectivities required for sufficient optical dipole trapping depth create logistical issues when building the optical cavity. Firstly, the mirrors must only be handled in a relatively clean environment and not exposed to environmental conditions where the mirrors could become coated in particles and dust. For this purpose, the optical cavity will be built in a Laminar Flow cabinet which carefully controls the flow of air to maintain a clean environment. Furthermore, the vacuum system will be cleaned, assembled, and pumped

down to a reasonable pressure before the cavity is inserted into the system. Secondly, a higher mirror reflectivity means the beam will circulate more times around the cavity and hence there is a low tolerance for cavity mirror alignment errors. However, in addition to the high cavity finesse, there are several building challenges that will make an accurate alignment difficult including inaccuracies or rough surfaces caused by the machining of the cavity mirror mount and movement of the mirrors caused by glue softening or shrinking during curing and baking. Due to these various challenges, the cavity is expected to provide the most significant building challenge of the experiment (as compared to the vacuum system, laser system, telescopes, and magnetic field coils). This section discusses the issues facing the optical cavity build including choosing a suitable glue and the alignment process.

3.4.1 Glue Requirements

Glue is required to fix the cavity mirrors into the v-grooves of the cavity mounts (see section 4.1.3) and to attach one cavity mirror to a ceramic piezo (used for mirror alignment) and, in turn, the piezo to the cavity mount. Therefore, the essential requirements of this glue are:

- It can bond glass, titanium, and ceramic strongly enough to withstand vibrations.
- It has low outgassing and therefore, is suitable for UHV.
- It has minimal movement when it cures i.e. minimal shrinkage and viscosity change.
- It can withstand temperatures of $\gtrsim 150°C$ without changing properties (for vacuum baking).
- It is not electrically conductive so the piezo is not shorted.

Furthermore, there are several additional desirable criteria including that

the glue can transmit 1560 and 780 nm light in case it 'creeps' to the back of the mirror where the light will be input/output and that the glue is space compatible for the future potential application of the project i.e. it can withstand the radiations and temperature changes of a space environment. Note that 'creep' is where the glue migrates across the substrate due to surface tension.

3.4.2 Glue Parameters

The relevant parameters to consider when selecting a glue are: the viscosity; the required cure temperature; and the required cure time. For each parameter, there are conflicting arguments for this experiment.

Viscosity

The glue must be of a suitable viscosity so that an amount can be picked up, for example using a needle tip, and it can be touched to a mirror-mount join and the surface tension of the glue will be sufficient to pull it into the gap. If it is too thick then it will not fill the gap and if it is too thin it could flow away. Furthermore, using a lower viscosity glue creates thinner layers and has less movement whilst curing, both of which are ideal to prevent mirror misalignment. However a higher viscosity glue has the advantage that it will have less 'creep' and therefore is less likely to coat the reflective mirror surface.

Cure Temperature & Time

When a glue cures, chemical cross-links form. For good mechanical strength and a strong bond, high cross-link densities are required. Note that when re-heated, a cured epoxy material does not melt but instead undergoes a slight softening or phase change. The midpoint of the temperature range over which an epoxy changes from a hard or 'glassy' state to a pliable or 'rubbery' state is defined as the glass transition temperature, T_g [122]. It depends on the type

of epoxy and the degree of cure but is also strongly dependent on the cure schedule with a higher curing temperature increasing T_g.

Typically, curing at a higher temperature results in more cross-linking and it will be faster so that there is less time for creeping. Furthermore, curing at a higher temperature raises the glass transition temperature. Therefore, vacuum baking can be performed at a higher temperature which is ideal for reducing outgassing (see section 4.1.6). Ideally, the glass transition temperature would be raised so that it is not the limiting factor to the vacuum bake. However, curing at a high temperature causes rapid shrinking of the glue which can result in alignment errors.

Using a lower temperature cure for a longer time creates a lower degree of shrinkage and also creates lower stress. This is because the structure is locked in more slowly. Whatever temperature the glue is cured at will be the zero stress point and so curing at a lower temperature will reduce the stress for the room temperature cavity operation. However, a glue cured for a lower temperature and longer time may not be able to withstand as high baking temperatures and the resin may migrate over this additional time. Furthermore, some adhesives will not cure (i.e. form cross-links) at low temperatures e.g. room temperature.

One compromise is to use a stepped or ramped cure where curing is begun at a lower temperature and then raised. This has been shown to produce lower stress than for a high temperature cure but higher cross-linking than a low temperature cure. For example, curing Epo-Tek's 301-2 Epoxy at 40 °C for 1 hour followed by 80 °C for 3 hours resulted in a similar performance to an all 80 °C cure but with lower stress [123].

Note that any heat sinks (e.g. large bodies of material) involved can absorb heat and create a longer required curing time. In addition, note that if the cure temperature is too high, a run-away reaction can occur where the glue

bubbles and expands. This is less likely to occur for smaller volumes of glue (or small volume to surface area ratios).

3.4.3 Glue Selection

Based on the above glue requirements and parameter considerations, 3 different options were chosen to be tested and these can be seen in table 3.4. All of these 2-part epoxies feature low outgassing [124], high optical transmission, are not electrically conductive, and bond the relevant materials of glass, titanium, and ceramic. However, they differ in their viscosity and curing parameters as well as their glass transition temperature.

Table 3.4: Specifications of the epoxies considered for cavity building [125].

Epoxy	**Minimal cure conditions**[i]	**Glass transition temperature**[ii]	**Viscosity at 23 °C [cPs]**[iii]	**Spectral transmission,%**
301-2	80°C - 3 hrs 23°C - 2 days	$>$ 80 °C	225-425	$\geqslant$99 at 780 nm $\geqslant$97 at 1560 nm
353ND	150°C - 1 min 80°C - 30 min	$>$ 120 °C	3000-5000	$\geqslant$98 at 800 nm $\geqslant$95 at 1560 nm
OM125	80°C - 1 hr 23°C - 24 hr	$>$ 90 °C	2400-5400	97 at 800 nm $\geqslant$96 at 1500 nm

[i] A temperature of 23 °C indicates a room temperature cure.
[ii] The glass transition temperatures reported are typically for a full cure i.e. 100% conversion of the material. It was typically measured using the minimum recommended cure conditions and hence, this experiment will attempt to increase these values.
[iii] For reference, water has a viscosity of 1 cPs. Viscosity measured at a specific RPM.

Epoxy 301-2 is low viscosity and can be cured at low temperature. This would allow the mirror(s) to be aligned at room temperature and left to start curing without moving. Then once partially cured, the structure could be moved to a hot oven to finish curing. This procedure aims to minimise glue shrinkage, mirror movement and cure time whilst maximising strength and ability to be baked at high temperatures. However, the low viscosity could

result in unwanted creep. An alternate option is epoxy 353ND which is a well used standard and must be cured at higher temperatures and has a medium viscosity. This epoxy should be able to withstand higher baking temperatures but it will have to be moved to an oven totally uncured which could have a negative effect on alignment. Finally, epoxy OM125 is chosen as a compromise between the two previous glues: it can cure at room temperature but also is a medium viscosity glue.

To determine which epoxy should be chosen for cavity building, several tests should be performed. Predominately, the strength of the bond produced between glass, titanium and ceramic should be tested as well as the optimum curing conditions to minimise mirror movement and maximise temperature resistance. It will be quantitatively investigated how the cure temperature affects the glass transition temperature of each epoxy to ensure that the glue chosen can withstand the vacuum system baking temperature without misalignment. The spectral properties should also be measured to ensure these have not been negatively effected by a high temperature cure (which may cause discolouring of the glues). All of the three epoxies have been purchased and testing them should be the priority when experimental work begins.

3.4.4 Suggested Gluing and Alignment Procedure

A cavity alignment procedure was developed based on the above discussion and literature which uses a method of curing the cavity mirrors one at a time at progressively lower temperatures [126]. This prevents the curing of the mirror in question from disturbing the alignment of the previously cured mirrors. The vacuum bake would then be performed at a lower temperature than these cures. By curing the mirrors one at a time, each one can be cured whilst it is lying flat so there is no torque acting on it due to gravity. Furthermore, any

small misalignments accumulated when a particular mirror is cured can be compensated for with the placement of the subsequent mirrors. The procedure should be preceded by cleaning the cavity mount in an ultrasonic bath and pre-baking the cavity mount and piezo to minimise outgassing (see section 4.1.6). Both procedures involve use translational stages (attached to the cavity mirrors via weakly glued metal posts/ appendages) to align the cavity mirrors into the mount using a laser and will take place inside a Laminar flow cabinet. The cavity mount will be held in place during alignment using a custom built structure. One of the cavity mirrors will be glued to the piezo and cured before the alignment procedure begins. The procedure is based on epoxy 301-2 or epoxy OM125 as it involves a degree of room temperature curing.

- Glue the first mirror in place and allow to cure at room temperature to minimise the mirror movement and set the zero-stress point. The duration of the cure will be determined by the epoxy testing stage.
- Transfer the cavity to an oven and complete curing using a ramped cure to a higher temperature, e.g. 80 up to 150 °C, to raise the glass transition temperature.
- After curing, check the alignment and re-align the subsequent cavity mirrors as necessary.
- Glue the second mirror in place and leave at room temperature for a suitable amount of time.
- Transfer to an oven to complete curing at a slightly lower temperature than the first e.g. 140 °C.
- Continue this process of mirror alignment and curing until all mirrors have been baked.
- Perform a test bake by placing the cavity in the oven at the baking temperature and check it can withstand the temperature without misalignment

(e.g. test the finesse before and after baking).

- If successful, insert the cavity mount into the vacuum system and bake, e.g. at 110 °C, for several weeks.

If the procedure outlined above cannot create a cavity with the required finesse then changes will be made to the procedure as appropriate. If the softening at high (baking) temperatures proves to be the limiting factor, then alternative epoxies could be tried, for example the 353ND epoxy. Furthermore, changes to the cavity mount design can be made to aid alignment, as will be discussed in section 4.1.3. As a final backstop, changes could be made to the cavity design itself if necessary, for example, the 4 curved mirror cavity can be changed to a 2 flat, 2 curved mirror cavity where the alignment of the flat mirrors is less critical. This cavity was simulated to have a similar beam waist and required enhancement factor as the 4 curved mirror cavity and parts for this alternate cavity have also been bought, as described in earlier in the chapter.

CHAPTER 4

SYSTEM DESIGN

This chapter describes the system design including: the vacuum system used to house the atoms and cavity; the coils used to generate the required magnetic fields; and the laser system and telescopes used to create the necessary optical beams.

4.1 Vacuum System

It is not possible to create the required cold atom clouds at atmospheric pressure due to collisions with background gas atoms which lead to heating. Hence the experiment must take place in an ultra-high vacuum (UHV) system. The vacuum flanges used are of the ConFlat (CF) variety which use knife-edges and soft metal gaskets to create extremely leak-tight seals. In Europe, the flange sizes are named by the prefix DN followed their inner diameter in mm. There are set standard sizes available.

To summarise from chapter 2, the vacuum system for this experiment requires three key regions: a 2D magneto-optical trap (MOT) region where a cold atomic loading beam is created; an ultra-cold atom preparation region where a 3D MOT is produced (using the 2D MOT atoms and reflective prisms for

light delivery) and further cooling is performed in an optical dipole trap (ODT) which is generated in an optical cavity; and finally an atom interferometry region where gravity measurements are undertaken. Figure 4.1 shows the vacuum system design, with the key components numbered as follows:

1. Rubidium dispenser attached to port of a DN40 4-way cross - inputs rubidium atoms into the vacuum system.
2. 2D MOT is formed in a 6-way DN40 cross, with 4 viewports being used to input the 2D MOT cooling beams.
3. The atomic 2D MOT beam generated is directed towards the 3D MOT region with a pushing beam input through a fifth viewport.
4. Graphite tube used to limit atomic conductance between the 2D MOT and 3D MOT chambers – housed in a DN16 tube.
5. 3D MOT chamber houses the reflective prisms and cavity required for ultra-cold atom generation – it has viewports to couple light into the cavity and for detection.
6. 3D MOT generation light is input from a large DN63 port above – 4 reflective prisms and a mirror then create the 6 counter-propagating beams required for a 3D MOT.
7. A DN63 6-way cross is used as the atom interferometry region (system would be upside down compared to figure for on ground gravity measurements so that, when released, the atoms fall into this region) - ports are used for measurement and detection.
8. Valves used for attachment of temporary pumps which reduce the pressure of the system from atmospheric and remove water and dirt.
9. An ion pump and getter is continuously used to maintain the ultra-high vacuum pressure.

Where possible, standard vacuum parts were used for cost, ease, and lead

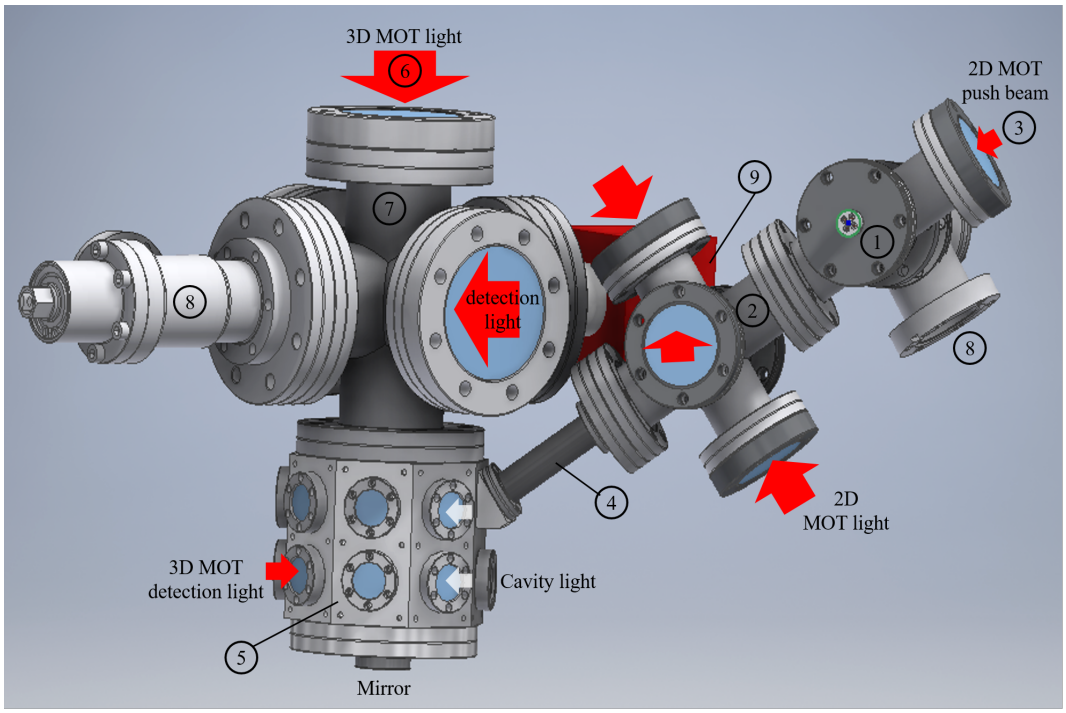

Figure 4.1: 3D CAD design of the vacuum system. (1) Rubidium dispenser (2) 2D MOT region (3) 2D MOT pushing beam (4) Conductance tube (5) 3D MOT chamber (6) 3D MOT light (7) Atom interferometry region (8) Valves (9) Ion pump and getter. See text for further details.

times. These parts are made from 316LN stainless steel which is a non-magnetic, strong, weldable, corrosion resistant grade of stainless steel. However, the novel design required the cavity and prism mounting structures and the 3D MOT chamber to be custom designed, using 3D CAD software, and built using an in-house workshop. These parts are made from titanium which is an ideal material for portable, ultra-high vacuum systems due to its low magnetism, low weight, and low outgassing properties. These custom parts will be described in further detail subsequently.

4.1.1 3D MOT Chamber

Figure 4.2 shows the main chamber where the required test atoms will be prepared. It is a custom designed, two-layered octagon. Two-layers are required

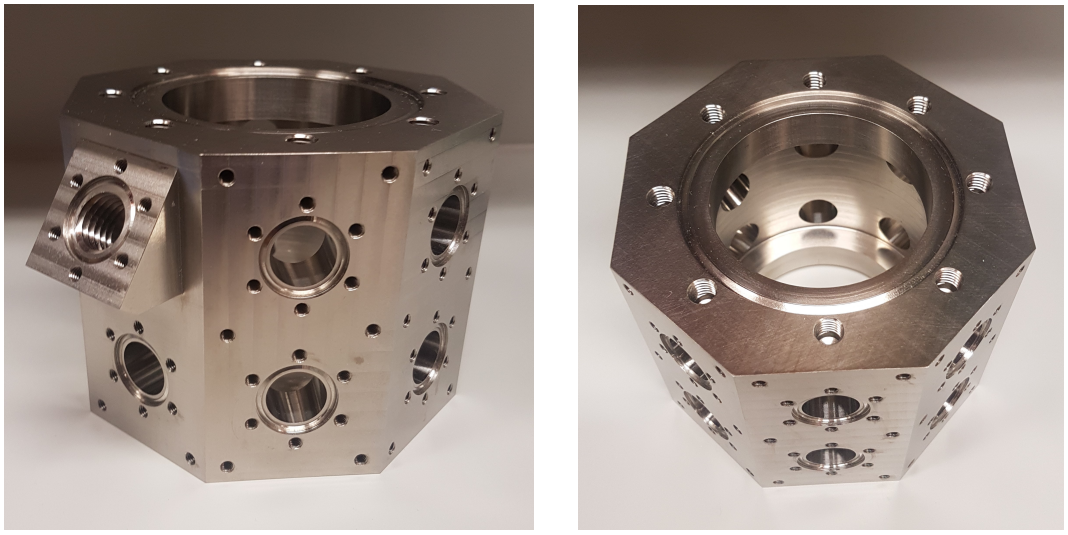

(a) Side View **(b)** Top View

Figure 4.2: Custom designed and built vacuum chamber used to house the 3D MOT and cavity required to generate ultra-cold atoms.

for optical and electrical access to the vertically mounted, four mirror cavity. Standard sized ports were incorporated for compatibility with off the shelf vacuum components. The top and bottom ports are DN63 flanges and the radial ports are DN16. The 16 available radial ports are used as follows:

- 1 attachment for atom input.
- 3 viewports for cavity light input and output (1560 nm).
- 1 electrical feed-through for the piezo used to adjust cavity mirror positions.
- 6 viewports for atom measurement and detection, 2 in the bottom plane and 4 in the top (780 nm).
- 4 ports are blocked by the MOT prisms.
- The remainder are uncoated viewports for viewing inside the vacuum.

This assignment of ports can be seen schematically in figure 4.3. The DN16 viewports, purchased from Torr Scientific, offer $\gtrsim 99\%$ transmission.

There are additional tapped holes for chamber mounting or attachment of external components. Note that one DN16 port is configured at an angle to

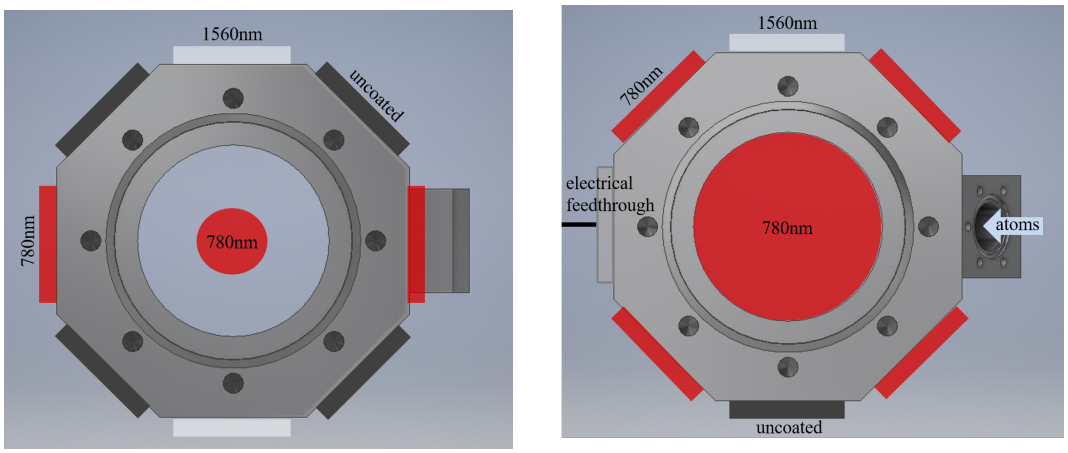

(a) From Bottom - Layer 1 **(b)** From Top - Layer 2

Figure 4.3: Assigned use of the 16 available ports of the 3D MOT chamber. Red, white, and black represent 780 nm coated, 1560 nm coated, and uncoated viewports respectively. The ports for atom input and electrical feed-through for piezo controlled cavity mirror adjustments are also labelled.

the chamber for 2D MOT mounting which is described in section 4.1.4.

4.1.2 Prism & Cavity-Mounting Flange

For the 3D MOT generation, 15 mm prisms (Thorlabs PS915H-B) were selected which have a reflectivity of $> 99.75\%$ at 780 nm. These prisms, and the cavity, will be mounted onto a custom built DN63-DN16 reducer flange as seen in figure 4.4. This flange has an in-built mounting structure for the 3D MOT prisms with notches to aid alignment. There is also a central hole to allow the 3D MOT light (input from above) to leave the chamber through a DN16 viewport where it is retro-reflected by a mirror to create a required counter-propagating 3D MOT beam (see section 2.2.1 for a description of the 3D MOT light generation in a prism system).

The mount also has tapped holes for attaching the cavity mounting structure. This cavity mount can be seen in place in figure 4.5. The mounts are designed so that the optical dipole trap generated by the cavity should automatically

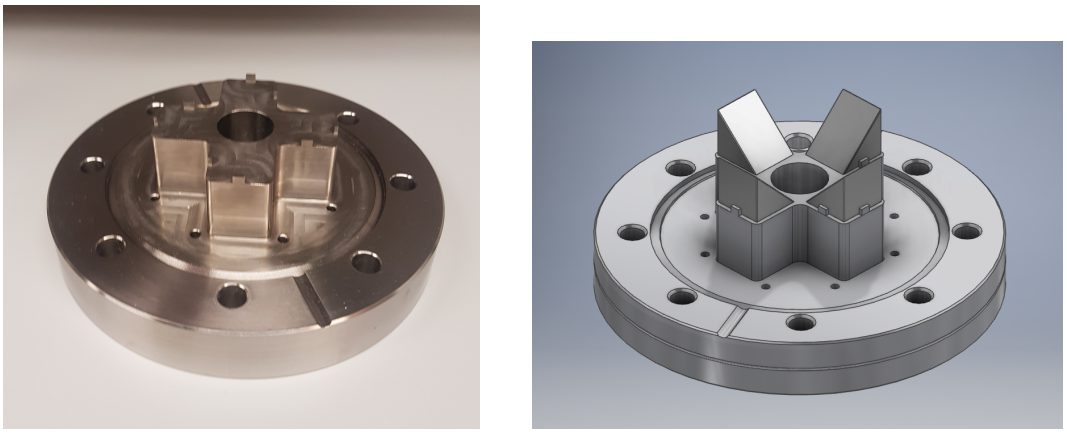

(a) Machined mount **(b)** CAD showing prism placement

Figure 4.4: Custom designed and built flange DN63-DN16 reducer flange used for mounting of the cold atom generating prisms (3D MOT).

overlap with the densest part of the 3D magneto-optical trap. Mounting the cavity on a removable structure on this flange allows for adjustments and cleaning to be made if necessary, or even for alternate cavity designs to be tested. Note that these images were made/taken before the addition of an extra rigid piece to the cavity mount (see section 4.1.3).

4.1.3 Cavity Mount

The cavity mounting structure can be seen independently in figure 4.6. It consists of a base with 2 vertical posts which are attached together using screws as shown in figure 4.6 (b)-(c). The base attaches the mount to the DN63 flange as described previously and the posts are used to house the cavity mirrors. To minimise post vibrations and movement, the base is made from a single, circular piece which is 10 mm thick and the posts are as large as possible whilst still fitting inside the clear aperture of the DN63 flange and without blocking the 3D MOT beams (this can be observed in the overhead view in figure 4.5 (b)). An additional rigid piece was also added to the design for this purpose as can be seen in figure 4.6 (d). This piece attaches the 2 posts, via screws,

(a) Side View **(b)** Overhead View

Figure 4.5: Cavity mounting structure placed onto prism mounting flange.

approximately half way up. The thickness of this piece is limited by the need to maintain optical access through the chamber viewports and it is semi-circular so as not to block the incoming 2D MOT atomic beam (see section 4.1.4 for description of the 2D MOT path).

The cavity mount was made out of 3 separate parts so that the faces of the posts could be extruded into to hold the cavity mirrors. This would not have been possible in the in-house workshop if the mounting structure was machined from only a single piece. The posts contain 4 extrusions (2 each) for housing the 4 cavity mirrors. These extrusions are placed so that the mirrors are at (approximately) the correct distances apart and angles to generate the optical cavity designed in chapter 3. The extrusions feature v-grooves which reduces the degrees of freedom for mirror placement as can be seen in figure 4.7 (a)-(b). The mirrors will be glued into place as discussed in chapter 3.4.

To input light into the cavity, the posts contain small holes for optical access

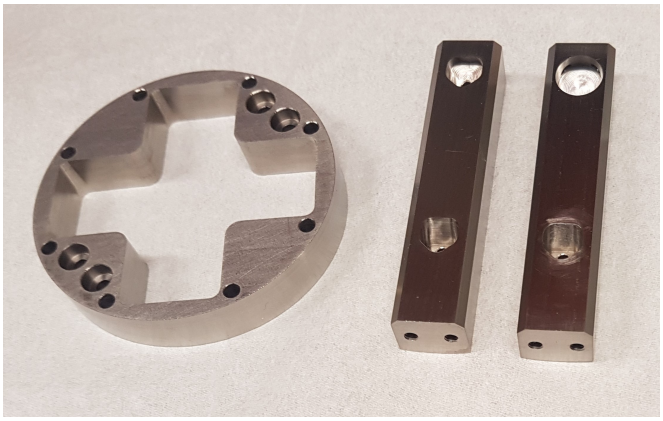

(a) Disassembled

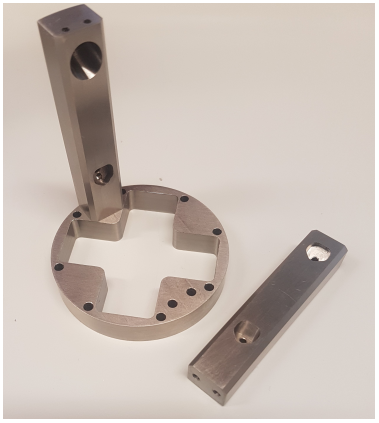

(b) Partially assembled

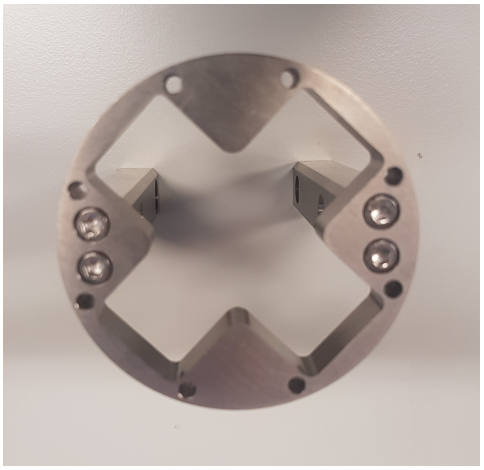

(c) Underneath

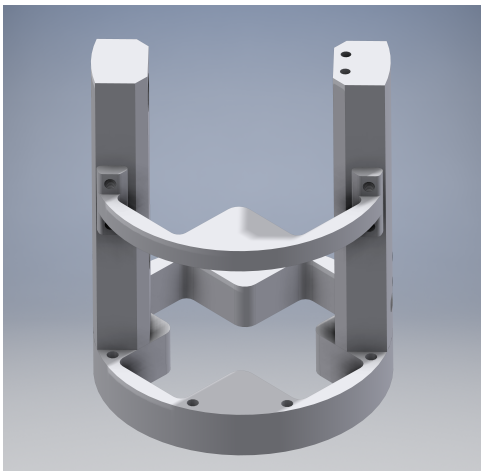

(d) Extra rigid piece

Figure 4.6: Optical cavity mirror mount made of a base and 2 posts (a). The posts attach to the base via screws (b)-(c). An additional rigid piece is attached via screws to minimise post movement (d).

to the back of the cavity mirrors. To generate a standing wave in the cavity, which is desired to create an optical dipole lattice trap (refer to section 2.2.2), the light has to be input into both cavity directions i.e. so that it circulates both ways around the cavity. Therefore, light has to be directed onto the back of the input mirror at 2 different angles. One of the beams is angled perpendicular to the mounting posts and chamber wall and hence this is easily input straight through the chamber viewport. However, the second cavity beam is at a 45° angle to the first. Therefore, a further hole is added to the mounting

post for an additional steering mirror, as shown in figure 4.7 (c). This mirror has the same specifications as the cavity mirrors except it is flat, in order to ease alignment. The steering mirror allows the second cavity beam to be input through the same viewport, parallel to the first, as shown in figure 4.7 (d). Furthermore, to align, lock and examine the cavity, an additional post hole is added for an output beam and the second layer of chamber viewports was aligned with this.

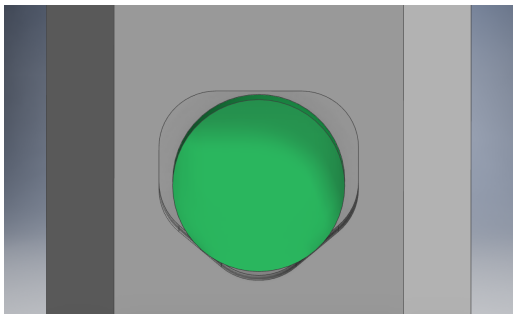

(a) V-groove mirror mounting

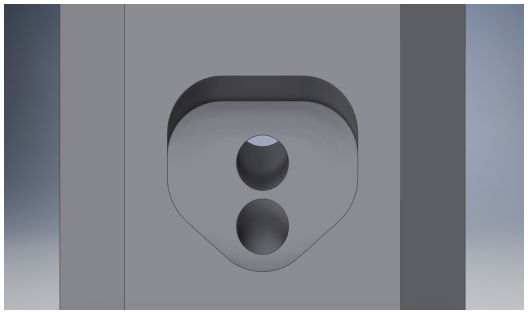

(b) Holes to input light

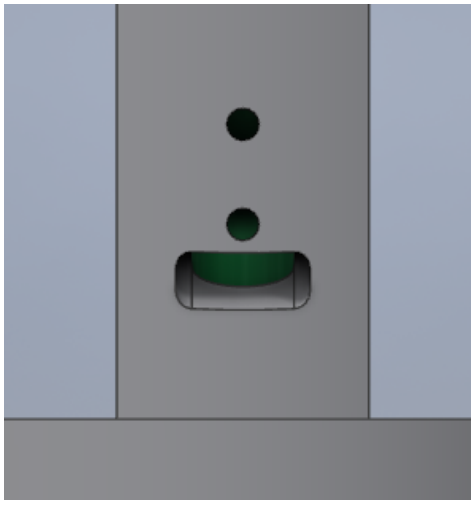

(c) Back of post

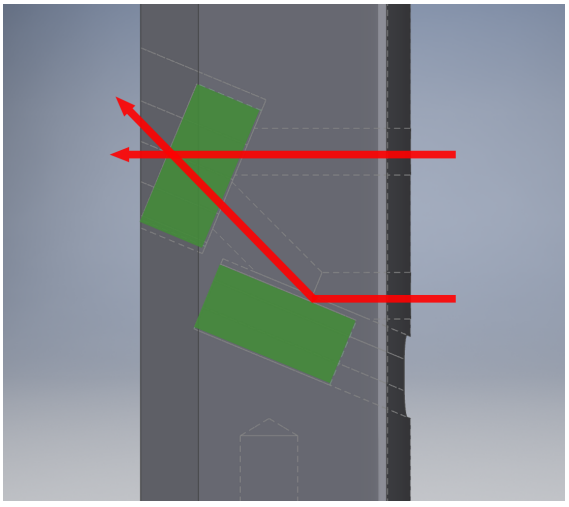

(d) Steering mirror

Figure 4.7: Illustrates the v-groove design used to mount cavity mirrors (a) and the holes in the mounting posts used to input light to the cavity (b)-(c). An additional steering mirror is used to input light into the second cavity direction (c)-(d). The mirrors are shown in green.

For fine control of the cavity length and alignment, a piezo actuator is

required. This will be glued to the back of one of the cavity mirrors and hence a 9.3 mm circular extrusion is used to fit this in and to allow for mirror movement. This is shown in figure 4.8. Two holes were also added into the post for the piezo wires to exit and be attached to an electrical feed-through on one of the chamber ports.

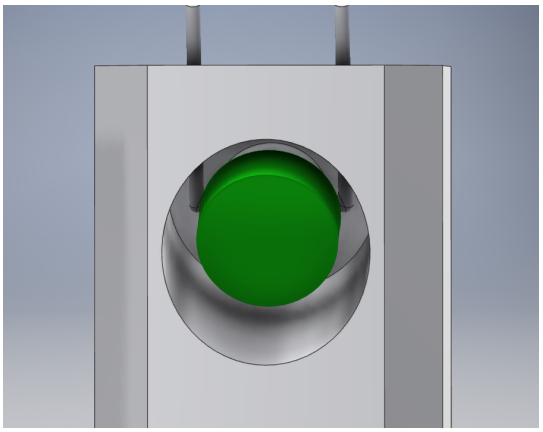

Figure 4.8: Piezo glued onto the back of one of the cavity mirrors. Holes are added for the piezo wires. The cavity mirror is shown in green.

Two piezo options were purchased: PICMA PL033.31 and PD050.31 which are both linear piezos whose respective properties can be observed in table 4.1. These piezos were chosen because: they are small enough to fit into the cavity mounting structure; they are suitable for vacuum conditions and come with vacuum compatible wires attached; and because they have been approved by NASA for space applications due to their consistency (of displacement) after billions of cycles [127]. Each piezo has various advantages and disadvantages. The (slightly) superior travel range and smaller width of the square PL033.31 piezo are advantageous. However the larger size of the PD050.31 ring piezo is beneficial for cavity alignment. This is because, when using a linear piezo, it should cover as much as possible of the (6.3 mm) cavity mirrors as an off centre piezo placement will affect the cavity mirror length. Both piezos will be tested experimentally. If these linear piezos are found to produce insufficient control

for cavity alignment, 3 axis piezos will be investigated. If no small enough 3 axis piezos can be found, alternative methods of moving the mirrors for alignment will have to be included, for example, the kinematic mount discussed below.

Table 4.1: Specifications of the two linear piezo options from PICMA [128, 129]. Where OD = outer diameter, ID = inner diameter, and TH = thickness.

Part	**Type**	**Size [mm]**	**Travel Range [μm]**
PL033.31	Square	3 × 3 × TH 2	2.2
PD050.31	Ring	OD 5 × ID 2.5 × TH 2.45	2

As discussed in section 3.4, the optical cavity is expected to be the most challenging feature of the system to build and optimise. Hence, further design iterations of the cavity mount have already been planned and are discussed subsequently. These changes can be implemented in future if required but were beyond the timescale of this work.

Physical modelling software

If movement of the mirror mounting posts due to vibrations or thermal changes is experimentally found to be problematic then the mount should be modelled using a physical simulation software package, for example, COMSOL [130]. Then the best materials and structural design (e.g. thickness of base, screw placements etc.) could be chosen to minimise movement and shift the vibrational modes to less prohibitive resonant frequencies.

Additive manufacturing

Ideally the cavity mount would be monolithic (single piece) to reduce the post movement, degrees of freedom for alignment, and vacuum complexity. However as previously stated, this could not be machined by the in-house workshop. A future solution could be to 3D print the mount, utilising the research group's existing contacts with UHV 3D printing companies and/or

the materials research group at the University of Birmingham.

Material

Eddy currents induced in the mounting structure due to turning off the magneto-optical trap magnetic field could cause vibrations. Titanium is a weakly magnetic material however if there are still significant vibrations then alternative materials could be investigated e.g. ceramics. Other materials (non-metals) may also be less sensitive to thermal changes.

Kinematic Mount

If the machining tolerance of the mechanical workshop, combined with the piezo motion, is insufficient to be able to accurately align the 4 mirror cavity, then a kinematic mirror mount could be designed and incorporated into the cavity mounting structure. An example of such a mount is shown in figure 4.9 which is a previously machined mount used for a different experiment within the group. It consists of 3 rigid metal layers attached together with screws. 2 hex head screws can be used to adjust the angle of each layer and a set-screw can be used to adjust the layer's distance from the rest of the mount. The mirror can be glued onto the front layer for 3 axis adjustment. To incorporate a similar structure into our cavity mount design, most of the mounting posts could be cut away for the top two mirrors and screw holes could be added. Note that there is only a small space for such a mount and so small screws would have to be used, or perhaps only 2 axis mounting would be available.

4.1.4 2D MOT Chamber

As described in the theory chapter 2.2.1, a 2D MOT will create an atomic beam to load the 3D MOT instead of using a direct atom dispenser. This is necessary to keep the background atomic density low in the 3D MOT chamber which has

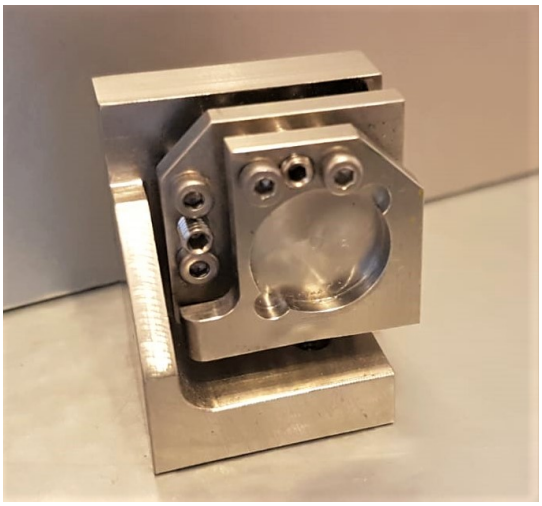

Figure 4.9: Example kinematic mirror mount.

two main advantages. Firstly, a lower background pressure is advantageous to a cold atom cloud as it reduces background collisions. Secondly, a low background pressure is required to keep the high reflectively cavity mirrors clean. This was shown to be necessary in another experiment within the group which used a cavity inside a vacuum but initially loaded from a dispenser: after one month of use the cavity finesse dropped from 2000 to 551 and subsequent cleaning of the cavity mirrors was shown to halve the round trip losses [126]. After implementing a new design loading from a 2D MOT and using a graphite tube (see section 4.1.5), the cavity finesse was maintained for over a year and a half of operation. So that the cavity mirrors are not coated, the atomic beam must be input in the plane perpendicular to the cavity mirrors and at an angle. This angular input can be seen in figure 4.10.

To generate a 2D MOT, a standard 6-way cross can be used. This has 4 viewports for optical access (a 2D MOT requires 2 pairs of counter-propagating cooling beams) and 2 ports which are attached to other parts of the vacuum system. One of these attachment ports is connected to a 4-way cross which contains the atom dispenser and a viewport for the input of a pushing beam.

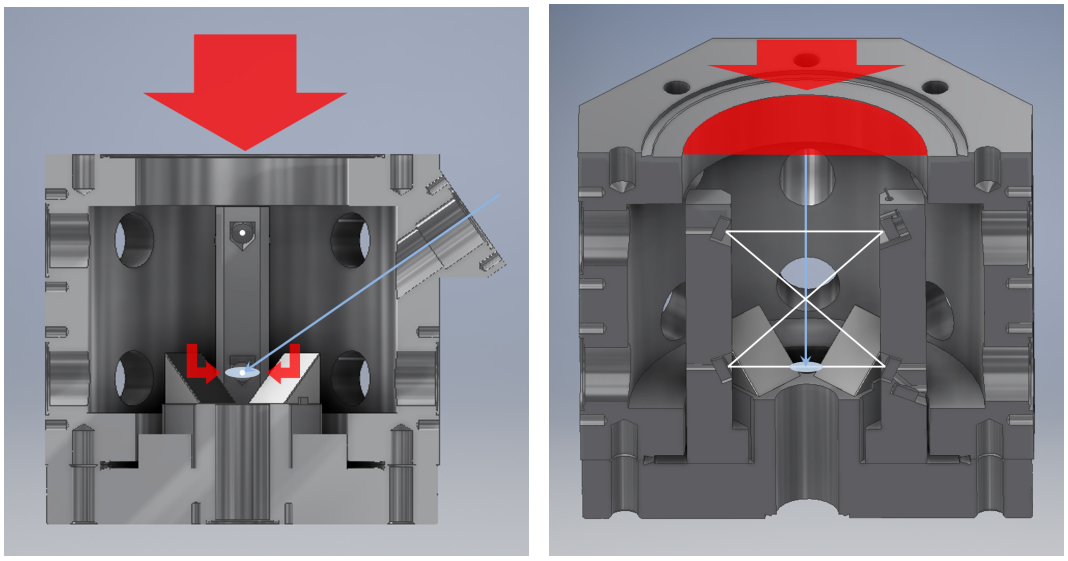

(a) In Plane of 2D MOT **(b)** In Plane of Cavity

Figure 4.10: Schematic showing how the atomic beam generated by the 2D MOT (blue) is input the perpendicular plane to the cavity mirrors. The cavity and 3D MOT beams are shown in white and red respectively. The 3D MOT atom cloud can be seen in blue.

This beam helps direct the atoms from the 2D MOT into the 3D MOT chamber through the other attachment port on the 6-way cross which is connected to a DN16 nipple containing a conductance limiting graphite tube via a DN35-DN16 reducer flange. The graphite tube will be described in detail subsequently. This vacuum arrangement is seen in the vacuum system design shown in figure 4.1.

As previously mentioned, using these standard vacuum parts is relatively fast and simple. However, the 2D MOT beam flux is limited by the cooling length available which is dependant on the beam size which is, in turn, dependant on the available clear view of the viewport. After proof of concept, compactness and atom flux could be improved by using a custom rectangular 2D MOT vacuum chamber design like the one used by Uehlinger at the Swiss Federal Institute of Technology Zurich [93].

The dispenser (SAES RB/NF/7/25/FT) is connected to an electrical feed-

through DN35 port (Kurt J. Lesker EFT0043033) to allow current to pass through it so that rubidium can be input to the vacuum system.

4.1.5 Graphite Tube

To further improve the likelihood of keeping the cavity mirrors clean, the conductance from the 2D MOT to 3D MOT region is reduced using a long graphite tube with a small aperture. This minimises the background atoms that can pass but also acts to select colder atoms from the 2D MOT. This is because atoms with a lower longitudinal velocity spend more time in the cooling volume and, therefore, are trapped closer to the 2D MOT axis (of zero magnetic field gradient).

The graphite tube aperture was set to be 3 mm (inner diameter) by conductance calculations outlined in the next section 4.1.6. The length of the tube was set to be 110 mm to fit inside the DN16 nipple that contains the tube. It must then be checked that the atoms are moving fast enough along the 2D MOT axis to make it out of the graphite tube and into the 3D MOT region before being lost from the beam (e.g. due to the pull of gravity), but are not moving too fast so that they will not be captured in the 3D MOT. As described in section 2.2.1, the finite size of the 3D MOT cooling beams, and hence cooling distance available, sets a maximum limit on the velocity of atom that can be captured. Using equation 2.12, this 'capture velocity' is calculated to be ~ 38 m/s for this system. By resolving the force of gravity perpendicular to the 2D MOT beam axis and using equations of motion, it is found that the maximum time an atom has to pass from (the centre of) the 2D MOT through the graphite tube is 0.023 s. This requires that atoms in the 2D MOT have a starting velocity of $\geqslant 3.38$ m/s which is sufficiently lower than the capture velocity of the 3D MOT. Therefore, a significant amount of the

(∼ Maxwell-Boltzmann distributed) 2D MOT atoms will be capturable by the 3D MOT. Note that a pushing beam will also be used to redirect some of the 2D MOT atoms that are moving away from the 3D MOT, as described in the 2D MOT subsection of section 2.2.1. The additional acceleration created by the pushing beam can be estimated using the equation for the scattering force 2.2.1 and then the power of the beam can be set to ensure that atoms still reach the 3D MOT region with a speed below the maximum capture velocity. Experimentally, the pushing beam power will be varied to optimise/maximise 3D MOT atom number. Note that in space, the movement due to gravity will be negligible and hence a smaller conductance aperture could be used if desired.

The graphite tube has been manufactured by Goodfellow and is shown in figure 4.11. The outer diameter of the graphite is set to 15.5 mm to fit inside the DN16 nipple and it will be held in place by threading the final 15 mm of the tube external which is attached to corresponding thread in the 3D MOT chamber input port as can be seen in figure 4.11 (a).

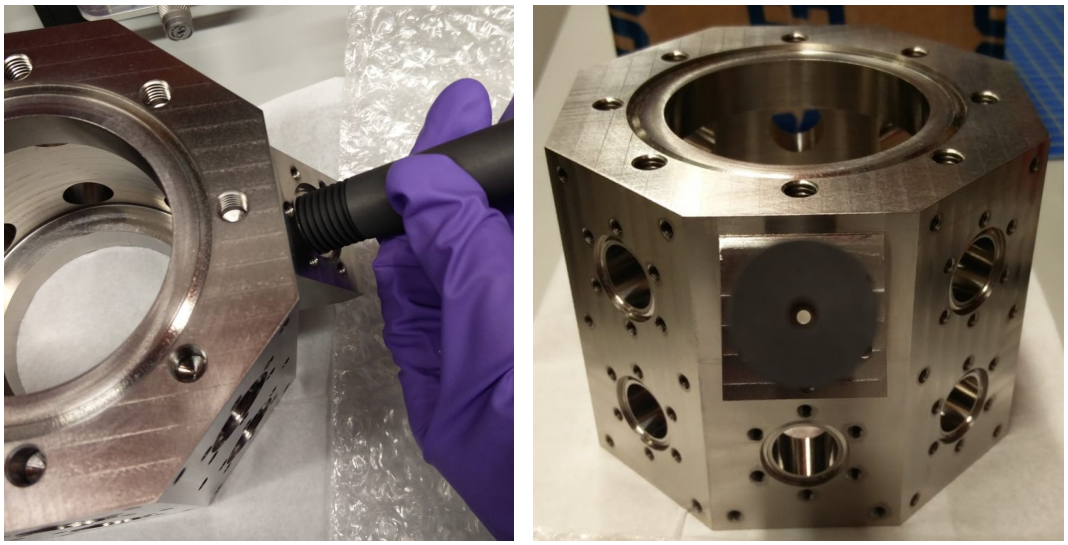

(a) Attaching graphite tube to chamber **(b)** Pinhole that atoms will travel through

Figure 4.11: Demonstrates how a graphite tube is attached to the 3D MOT chamber via external threading.

4.1.6 Pump

A vacuum pump is permanently attached to the system to continuously remove ions and active gases from the chamber. The pump chosen for this experiment was the NEXTorr Z 100 which contains a non-evaporable getter (NEG) for the removal of active gases including background rubidium atoms. This NEG has a pumping speed of $\sim$ 100 L/s (atom/molecule dependent). It also contains a 6 L/s ion pump which removes noble gases and methane that are not pumped by the NEG [131]. To determine the vacuum conditions generated with this pumping speed, conductance calculations were performed.

The pressure, P obtainable in a vacuum chamber is determined by the ratio of the gas load, Q, to the pumping speed, S [132]:

$$P = \frac{Q}{S}. \tag{4.1}$$

In a ultra-high vacuum system, gas loads are created from experimental rubidium atoms, outgassing from internal surfaces, and diffusion through the external walls. The vacuum system was therefore designed to reduce these gas loads. Walls of sufficient thickness can be used to ensure the diffusion is sufficiently small. Outgassing is reduced by using vacuum-compatible materials with low rates and by cleaning and baking (heating) the vacuum system to desorp materials from the internal surfaces and evaporate water.

The throughput, Q, caused by a pressure difference $\Delta P = P_{\text{high}} - P_{\text{low}}$ will be given by:

$$Q = C\Delta P \tag{4.2}$$

where C is the conductance between the two pressure regions which is, in turn,

given by [132]:

$$C = \left(1 + \frac{3L}{8R}\right)^{-1} \frac{\pi}{4} \nu R^2 \tag{4.3}$$

for a tube of length L and radius R where ν is the average gas speed in the system. From this equation it is observed that a longer, narrower tube has smaller conductance than a shorter, wider tube. The smaller the conductance between two regions, the higher achievable pressure difference. However, the conductance also limits the ability of a vacuum pump to remove unwanted particles. Hence, the vacuum pump in this system was attached to one of the DN63 atom interferometry chamber ports (described in section 4.1.7) rather than to the 3D MOT chamber directly as this chamber only had DN16 size ports. The conductance creates an effective pumping speed, S^* of:

$$S^* = \frac{SC}{S + C}. \tag{4.4}$$

Note that for multiple connections in series, the overall conductance is given by:

$$\frac{1}{C_{\text{eff}}} = \frac{1}{C_1} + \frac{1}{C_2} + \frac{1}{C_3} + ... \tag{4.5}$$

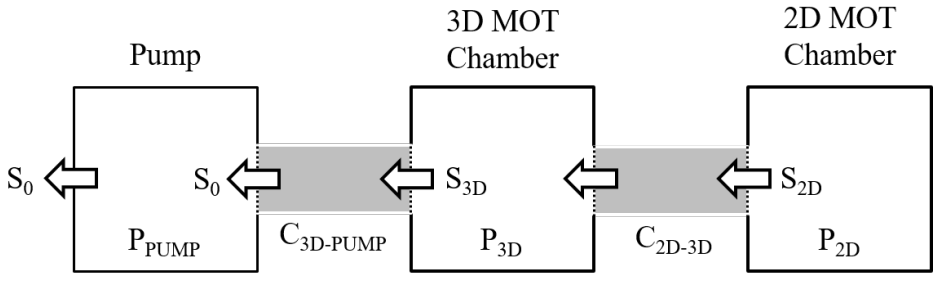

Figure 4.12: Schematic representation of the vacuum system for conductance calculations. See text for further details.

To determine the relevant pressures in our vacuum system, it is represented schematically in figure 4.12 with the 3 key regions being the 2D MOT, the

3D MOT, and the pump (connected to the AI chamber). Referring to figure 4.1, and using the equations outlined above, the pressure ratio between the 2D MOT, P_{2D}, and 3D MOT, P_{3D}, vacuum regions is given by:

$$\frac{P_{\text{2D}}}{P_{\text{3D}}} = \frac{S_0 C_{\text{3D-PUMP}}}{C_{\text{2D-3D}}(S_0 + C_{\text{3D-PUMP}})} + 1 \tag{4.6}$$

where S_0 is the pumping speed at the pump, $C_{\text{3D-PUMP}}$ is the conductance between the pump and the 3D MOT, and $C_{\text{2D-3D}}$ is the conductance between the 2D MOT and 3D MOT regions. The conductance $C_{\text{3D-PUMP}}$ is calculated using the geometry of the DN63 6-way cross that connects the 3D MOT chamber to the pump. Similarly, the conductance $C_{\text{2D-3D}}$ is determined by the dimensions of the graphite tube that connects them, or more accurately, the graphite tube dimensions were set by these calculations to ensure a sufficient pressure difference.

The rubidium dispenser selected will create a background vapour of atoms at a pressure of $\sim 10^{-8}$ mbar in the 2D MOT region (dependent on dispenser current applied). To maintain 'clean' cavity mirrors and minimise background collisions for the cold atoms, a significant pressure ratio between the 2D and 3D MOT regions, $P_{\text{2D}}/P_{\text{3D}}$, will be required. Performing the above calculations and using an initial pumping speed of $S_0 = 100$ L/s gives an effective pumping speed in the 3D MOT chamber of $S_{\text{3D}} = 44$ L/s and equates to a pressure ratio of $P_{\text{2D}}/P_{\text{3D}} = 2459$. Note that maintaining a large pressure difference between two parts of a vacuum system in this way is referred to a 'differential pumping'.

However, this calculation only considers the gas load caused by the background rubidium atoms coming from the 2D MOT chamber: $Q_{\text{2D-3D}}$. When this load has been sufficiently reduced, the outgassing load of the internal vacuum surfaces, Q_{outgas}, becomes relevant and should be taken into account

via:

$$P_{\text{3D}} \approx \frac{Q_{\text{2D-3D}} + Q_{\text{outgas}}}{S_{\text{3D}}} \tag{4.7}$$

The surfaces present in the 3D MOT chamber are: titanium chamber walls and mounting structures; fused silica viewports and cavity mirrors; N-BK7 prisms; a vacuum compatible piezo and wires; 316LN stainless steel electrical feedthrough; and vacuum compatible epoxy for fixing cavity mirrors, prisms, and the piezo. The total outgasing load can be approximated by estimating the surface area of the various materials in the chamber and multiplying it by their respective typical outgassing rates. However, outgassing rates for materials have a significant range depending on baking time, baking temperature, quality of cleaning etc. and most of the values given in literature are for unbaked materials or for a baking time of between 1-24 hours at 100-150 °C. To minimise outgasing, this experiment has a planned bake-out time of several weeks. Furthermore, the coating used on the piezo (to prevent the transmission of water internally) is an unspecified ceramic and the specific epoxy to be used has still to be determined based on testing (see section 3.4). Hence, it is difficult to estimate the outgasing load, Q_{outgas}, that will be present in the 3D MOT chamber. However, a comparison can be made to another 2D-3D MOT experiment in the group with an in-vacuum cavity controlled by a piezo where a finesse of $\sim$ 2,000 was maintained for over a year of dispenser operation by using a conductance limiting graphite tube of similar geometry (diameter = 3 mm, length = 100 mm) [126]. Compared to their experiment, the 3D MOT chamber presented in this thesis contains some additional surfaces including the mounting titanium structures and the reflective glass prisms. However, these materials are highly vacuum compatible and the additional outgassing due to them is expected to be low. The 'dirtiest' element of the vacuum system, is expected to be

the piezo and hence it will be pre-baked before use to reduce its outgassing. If the outgassing in this chamber is found experimentally to be too high (as determined by the cavity finesse reducing over time), then the vacuum will have to be broken periodically to clean the cavity mirrors. This is not ideal for an experiment with a space-based application where long term autonomy is essential. Hence, if necessary, methods to reduce the outgassing can be explored including using a different piezo, attaching a pump with a higher pumping speed, or attaching an additional pump directly to the 3D MOT chamber.

4.1.7 Atom Interferometry Region

The vacuum system requires a 'drop' region where the pre-prepared atoms can free fall for gravimetry. This is entitled the 'atom interferometry' (AI) region which in our system is constructed from a standard DN63 6-way cross, as previously described at the start of the section. To minimise the overall footprint of the system, this is added on the same side as the 2D MOT vacuum parts and the whole system would be inverted (with respect to figure 4.1) for gravity measurements.

4.2 Magnetic Field Generation

As described in section 2.2.1, the 2D and 3D MOTs require 2D and spherical quadrupole magnetic fields respectively to confine the atoms. These will be generated using current carrying coils, rather than permanent magnets, so they can be switched off to allow the cold atom cloud to free fall for gravity measurements.

4.2.1 3D MOT Magnetic Field

The spherical quadrupole field (see section 2.2.1) can be generated with two coils in anti-Helmholtz orientation i.e. with current flowing in opposite directions. The magnetic field gradient created by this coil configuration is approximately linear around the centre, passing through zero. This point of zero magnetic field gradient will define the centre of the 3D MOT because the atoms will be selectively pushed towards this point as described in section 2.2.1. To achieve maximal cooling, this zero point is designed to align with the maximum intensity of the Gaussian light beams which, in this experiment, is determined by the placement (height) of the reflective prisms and the incoming overhead beam. Typically, identical coils (i.e. same number of turns, wire radius, coil geometry etc.) are placed equidistant from the maximum intensity point so that the point of zero magnetic field gradient automatically aligns and the same current can be supplied to both coils. But in this system, the magnetic coils must be placed above and below the bottom layer of viewports of the 3D MOT chamber, so as not to block the optical access, as shown in figure 4.13 (a). However, the maximum light intensity does not occur in the centre of these viewports and, hence, the coils cannot be placed equidistant from this maximum. Therefore, the position of the magnetic field gradient zero, with respect to the coils, must be shifted off-centre to balance this by using a different number of turns in the 2 coils. To simulate this and design the coils, the Biot-Savart law was used to calculate the magnetic field, B_x, at some distance, x, away along the axis of the coil for a coil with n turns, of radius R, and carrying current I:

$$B_x = \frac{\mu_0 n I}{2} \frac{R^2}{(x^2 + R^2)^{\frac{3}{2}}}. \tag{4.8}$$

The total magnetic field for the two coils is simply the summation of their respective fields. The centre of the coils above and below the viewports are x_{above} = 17.8 mm and x_{below} = 23.0 mm from the intensity maximum respectively and this equates to a required number of turns ratio of $n_{\text{above}}/n_{\text{below}} = 0.95$ to align the magnetic field gradient zero point (assuming the same radii and arbitrary current for both coils).

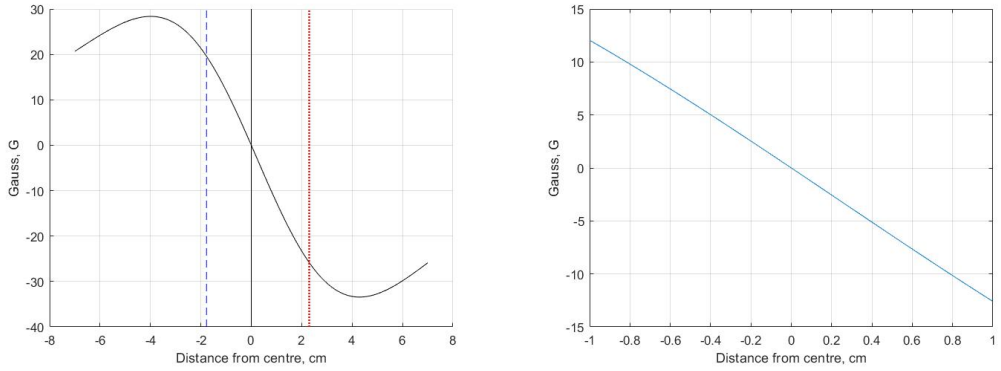

(a) Magnetic Field **(b)** Magnetic Field Around Centre

Figure 4.13: (a) The simulated 3D MOT magnetic field produced by anti-Helmholtz coils where the blue dashed and red dotted vertical lines represent the positions of the centre of the two coils. (b) Zoomed in magnetic field around the 3D MOT centre showing a field gradient of $\sim$ 12 G/cm. The coils have radii of R = 76.25 mm, 285 and 300 turns, and a current of I = 3 A.

A further issue with this magnetic field generation is that, due to the flange mounting design and use of external viewports, the coils require a relatively large radius of R = 76.25 mm to fit around the vacuum chamber. This means that more turns and a higher current are needed to obtain the typical required magnetic field gradient of $\sim$ 10-15 G/cm around the MOT region. However, increasing the turns and current increases the resistance of the coils which generates unwanted heat. To circumvent this problem several steps were taken. Firstly, the mount is designed from metal, rather than 3D printed from plastic, so that it can sustain higher temperatures. This has the additional advantage

of being more rigid, however, a slot has to be cut out of the mount to reduce Eddy currents. Secondly, when winding the coils, thermal paste will be used in-between layers of coils for improved heat dissipation. Thirdly, thicker radius wires will be used to decrease the resistance. To ensure the resistance, Ω, in each coil was low enough, the power, P, was calculated via:

$$P = I^2\Omega = \frac{2I^2\rho nR}{r^2} \tag{4.9}$$

where r is the thickness of the wire and ρ is the resistivity of the wire. A power of $P = 40$ W generates too much heat for in-air coils (i.e. with no additional cooling) and hence the power calculated must be lower than this (ideally < 25 W). Using copper wires with $r = 0.55$ mm and $\rho = 0.0172$ Ωm [133], 285 and 300 turns can be used in the 'above' and 'below' coils respectively to generate the required field gradient at acceptable powers. With a current of $I = 3$ A, a magnetic field gradient of $B \sim 12.3$ G/cm is obtained with powers of $P_{\text{above}} = 22.3$ W and $P_{\text{below}} = 23.5$ W. The exact current used would be determined experimentally by optimising the 3D MOT density whilst keeping the coil heating at acceptable levels.

The mount used to house these coils is shown in figure 4.13 (a). It is made from a mounting structure for the 2 coils and separate pillars to attach this structure to the chamber. This is because the coil mount has to be slid over the chamber from the bottom, after vacuum system assembly, but the required pillar width to attach the mount to the chamber (via screws) is too wide to fit in-between the viewports. The mount will be attached to the pillars via screws. Note that the edges of the mount are filleted to remove any sharp edges that could damage the coil wires.

The bottom coil mount is slightly wider than the top one to match the

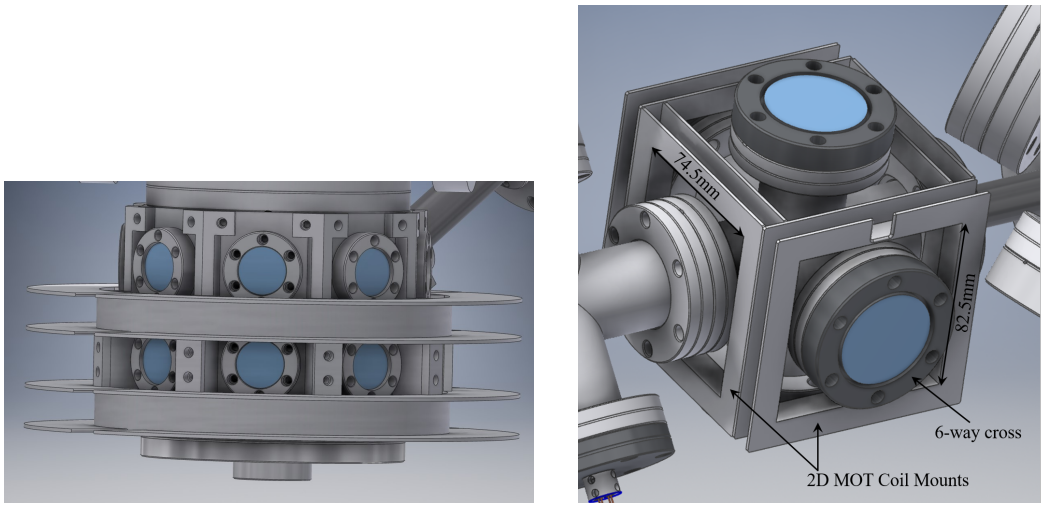

(a) 3D MOT **(b)** 2D MOT

Figure 4.14: 3D and 2D MOT coil structures mounted onto the vacuum system. See text for further details.

additional number of turns required. The top mount is 15 mm wide which fits 12 turns per layer and the bottom mount is 15.8 mm wide which should fit 13 turns per layer so that both coils require 24 layers. With the expected thickness of the wire, the thickness of the coils should be $\leqslant 30$ mm which is the depth of the mounting structure.

Note that, in future iterations of the experiment, the DN16 viewports attached to the chamber could be substituted for inset indium sealed windows. This would reduce the radius of the 3D MOT chamber and therefore coil radius, which would in turn allow for an increased magnetic field gradient, or equivalently, the same field gradient with a lower input current or number of turns. For example, an achievable reduction of coil radius to 70 mm would increase the magnetic field gradient in the MOT region by 3 G/cm to > 15 G/cm.

Compensation Coils

In addition to MOT generation coils, 'compensation coils' are also required. These will be made up of three orthogonal pairs of Helmholtz coils where the current through each pair can be adjusted to cancel the effects of any stray magnetic fields. This is particularly important for the optical dipole trapping stage of the experiment where there will be no trapping field to keep the atoms in place and any stray fields could cause the cloud to veer off in a particular direction. For a space compatible sensor, the experimental region would instead be covered with magnetic shield. This has regularly been done in the research group for mobile, ground based demonstrators.

4.2.2 2D MOT Magnetic Field

For the 2D MOT, four conjoined rectangular coils can be used to generate the 2D quadrupole magnetic field which has a line of zero magnetic field gradient (instead of a point) to which the atoms will be confined. One pair of coils are slightly smaller to fit inside the other: at 74.5×82.5 mm compared to 82.5×82.5 mm length. These coils will be mounted separately around the DN35-6 way cross used to house the 2D MOT as can be seen in figure 4.14 (b). Note that two of the mounts must be fitted whilst assembling the vacuum system and hence these mounts will also be made from metal to withstand vacuum baking temperatures. Similarly to the 3D MOT case, significant space could be saved in future iterations of the experiment by designing a custom 2D MOT chamber and indium sealing rectangular windows to it. This would halve the coil sizes (to $\sim$ 40 mm $\times$ 80 mm) which would again allow for a significant increase in magnetic field gradient or reduction in applied current.

4.3 Optical Delivery: Laser System & Telescopes

A laser system and telescopes must be constructed to provide the optical beams required. One novelty of this experiment is the proposal to use a single laser for the entire ultra-cold atoms generation i.e. for both MOTs and the optical dipole trap. As described in the Atomic Species subsection of 2.2.1, one reason Rb-87 was historically selected over other alkalies for cold atom experiments was because of the existence of readily available lasers and components from the telecommunications industry. These 1560 nm lasers are typically frequency doubled to the 780 nm required for the D_2 cooling transition. In this experiment, the 1560 nm can also be directly input to the optical cavity for the production of the ODT which requires far-detuned light (see section 2.2.2). Note that in telecommunications, 1550 nm is actually typically used, however the lasers and components have sufficient range to be operated effectively at 1560 nm.

Note that, in future, an additional laser system or arm would be required for atom interferometry however this is beyond the scope of this work.

4.3.1 Fibre Laser System

In typical cold atom interferometry, the laser system has a large contribution to the total size and power consumption budget. Hence, it is important to design a compact and efficient laser system, especially for space applications where a low SWaP is essential. To meet these criteria, the laser system will use polarisation maintaining, fibre-coupled components which allows for a flexible and robust set-up compared to free space optomechanics.

A schematic of the laser system to be used can be seen in figure 4.15. The first step is to amplify the output of an external cavity diode laser (ECDL) to ~ 2 W. This can be done using separate components or with a combined laser

module, for example the RIO GRANDE [134]. The light is then split using a 99:1 fibre splitter where the 1% can be used for laser locking and the rest is further split at 75:25 which goes to the cavity-based optical dipole trapping and MOT production respectively. These 3 'arms' of the laser will be detailed subsequently.

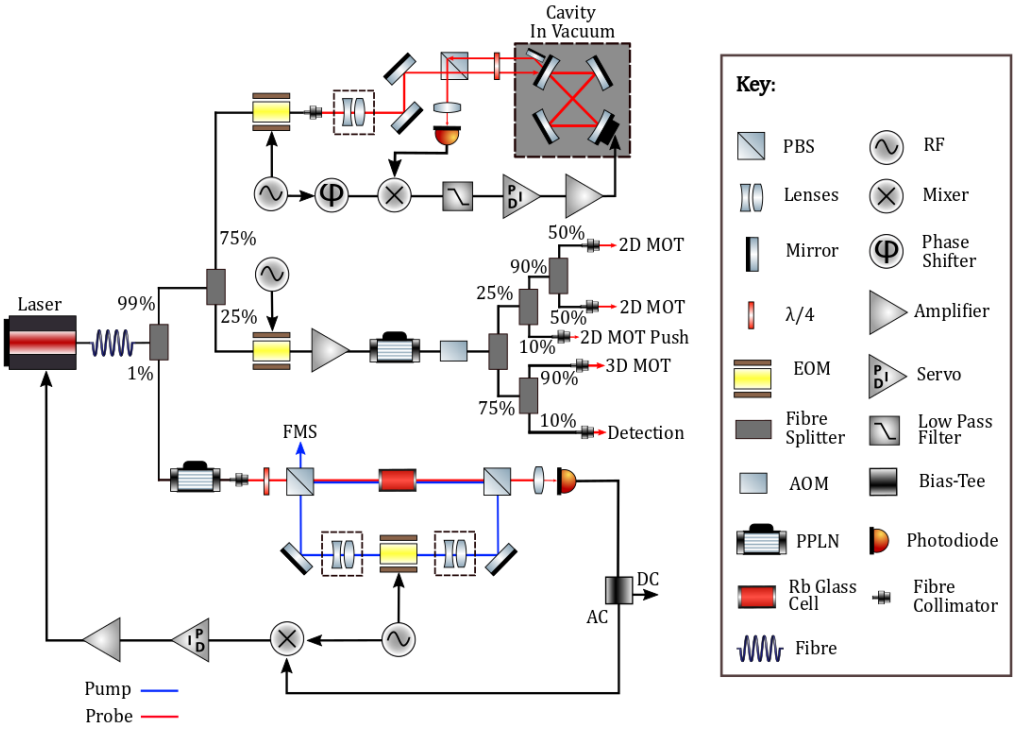

Figure 4.15: Laser system design comprising of 3 main arms used for: laser locking; MOT generation and detection; and cavity-enhanced optical dipole trapping. See the text for further details.

Magneto-Optical Trapping

The MOT arm first passes through an electro-optical modulator (EOM) which is driven by a voltage-controlled oscillator and potentiometer to add a 6.568 GHz sideband to the carrier beam [100]. This is required to re-pump atoms back into the Doppler cooling transition as described in the Atomic Species and Repumping subsection of 2.2.1. An erbium-doped fibre amplifier (EDFA)

then amplifies the light before a periodically-poled lithium-niobate (PPLN) frequency doubler converts it to the required frequency. Experimentally, the frequency output of the ECDL is fine-tuned to resonance by varying the cavity length with the built-in piezo electric actuator. It can then be red-detuned until a MOT is observed in the vacuum system. The ECDL, EDFA, and PPLN can each be controlled via a single USB port. An acousto-optical modulator (AOM) is also used to quickly switch the light on and off as necessary.

Finally, the light is split into the required components for: the 2D MOT cooling beams; the 2D MOT pushing beam; the 3D MOT cooling beam; and detection light. From other experiments in the group using the same (15 mm) prism size and literature based on Rb-87 2D MOTs, powers of approximately: $\gtrsim$ 30 mW; 3-10 mW; 200 mW; and 1 mW are required for the beams respectively [88, 92, 135]. This gives a total power requirement of $\gtrsim$ 250 mW. From the fibre splitter, a power of 400-500 mW is input to this MOT arm, depending on the efficiency of the initial splitters. The typical optical conversion efficiencies of the particular suggested EOM and PPLN to be used are $\sim$ 75% and 55% respectively and therefore, a power of only $\sim$ 150-200 mW would be available without the EDFA, which re-amplifies the light. Using a 1 W EDFA would produce the desired power for this arm. However, experimentally the 2D and 3D MOT conditions that can be obtained without the EDFA should be investigated because, if sufficient parameters (atom number, loading time etc.) can be reached without amplification then this removes one component from the laser system which is advantageous for minimising the SWaP.

Laser Locking

To reduce the frequency variations and drift of the ECDL, one of the laser system arms is dedicated to 'locking' the laser to an external reference. This will be

done using a glass cell containing ^{87}Rb vapour and based on the well-established modulation transfer spectroscopy (MTS) frequency stabilisation technique. This technique generates an electronic 'error' signal which represents the variation of the laser frequency from the atomic transition frequency measured using the glass cell. This signal is fed to the laser's piezo to continuously counteract frequency drifts. Only a small amount of optical power is split into this arm so that the rubidium in the glass cell is not saturated. Further details of the MTS locking method and its advantages can be found in literature [136–138]. Note that, experimentally, a hybrid combined MTS and frequency modulation spectroscopy (FMS) could be used to improve the locking stability [139]. A laser arm will be constructed that is capable of both techniques.

Cavity-Based Optical Dipole Trapping

The final arm of the laser system is used to input light into the optical cavity for optical dipole trapping. Free-space steering mirrors will be used to accurately align the beam into the cavity and lenses can be used to match the size and shape of the beam to a single mode (TEM_{00}) of the cavity. This technique is referred to as 'mode matching' and is described in literature [140].

The well-established Pound-Drever-Hall (PDH) technique [141] will be used to lock the cavity to the stabilised laser source. This involves directing phase modulated light, made up of a carrier and two sidebands, onto the cavity. Light reflected off the cavity is measured by a photodetector and contains the two unchanged sidebands as well as the phase-shifted carrier component. The photodetector signal is then mixed down with a local oscillator, which is in phase with the modulated light. After filtering, an electronic signal is output which represents how far off resonance the cavity is from the laser carrier. This signal can then be used as feedback for stabilisation.

Depending on the efficiency of the fibre splitters, 1200-1500 mW should be initially delivered to this arm of the laser system. From previous calculations in section 3.3.3, a cavity input power on the order of 100 mW is required for sufficient optical dipole trapping depth. The lossiest parts of this arm are expected to be the frequency doubler (PPLN), where $\sim$ half of the power can be lost, and the mode matching. To achieve the desired 100 mW, $\sim$ 20% of the initial light must be coupled into the TEM_{00} cavity mode. With careful alignment, percentages of $>$ 80% can be achieved [126, 142] but cavity and system design constraints in this experiment may reduce this value. Hence, the final power achievable in this arm must be determined experimentally.

4.3.2 Telescopes

The beams coupled out of the fibres need to be magnified, collimated, and polarisation corrected before being directed into the vacuum system. Hence, telescopes were designed for this purpose. Telescopes are required for the 2D and 3D MOT generation as well as for the 2D MOT pushing beam and light detection. All of the optical components were purchased from Thorlabs. Standard lens tube components are chosen for speed and ease. However, as the ultimate application of this work is space-based, in future single body metal telescopes could be constructed with the optics fixed in place using space compatible glues. This builds on heritage from previous experiments in the group.

Pushing Beam

A 2D MOT is radially confined to $\sim$ a few mm and hence a small pushing beam can be generated by simply using a fibre collimator which is a lens pre-packaged to attach directly to the fibre output. The part selected is the F260APC-780

which will collimate the beam to $\sim$ 3 mm. Note that the graphite tube inner diameter, that the 2D MOT atoms have to pass through, is 3 mm and hence this places an upper limit on the push beam size.

Detection

The optical access of the viewport used for detection is 16 mm (see 4.1) and hence this beam diameter is aimed for. To achieve this, a plano-concave and plano-convex lens will be used in tandem to expand and collimate the beam respectively. The required focal lengths can be calculated using simple geometry as illustrated in figure 4.16. According to this, the optical components selected were: a F280APC-780 fibre collimator which creates an initial beam of radius x_1 = 2 mm; LC2969-B plano-concave lens with a focal length f_1 = -6 mm; and LA1951-B plano-convex lens with f_2 = 25 mm. This should result in a final collimated beam radius of x_2 = 8.5 mm as desired. The parts will be held in 1″ lens tube optomechanics.

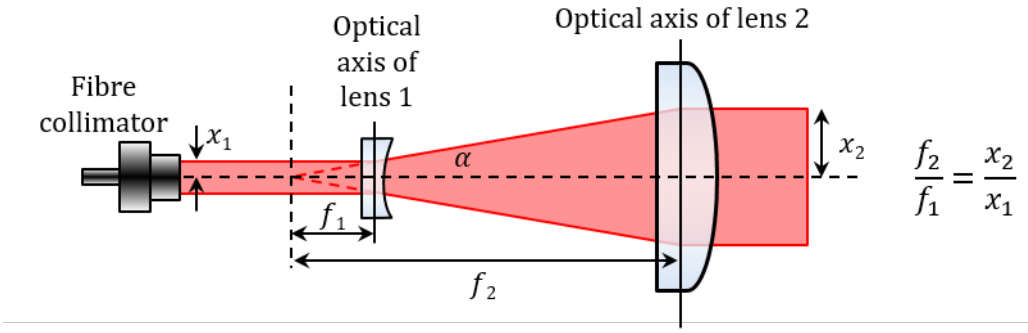

Figure 4.16: Telescope lens geometry used for expanding and collimating fibre outputs. A plano-concave lens with focal length f_1 expands the fibre collimated output of beam radius x_1. A plano-convex lens with focal length f_2 re-collimates the beam to a radius x_2.

Magneto-Optical Trapping

As outlined in the theory section, for the generation of MOTs circularly polarised beams are required. The laser system uses panda-type fibre components which attempt to maintain the $\sim$ linear polarisation output by the ECDL [143]. The first optical component of the MOT telescopes is a linear polariser which removes any non-linearities in the polarisations. The optical axis of this element is aligned with the fibre polarisation axis to maximise light intensity. Next, the light passes through a quarter waveplate whose 'fast-axis' is set at 45° to the optical axis of the polariser so that the light polarisation is converted from linear to circular. After polarisation correction, the beams are expanded and collimated using the plano-concave - plano-convex lens configuration previously described.

The 3D MOT is created using a single overhead Gaussian beam and reflective surfaces. Hence, a beam size of $\gtrsim 48.8$ mm is required to cover the prisms. After using the same fibre collimator and initial expansion lens as in the detector telescope, there are 2 options for the final collimation lens: the LA1145-B or the LA1050-B which have focal lengths of 75 mm and 100 mm respectively. These generate beam diameters of 50 mm and 67 mm respectively. The later, larger beam may be desired so that a higher intensity is incident on the prisms but this beam will be clipped on the 63 mm clear view of the viewport. Both options were purchased and the preferred choice, in terms of MOT atom number, will be found experimentally. The parts will be mounted in 2″ lens tubes.

Finally, for the 2D MOT, 2 pairs of counter-propagating beams are required. To maximise the 2D MOT flux, a large as possible beam size should be used [88]. The beam size is limited by the $\sim$ 35 mm clear view of the viewports however 40 mm beams are designed to cut off the low intensity outer ring

of the Gaussian beam. This is done by using the same fibre collimator and expansion lens as in the 3D MOT and detection telescopes followed by a 60 mm focal length collimating lens (LA1401-B). Again, the parts will be mounted in 2″ lens tubes. Furthermore, 2 retroreflecting prisms (PS976M-B), based on the principle of total internal reflection, were used to reduce the number of telescopes required from 4 to 2. These prisms come pre-mounted in a 2″ lens tube.

All of these telescopes can be seen in place around the vacuum system in figure 4.17 in the final section of this chapter.

4.4 Full Assembly

The CAD assembly of the system design is shown in figure 4.17. This includes the vacuum system, magnetic field coils, telescopes, and a mounting structure to attach this to an optical table. Additional mounting structure may be added to support the pump and 2D MOT region to minimise torque on the vacuum joins. The laser system is not shown. Note that the peripherals are closely fitting on this design i.e. there is little space between the vacuum flanges, telescopes, and coil mounts. This would be improved in future iterations of the experiment where a custom built, rectangular 2D MOT chamber could be used, as previously suggested in section 4.1.4. This would be more compact and could improve the 2D MOT flux due to increased optical access and therefore beam size [88]. All of the components in the figure have been manufactured or purchased and are ready for assembly.

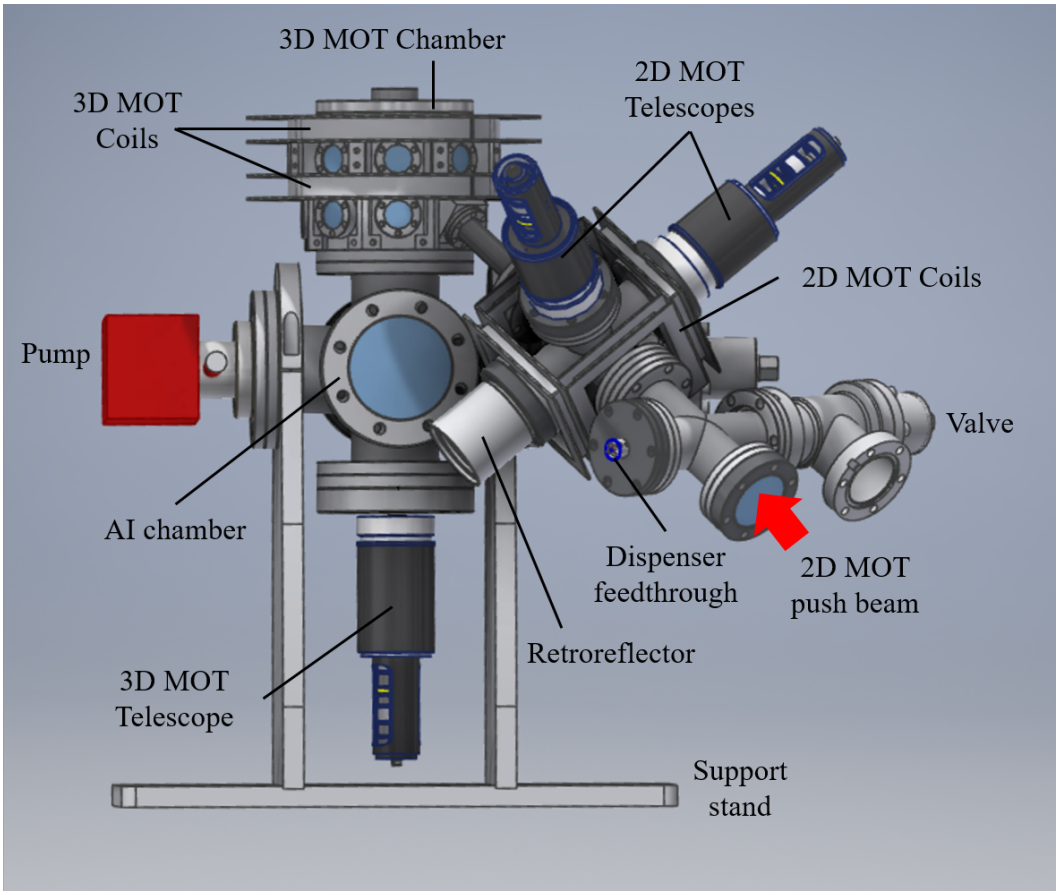

Figure 4.17: 3D CAD design of the full system assembly including vacuum system, magnetic coil mounts, and telescopes.

CHAPTER 5

CONCLUSIONS

5.1 Project Motivation and Goals

In conclusion, this thesis presents the design of a system that aims to prove a novel all-optical method of generating the ultra-cold atoms required for space-based cold atom interferometry. The proposed main application behind a future sensor based on this technology would be for the observation of the Earth's gravitational field for use in climate monitoring and navigation [10–12]. Previously, classical devices have been successfully used for this purpose [27, 30, 31, 33] however the sensitivity limit of these classical technologies is close to being reached [36].

Quantum sensors based on cold atom interferometry are a proposed method of reaching improved gravimetry sensitivity [36, 42]. Atom interferometers use pre-cooled clouds of atoms as the falling test mass for a gravity measurement. These atom interferometers have an advantage when taken to space: the measurement or drop time can be increased by a factor of 10-100 in the microgravity environment. This improves the precision of the gravity measurement, compared to on ground, by orders of magnitude because the sensitivity of a cold atom interferometry is proportional to the interferometry time squared.

However, this also creates a fundamental challenge for this technology: over the increased measurement time, the thermal expansion of the atoms can become problematic and limit the interferometry contrast. Hence, there is a need to pre-cool the atoms to ultra-cold temperatures to minimise expansion.

One of the challenges of obtaining ultra-cold atoms is trapping the atoms whilst further cooling is performed. The most developed technology for this purpose currently uses atom chips which use a hybrid combination of magnetic and optical traps. They are compact and provide fast cooling, however they require a high current to generate the strong magnetic fields required. Also, the atoms have to be trapped close to the chip surface which can limit cloud sizes (a higher atom number is desired for signal-to-noise ratio). Furthermore, magnetic traps have some inherent issues including: atoms must be prepared in specific states for trapping; some atoms cannot be magnetically trapped at all; and there are perturbations when the magnetic field is turned off.

Hence, the work presented in this thesis aims to develop a competitive or complementary technology based on all-optical dipole trapping (ODT) methods. This technique can be used for all states and atoms and therefore could be used for atoms that cannot be magnetically trapped. All-optical traps were historically not chosen because there is a requirement for high optical power. Hence, the focus of this work was to design a novel, low input power, all-optical trapping method of generating ultra-cold atoms.

This experiment will also use a single laser to provide all of the light required for the 2 stage cooling process. Using a single laser would reduce the power and size footprint of the system, which is advantageous for space applications. It would, according to literature, be the first time a single laser has been used for all of these stages in one experiment. However, this single laser system further amplifies the power requirements of the ODT due to the non-optimal

wavelength that must be used for trapping. The solution proposed in this work is to use a reflective optical cavity, inside the vacuum system containing the atoms, to enhance the optical power in the dipole trap. The optical cavity will balance, in real time, travelling wave (single beam) and standing wave (lattice) trapping to optimise the evaporative cooling process for final atom number, temperature, and speed.

Furthermore, this experiment plans to build on heritage in the group of using a compact prism-based pre-cooling magneto-optical trap stage. If successful, this would be the first optical dipole trap and Bose-Einstein condensate loaded from a prism-based MOT.

5.2 Summary of Work Completed

Firstly, ABCD matrix formalisation, set out in chapter 2, was used to model various optical cavities and the optical dipole traps they would generate, in chapter 3. Cavity parameters investigated included: number of mirrors; radius of curvature of mirrors; reflectivities of mirrors; cavity geometries; cavity stabilites; and beam waists. From this modelling, a 4 all-curved-mirror cavity was chosen with equal radii of curvature, $R_i = 75$ mm, reflectance of the input mirror of $r_1^2 = 0.9988$, reflectance of the other mirrors, $r_{2,3,4}^2 = 0.9997$, sagittal (axial) and tangential (radial) beam waists of $w_{0s} = 155$ µm and $w_{0s} = 158$ µm respectively, and corresponding sagittal and tangential stability parameters of -0.04 and 0.43 respectively. Assuming 100 mW is coupled into the cavity, it will generate an initial optical dipole trap depth of 131 µK which should capture ∼5% of the MOT atoms. After evaporative cooling, between 1-10% of these atoms are expected to remain and from this, and the range of possible measurement times in microgravity, an expected gravity sensitivity of between

10^{-8} - 10^{-11} Gal is predicted for this system in a space environment. This improves on the current classical Earth observation sensors by several orders of magnitude and hence, it validates this system for future, high precision space based gravimetry. The cavity mirrors, alignment enabling piezo actuators, and the epoxies proposed to hold everything in place, have been custom purchased and are ready for initial testing.

Furthermore, the rest of the system was designed including the the vacuum system; the magnetic field generating coils; and the laser system and telescopes, as is described in chapter 4. The vacuum system is a multi-chamber system containing a custom conductance limiting tube so that the atom loading region, containing a dense rubidium vapour, is kept separate from the ultra-cold atom preparation chamber. In this chamber a low background is required to keep cavity mirrors clean and to reduce background collisions which can knock atoms out of the trap. This 'differential pumping' stage can maintain a pressure difference of $\sim$ 2,500 however a lower ratio is expected due to outgassing of materials in the vacuum. The ultra-cold atom preparation chamber was custom designed, using 3D CAD software, and built in the in-house mechanical workshop so that the pre-cooled atomic loading beam could be input at a custom angle to maximise loading whilst simultaneously preventing atoms from coating the cavity mirrors. Custom prism and cavity mirror mounting structures were also designed and built and these structures should enable the centres of the magneto-optical trap and optical dipole trap to automatically align for maximum atom transfer. Attached to the preparation chamber is a region where atom interferometry can be performed in future. All of these vacuum parts have been ordered/manufactured, cleaned, and are ready for assembly.

The laser system is designed as 3 main 'arms' responsible for providing the

required light for: atomic beam and magneto-optical trap generation and atom detection; cavity-based optical dipole trapping; and laser locking. It is proposed that a readily available laser, operated at 1560 nm, could be used to provide the ODT beams, and a portion of the light could also be frequency doubled, using off the shelf components, to 780 nm which is the resonant frequency of the D2 transition in Rb-87 and is required for laser cooling. Using this design, a single 2 W laser could provide all of the necessary light beams for the system. To increase the flexibility and robustness of the laser system, it was designed using fibre based components, where possible. This is important for space-based future applications. Telescopes were also designed to couple the light from the fibres to the chamber. These will use standard lens tube components but could be made space-compatible in the future by using single body metal telescopes which builds on heritage previously developed within the group.

5.3 Future Work

The immediate next steps of the project would be to test the epoxies and to build the optical cavity. Once built it would be fully characterised (in terms of finesse, mode image, etc.) both before and after a test-bake to ensure it can withstand high temperatures. As the cavity building, alignment, and testing is expected to take some time, the vacuum system can be built and tested in tandem. A magneto-optical trap can be obtained, characterised (in terms of atom number, temperature etc.), and optimised so that when the cavity is ready and put into the system, work can immediately begin on generating an optical dipole trap (after re-baking the system to maintain low vacuum pressures).

Once the cavity is in the vacuum system, atoms will be transferred to the

optical dipole trap. This transfer process will be optimised (in terms of atom number, temperature etc.) using techniques established in literature. Once in the trap, a standing wave can be generated in the cavity to convert to an optical dipole lattice trap. This will also be characterised before attempting evaporative cooling, ideally to quantum degeneracy. This can be done simply by reducing the intensity of the cavity beams.

In the further term, once this method of ultra-cold atom generation has been demonstrated and optimised, atom interferometry measurements can be attempted. Note that the vacuum system has already been made ready for this purpose however additional laser system components will be required. From the on-ground measurement sensitivity achieved, it can be extrapolated what the sensitivity in the microgravity environment of space would be and this can be compared to existing sensors and other proposed future technologies. If this sensor proved competitive, then work towards qualifying this system for space applications could be made. Where possible, space qualified parts were used in this system. However, as the experiment presented in this thesis is a proof of principle demonstrator, cost and lead-time were prioritised over space compatibility. Hence, in the long-term, significant focus would be put on improving the technology readiness level of this system for space. For this, the SWaP of the system would be minimised by, for example, making more custom vacuum parts out of titanium rather than off-the-shelf stainless steel. Furthermore, existing components could be replaced with similar, space qualified versions, for example the fibre laser system components and optics. This would build on miniaturisation heritage within the group [92]. As well as low SWaP, the system would have to be tested for space-compatibility in terms of vibrations, radiations, and thermal changes and an automated computer control system would be required. The technology readiness level of

the system could therefore be proved step-wise; first in the laboratory, then on space testing platforms, then in a drop tower, next on a parabolic flight etc. Most space-based sensors are proved this way over a significantly long-time scale. However, if the system could be made compact and low power enough, a miniaturised satellite (CubeSat) demonstrator could be attempted which allows for a faster and cheaper launch. This would build on previous heritage in the group [57].

Note that quantum technology proposals have been previously rejected from large scale (ESA and NASA) funding, due to the immaturity of the technology in terms of space qualification. However, this funding is critical because it takes significant time, resources, and iterations to convert a concept into a launchable, space-qualified sensor. Therefore, the ultimate aim of this project is to act a proof-of-principle demonstrator which could secure further funding for future work.

REFERENCES

[1] G. Galilei. *Discourses and Mathematical Demonstrations Relating to Two New Sciences*. 1638.

[2] N. Maskelyne. "An account of observations made on the mountain Schehallien for finding its attraction". In: *Philosophical Transactions of the Royal Society of London* 65 (1775), pp. 500–542. URL: https://doi.org/10.1098/rstl.1775.0050.

[3] H. Cavendish. "Experiments to determine the Density of the Earth". In: *Philosophical Transactions of the Royal Society of London* 88 (1798), pp. 469–526. URL: https://doi.org/10.1098/rstl.1798.0022.

[4] J. H. Poynting. *Mean Density of the Earth*. 1984.

[5] J. Hinderer, D. Crossley, and R. Warburton. "Gravimetric Methods – Superconducting Gravity Meters". In: vol. 3. 2007, pp. 65–122. ISBN: 9780444527486. DOI: 10.1016/B978-044452748-6/00172-3.

[6] T. Niebauer. "Gravimetric Methods – Absolute Gravimeter: Instruments Concepts and Implementation". In: vol. 3. 2007, pp. 43–64. DOI: 10.1016/B978-044452748-6/00055-9.

[7] R. P. Middlemiss et al. "Measurement of the Earth tides with a MEMS gravimeter". In: *Nature* 531.7596 (2016), pp. 614–617. DOI: 10.1038/nature17397. URL: http://eprints.gla.ac.uk/118025/.

[8] M. Nabighian et al. "75th Anniversary - Historical development of the gravity method in exploration". In: *Geophysics* 70 (2005). DOI: 10.1190/1.2133785.

[9] N. Metje et al. "Seeing through the Ground: The Potential of Gravity Gradient as a Complementary Technology". In: *Advances in Civil Engineering* 2011 (2011). DOI: 10.1155/2011/903758.

[10] T. Niebauer et al. "Monitoring earthquakes with gravity meters". In: *Geodesy and Geodynamics* 2 (2011), pp. 71–75. DOI: 10.3724/SP.J.1246.2011.00071.2.

[11] Y. Zhu et al. "Earthquake prediction from China's mobile gravity data". In: *Geodesy and Geodynamics* 6 (2 2015), pp. 81–90. DOI: 10.1016/j.geog.2015.01.002.

[12] M. Charco et al. "Spatiotemporal gravity changes on volcanoes: Assessing the importance of topography". In: *Geophys. Res. Lett* 36 (2009). DOI: 10.1029/2009GL037160.

[13] J. Pritchard, S. Till, et al. *UK Quantum Technology Landscape 2014*. Accessed: 03-04-2020. DSTL. 2014. URL: https://epsrc.ukri.org/newsevents/pubs/dstl-uk-quantum-technology-landscape-2014/.

[14] J. Dowling and G. Milburn. "Quantum Technology: The Second Quantum Revolution". In: *Philosophical transactions. Series A, Mathematical, physical, and engineering sciences* 361 (2003), pp. 1655–74. DOI: 10.1098/rsta.2003.1227.

[15] *UK National Quantum Technologies Programme*. Accessed: 02-04-2020. UKNQTP - UKRI. URL: https://uknqt.ukri.org/.

[16] P. Knight et al. *Blackett Review: The Quantum Age: technological opportunities*. Accessed: 17-12-2019. 2016. URL: https://www.gov.uk/government/publications/quantum-technologies-blackett-review.

[17] *Cerca - Wearable MEG Scanner: A quantum leap in imaging brain function*. Accessed: 01-02-2021. Cerca Magnetics. URL: https://www.cercamagnetics.com/.

[18] *M Squared: Quantum Products*. Accessed: 01-02-2021. M Squared. URL: https://www.m2lasers.com/quantum.html.

[19] *Products: Quantum Technology*. Accessed: 01-02-2021. Telesyne e2v. URL: https://www.teledyne-e2v.com/products/quantum-technology/.

[20] *FG5-X ABSOLUTE GRAVITY METERS*. Accessed: 04-05-2020. Micro g LaCoste. URL: http://microglacoste.com/product/fg5-x-absolute-gravimeter/.

[21] *CG-6 AUTOGRAV GRAVITY METER*. Accessed: 04-05-2020. Scintrex. URL: https://scintrexltd.com/product/cg-6-autograv-gravity-meter/.

[22] B. Altschul et al. "Quantum Tests of the Einstein Equivalence Principle with the STE-QUEST Space Mission". In: *Advances in Space Research* 55 (1 2015), pp. 501–524. URL: https://arxiv.org/pdf/1404.4307.pdf.

[23] L. Badurina et al. "AION: an atom interferometer observatory and network". In: *Journal of Cosmology and Astroparticle Physics* 05 (2020), pp. 011–011. DOI: 10.1088/1475-7516/2020/05/011. URL: https://doi.org/10.1088/1475-7516/2020/05/011.

[24] NASA. *GRACE launch - press kit*. Accessed: 01-06-2020. 2002. URL: https://www.jpl.nasa.gov/news/press_kits/gracelaunch.pdf.

[25] L. Zhang et al. "GRACE-based validation of terrestrial water storage variations as simulated by four different hydrological models". In: *EGU General Assembly 2016, Geophysical Research Abstracts* 19 (2016). URL: https://meetingorganizer.copernicus.org/EGU2016/EGU2016-13303.pdf.

[26] E. Rignot et al. "Acceleration of the contribution of the Greenland and Antarctic ice sheets to sea level rise". In: *Geophysical Research Letters* 38 (5 2011). DOI: 10.1029/2011GL046583.

[27] NASA. *Ocean surface topography*. Accessed: 01-06-2020. URL: https://science.nasa.gov/earth-science/oceanography/physical-ocean/ocean-surface-topography.

[28] A. Buis. *Gravity measurements help melt ice mysteries - NASA, Earth, Mission, News*. Accessed: 20-06-2020. 2007. URL: https://www.nasa.gov/vision/earth/lookingatearth/grace-20070320.html.

[29] N. S. Tkachenko and I. V. Lygin. "Application of the GRACE satellite mission for solving geological and geographic problems". In: *Moscow University Geology Bulletin* 72 (3 2017). URL: https://link.springer.com/content/pdf/10.3103/S0145875217030085.pdf.

[30] R. Rummel, W. Yi, and C. Stummer. "GOCE gravitational gradiometry". In: *Journal of Geodesy* 85 (11 2011). URL: https://link.springer.com/article/10.1007/s00190-011-0500-0.

[31] M. R. Drinkwater et al. "The GOCE gravity mission: ESA's first core Earth explorer". In: *Proceedings of the 3rd International GOCE User Workshop - ESA Special Publication* (2007), pp. 1–8. URL: http://esamultimedia.esa.int/docs/GOCE_3rd_Workshop_Drinkwater_et_al.pdf.

[32] ESA. *New GOCE geoid, ESA Space in Images*. Accessed: 25-07-2020. 2011. URL: http://www.esa.int/spaceinimages/Images/2011/03/New_GOCE_geoid.

[33] NASA. *GRACE-FO*. Accessed: 25-07-2020. URL: https://gracefo.jpl.nasa.gov/.

[34] K. Abich et al. "In-Orbit Performance of the GRACE Follow-on Laser Ranging Interferometer". In: *Phys. Rev. Lett.* 123 (3 2019), p. 031101. DOI: 10.1103/PhysRevLett.123.031101. URL: https://link.aps.org/doi/10.1103/PhysRevLett.123.031101.

[35] K. Ghobadi-Far et al. "GRACE Follow-On Laser Ranging Interferometer Measurements Uniquely Distinguish Short-Wavelength Gravitational Perturbations". In: *Geophysical Research Letters* 47 (2020). DOI: 10.1029/2020GL089445.

[36] K. Bongs, M. Holynski, and Y. Singh. "Ψ in the sky". In: *Nature Physics* 11 (8 2015). DOI: https://doi.org/10.1038/nphys342.

[37] *Space for Europe - Bulletin*. Accessed: 04-05-2020. 2013. URL: https://esamultimedia.esa.int/multimedia/publications/ESA-Bulletin-153/offline/download.pdf.

[38] NASA. *InSight Mission Overview*. Accessed: 19-06-2021. 2002. URL: https://mars.nasa.gov/insight/mission/overview/.

[39] W. Pike et al. "A Silicon Seismic Package (SSP) for Planetary Geophysics". In: 2016.

[40] W. Pike et al. "A broad-band silicon microseismometer with 0.25 NG/rtHz performance". In: *2018 IEEE Micro Electro Mechanical Systems (MEMS)* (2018), pp. 113–116.

[41] S. Tang et al. "A high-sensitivity MEMS gravimeter with a large dynamic range". In: *Microsystems & Nanoengineering* 5 (2019), pp. 1–11. DOI: 10.1038/s41378-019-0089-7.

[42] O. Carraz et al. "A Spaceborne Gravity Gradiometer Concept Based on Cold Atom Interferometers for Measuring Earth's Gravity Field". In: *Microgravity Science and Technology* 26 (3 2014), pp. 139–145. URL: https://link.springer.com/article/10.1007%2Fs12217-014-9385-x.

[43] R. Grimm, M. Weidemüller, and Y. B. Ovchinnikov. "Optical Dipole Traps for Neutral Atoms". In: *Advances in Atomic Molecular and Optical Physics* 42 (2000), pp. 95–170. DOI: 10.1016/S1049-250X(08)60186-X.

[44] S. Herrmann. *QUANTUS - Bose-Einstein condensates in microgravity, ZARM, University of Bremen*. Accessed: 25-07-2020. URL: https://www.zarm.uni-bremen.de/en/research/space-science/experimental-gravitation-and-quantum-optics/projects/quantus.html.

[45] W. Lewoczko-Adamczyk et al. "Rubidium Bose-Einstein Condensate under Microgravity". In: *International Journal of Modern Physics D* 16 (2007), pp. 2447–2454. DOI: 10.1142/9789814261210_0048.

[46] T. van Zoest et al. "Bose-Einstein Condensation in Microgravity". In: 328.5985 (2010), pp. 1540–1543. DOI: 10.1126/science.1189164.

[47] H. Müntinga et al. "Interferometry with Bose-Einstein Condensates in Microgravity". In: *Physical Review Letters* 110.9 (2013). ISSN: 1079-7114. DOI: 10.1103/physrevlett.110.093602.

[48] DRL. *MAIUS 1 – First Bose-Einstein condensate generated in space*. Accessed: 25-07-2020. 2017. URL: https://www.dlr.de/content/en/

articles/news/2017/20170123_maius-1-first-bose-einstein-condensate-generated-in-space_20337.html.

[49] ZARM. *QUANTUS IV - MAIUS*. Accessed: 23-05-2020. URL: https://www.zarm.uni-bremen.de/en/research/space-technologies/space-system-design-and-technologies/projects/quantus-iv-maius.html.

[50] NASA. *NASA's Cold Atom Lab Takes One Giant Leap for Quantum Science*. Accessed: 01-12-2020. 2020. URL: https://www.nasa.gov/feature/jpl/nasas-cold-atom-lab-takes-one-giant-leap-for-quantum-science.

[51] JPL NASA. *The Space Station's Coolest Experiment Gets Astronaut-Assisted Upgrade*. Accessed: 01-12-2020. 2020. URL: https://www.jpl.nasa.gov/news/the-space-stations-coolest-experiment-gets-astronaut-assisted-upgrade.

[52] K. Frye et al. "The Bose-Einstein Condensate and Cold Atom Laboratory". In: *EPJ Quantum Technology* 8.1 (2021). ISSN: 2196-0763. DOI: 10.1140/epjqt/s40507-020-00090-8. URL: http://dx.doi.org/10.1140/epjqt/s40507-020-00090-8.

[53] H. J. Metcalf and P. van der Straten. *Laser Cooling and Trapping*. Springer-Verlag, 1999. 324 pp. ISBN: 9781461214700. DOI: 10.1007/978-1-4612-1470-0.

[54] A. Mosk et al. "Resonator-enhanced optical dipole trap for fermionic lithium atoms". In: *Opt. Lett.* 26.23 (2001), pp. 1837–1839. DOI: 10.1364/OL.26.001837. URL: http://ol.osa.org/abstract.cfm?URI=ol-26-23-1837.

[55] D. Kruse et al. "Cold atoms in a high-Qring cavity". In: *Physical Review A* 67.5 (2003). ISSN: 1094-1622. DOI: 10.1103/physreva.67.051802. URL: http://dx.doi.org/10.1103/PhysRevA.67.051802.

[56] D. S. Naik et al. "Bose–Einstein condensate array in a malleable optical trap formed in a traveling wave cavity". In: *Quantum Science and Technology* 3.4 (2018), p. 045009. DOI: 10.1088/2058-9565/aad48e. URL: https://doi.org/10.1088/2058-9565/aad48e.

[57] D. Devani et al. "Gravity sensing: cold atom trap onboard a 6U CubeSat". In: *CEAS Space Journal* 12 (2020), pp. 539–549. DOI: 10.1007/s12567-020-00326-4.

[58] P. Berman. *Atom Interferometry*. Academic Press, 1996. 478 pp. ISBN: 9780080527680. URL: https://www.elsevier.com/books/atom-interferometry/berman/978-0-12-092460-8.

[59] M. Schmidt. "A mobile high-precision gravimeter based on atom interferometry". PhD thesis. Humboldt University of Berlin, 2011. URL: https://www.physics.hu-berlin.de/en/qom/pdfs/Schmidt2011.pdf.

[60] D. J. Griffiths. *Introduction to Quantum Mechanics*. 2nd ed. Pearson Education, 2005. ISBN: 0131911759. URL: https://www.researchgate.net/publication/327610279_Introduction_to_Quantum_Mechanics.

[61] J. M. McGuirk. "High precision absolute gravity gradiometry with atom inteferometry". PhD thesis. Stanford University, 2001. URL: https://web.stanford.edu/group/kasevich/cgi-bin/wordpress/wp-content/uploads/2012/09/McGuirkThesis.pdf.

[62] J. M. McGuirk et al. "Low-noise detection of ultracold atoms". In: *Optics Letters* 26 (6 2001), pp. 364–366. DOI: 10.1364/OL.26.000364.

[63] G. Santarelli et al. "Quantum Projection Noise in an Atomic Fountain: A High Stability Cesium Frequency Standard". In: *Phys. Rev. Lett.* 82 (23 1999), pp. 4619–4622. DOI: 10.1103/PhysRevLett.82.4619.

[64] Gravitational Observatory Advisory Team. *The ESA–L3 Gravitational Wave Mission - Final Report*. 2016. URL: https://www.cosmos.esa.int/documents/427239/653121/goat-final-rev1.pdf/5b27a845-1948-4c1e-9e38-67bf7156dfe4.

[65] N. Mielec et al. "Atom Interferometry with Top-Hat Laser Beams". In: *Appl. Phys. Lett.* 113 (16 2018). DOI: 10.1063/1.5051663.

[66] E. L. Raab et al. "Trapping of Neutral Sodium Atoms with Radiation Pressure". In: *Phys. Rev. Lett.* 59 (23 1987), pp. 2631–2634. DOI: 10.1103/PhysRevLett.59.2631.

[67] M. H. Anderson et al. "Observation of Bose-Einstein Condensation in a Dilute Atomic Vapor". In: 269.5221 (1995), pp. 198–201. ISSN: 0036-8075. DOI: 10.1126/science.269.5221.198. eprint: https://science.sciencemag.org/content/269/5221/198.full.pdf. URL: https://science.sciencemag.org/content/269/5221/198.

[68] G. K. Campbell and W. D. Phillips. "Ultracold atoms and precise time standards". In: 369 (1953 2011). ISSN: 1471-2962. DOI: https://doi.org/10.1098/rsta.2011.0229.

[69] T. W. Hänsch and A. L. Schawlow. "Cooling of gases by laser radiation". In: *Optics Communications* 13 (1 1975), pp. 68–69. ISSN: 0030-4018. DOI: 10.1016/0030-4018(75)90159-5.

[70] T. W. Hänsch. "Repetitively Pulsed Tunable Dye Laser for High Resolution Spectroscopy". In: *Appl. Opt.* 11.4 (1972), pp. 895–898. DOI: 10.1364/AO.11.000895.

[71] D. J. Wineland, R. E. Drullinger, and F. L. Walls. "Radiation-Pressure Cooling of Bound Resonant Absorbers". In: *Phys. Rev. Lett.* 40 (25 1978), pp. 1639–1642. DOI: 10.1103/PhysRevLett.40.1639.

[72] W. Neuhauser et al. "Optical-Sideband Cooling of Visible Atom Cloud Confined in Parabolic Well". In: *Phys. Rev. Lett.* 41 (4 1978), pp. 233–236. DOI: 10.1103/PhysRevLett.41.233.

[73] S. V. Andreev et al. "Radiative slowing and reduction of the energy spread of a beam of sodium atoms to 15 K in an oppositely directed laser beam". In: *JETP Letters* 38 (8 1981), pp. 442–445. ISSN: 0021-3640.

[74] A. Einstein. "Strahlungs-Emission und Absorption nach der Quantentheorie (Emission and Absorption of Radiation in Quantum Theory)". In: *Deutsche Physikalische Gesellschaft (German Physical Society)* 18 (1916), pp. 318–323.

[75] A. Einstein. "Zur Quantentheorie der Strahlung (The Quantum Theory of Radiation)". In: *Physikalische Zeitschrift (Physical Journal)* 18 (1917), pp. 121–128.

[76] F. Ramirez-Martinez. "Integration of optical components and magnetic field sources in atom chips". PhD thesis. Imperial College London, 2008. URL: https://www.imperial.ac.uk/media/imperial-college/research-centres-and-groups/the-centre-for-cold-matter/public/Fernando-Ramirez-Martinez-(2008).pdf.

[77] P. D. Lett et al. "Observation of Atoms Laser Cooled below the Doppler Limit". In: *Phys. Rev. Lett.* 61 (2 1988), pp. 169–172. DOI: 10.1103/PhysRevLett.61.169.

[78] J. Dalibard and C. Cohen-Tannoudji. "Laser cooling below the Doppler limit by polarization gradients: simple theoretical models". In: *J. Opt. Soc. Am. B* 6.11 (1989), pp. 2023–2045. DOI: 10.1364/JOSAB.6.002023. URL: http://josab.osa.org/abstract.cfm?URI=josab-6-11-2023.

[79] K. J. Weatherhill. "A CO_2 laser lattice experiment for cold atoms". PhD thesis. Durham University, 2007. URL: https://core.ac.uk/download/pdf/6115809.pdf.

[80] C. Burrows. "Repump Methods for Magneto Optically trapped calcium atoms". PhD thesis. University of Strathclyde, 2012. URL: http://photonics.phys.strath.ac.uk/wp-content/uploads/2012/07/ChrisBurrows.pdf.

[81] SAES Group. *Alkali Metal Dispensers - Brochure*. Accessed: 08-10-2020. 2007. URL: https://www.saesgetters.com/sites/default/files/AMD%20Brochure_0.pdf.

[82] J. P. Burke and J. L. Bohn. "Ultracold scattering properties of the short-lived Rb isotopes". In: *Phys. Rev. A* 59 (2 1999), pp. 1303–1308. DOI: 10.1103/PhysRevA.59.1303.

[83] D. W. Sesko, T. G. Walker, and E. C. Wieman. "Behavior of neutral atoms in a spontaneous force trap". In: *J. Opt. Soc. Am. B* 8.5 (1991), pp. 946–958. DOI: 10.1364/JOSAB.8.000946. URL: http://josab.osa.org/abstract.cfm?URI=josab-8-5-946.

[84] W. Ketterle et al. "High densities of cold atoms in a dark spontaneous-force optical trap". In: *Phys. Rev. Lett.* 70 (15 1993), pp. 2253–2256. DOI: 10.1103/PhysRevLett.70.2253. URL: https://link.aps.org/doi/10.1103/PhysRevLett.70.2253.

[85] C. G. Townsend et al. “Phase-space density in the magneto-optical trap”. In: *Phys. Rev. A* 52 (2 1995), pp. 1423–1440. DOI: 10.1103/PhysRevA.52.1423. URL: https://link.aps.org/doi/10.1103/PhysRevA.52.1423.

[86] Lan-Sheng Yang et al. “Loading and Compression of a Large Number of Rubidium Atoms Using a Semi-Dark Type Magneto-Optical Trap”. In: *Chinese Journal of Physics - CHIN J PHYS* 45 (Dec. 2007).

[87] G. L. Gattobigio et al. “Scaling laws for large magneto-optical traps”. In: *Physica Scripta* 81.2 (2010), p. 025301. DOI: 10.1088/0031-8949/81/02/025301. URL: https://doi.org/10.1088/0031-8949/81/02/025301.

[88] J. Schoser et al. “Intense source of cold Rb atoms from a pure two-dimensional magneto-optical trap”. In: *Phys. Rev. A* 66 (2 2002), p. 023410. DOI: 10.1103/PhysRevA.66.023410. URL: https://link.aps.org/doi/10.1103/PhysRevA.66.023410.

[89] J. L. Bliss et al. “Generation of a cold atom beam from a pyramidal magneto-optical trap”. In: *Technical Digest. Summaries of Papers Presented at the Quantum Electronics and Laser Science Conference*. 1999, pp. 73–. DOI: 10.1109/QELS.1999.807319.

[90] J. J. Arlt et al. “A pyramidal magneto-optical trap as a source of slow atoms”. In: *Optics Communications* 157.1 (1998), pp. 303–309. ISSN: 0030-4018. DOI: https://doi.org/10.1016/S0030-4018(98)00499-4. URL: https://www.sciencedirect.com/science/article/pii/S0030401898004994.

[91] K. I. Lee et al. “Single-beam atom trap in a pyramidal and conical hollow mirror”. In: *Opt. Lett.* 21.15 (1996), pp. 1177–1179. DOI: 10.1364/OL.

21.001177. URL: http://ol.osa.org/abstract.cfm?URI=ol-21-15-1177.

[92] A. Hinton et al. "A portable magneto-optical trap with prospects for atom interferometry in civil engineering". In: *Philosophical Transactions of The Royal Society A Mathematical Physical and Engineering Sciences* 375 (2017), p. 20160238. DOI: 10.1098/rsta.2016.0238.

[93] T. Uehlinger. "A 2D Magneto-Optical Trap as a High-Flux Source of Cold Potassium Atoms". Institute for Quantum Electronics, Swiss Federal Institute of Technology Zurich, 2008.

[94] S. Chu et al. "Experimental Observation of Optically Trapped Atoms". In: *Phys. Rev. Lett.* 57 (3 1986), pp. 314–317. DOI: 10.1103/PhysRevLett.57.314.

[95] A. F. J. Levi. *Chapter 5: The Lorentz oscillator model*. Morgan & Claypool Publishers, 2016. ISBN: 978-1-6817-4413-1. DOI: 10.1088/978-1-6817-4413-1ch5. URL: http://dx.doi.org/10.1088/978-1-6817-4413-1ch5.

[96] W. T. Silfvast. 2nd ed. Cambridge University Press, 2004. ISBN: 0521541050.

[97] V. L. Allen and J. H. Eberly. John Wiley and Sons LTD, 1975. ISBN: 9780486136172. URL: https://www.osti.gov/biblio/7365050.

[98] C. Cohen-Tannoudji, J. Dupont-Roc, and G. Grynberg. Wiley, 1992. ISBN: 978-3-527-61719-7. DOI: https://doi.org/10.1063/1.2809840.

[99] I. I. Sobelman. 1st ed. Springer Series in Chemical Physics 1. Springer-Verlag Berlin Heidelberg, 1979, p. 308. ISBN: 978-3-662-05905-0.

[100] D. A. Steck. *Rubidium 87 D Line Data*. Accessed: 05-11-2020. 2001. URL: https://steck.us/alkalidata/rubidium87numbers.1.6.pdf.

[101] S. J. M. Kuppens et al. "Loading an optical dipole trap". In: *Phys. Rev. A* 62 (1 2000), p. 013406. DOI: 10.1103/PhysRevA.62.013406. URL: https://link.aps.org/doi/10.1103/PhysRevA.62.013406.

[102] O. J. Luiten, M. W. Reynolds, and J. T. M. Walraven. "Kinetic theory of the evaporative cooling of a trapped gas". In: *Phys. Rev. A* 53 (1 1996), pp. 381–389. DOI: 10.1103/PhysRevA.53.381. URL: https://link.aps.org/doi/10.1103/PhysRevA.53.381.

[103] Abraham J. Olson, Robert J. Niffenegger, and Yong P. Chen. "Optimizing the efficiency of evaporative cooling in optical dipole traps". In: *Phys. Rev. A* 87 (5 2013), p. 053613. DOI: 10.1103/PhysRevA.87.053613. URL: https://link.aps.org/doi/10.1103/PhysRevA.87.053613.

[104] P. Debs J.and Altin et al. "Cold atom gravimetry with a Bose-Einstein Condensate". In: *Physical Review. A* 84 (Nov. 2010), p. 033610. DOI: 10.1103/PhysRevA.84.033610.

[105] T. Kinoshita, T. Wenger, and D. S. Weiss. "All-optical Bose-Einstein condensation using a compressible crossed dipole trap". In: *Phys. Rev. A* 71 (1 2005), p. 011602. DOI: 10.1103/PhysRevA.71.011602. URL: https://link.aps.org/doi/10.1103/PhysRevA.71.011602.

[106] J.-F. Clément et al. "All-optical runaway evaporation to Bose-Einstein condensation". In: *Physical Review A* 79.6 (2009). ISSN: 1094-1622. DOI: 10.1103/physreva.79.061406. URL: http://dx.doi.org/10.1103/PhysRevA.79.061406.

[107] N. Hodgson and H. Weber. *Optical Resonators: Fundamentals, Advanced Concepts and Applications*. Springer, 1997. ISBN: 3540761373. DOI: 10.1007/978-1-4471-3595-1.

[108] Thorlabs. *Fabry-Perot Tutorial*. Accessed: 10-10-2020. URL: https://www.thorlabs.com/tutorials.cfm?tabID=E9D2D96F-1EFD-4EF0-BB17-FA2CA60F8A8D.

[109] W. Nagourney. *Quantum Electronics for Atomic Physics and Telecommunication*. Oxford graduate texts. Oxford University Press, 2014. ISBN: 9780199665488. URL: https://books.google.co.uk/books?id=YDOTAwAAQBAJ.

[110] H. Kogelnik and T. Li. "Laser Beams and Resonators". In: *Appl. Opt.* 5.10 (1966), pp. 1550–1567. DOI: 10.1364/AO.5.001550.

[111] J. R. Pierce. *Theory and Design of Electron Beams*. Bell Telephone Laboratories series. 1954. URL: https://books.google.co.uk/books?id=iR9RAAAAMAAJ.

[112] L. Mudarikwa. "Cold Atoms in a Ring Cavity". PhD thesis. University of Birmingham, 2015. URL: https://etheses.bham.ac.uk/id/eprint/5843/.

[113] E. T. Jaynes and F. W. Cummings. "Comparison of quantum and semiclassical radiation theories with application to the beam maser". In: *Proceedings of the IEEE* 51.1 (1963), pp. 89–109. DOI: 10.1109/PROC.1963.1664.

[114] A. Lamb. "Cold Atom Gravity Gradiometer for Field Applications". PhD thesis. University of Birmingham, 2018.

[115] L. Earl. "A Compact and Portable Atom Interferometry System:PhD Thesis". 2020.

[116] W. Petrich et al. "Behavior of atoms in a compressed magneto-optical trap". In: *J. Opt. Soc. Am. B* 11 (8 1994), pp. 1332–1335. DOI: 10.1364/JOSAB.11.001332.

[117] H. J. Williams et al. "Characteristics of a magneto-optical trap of molecules". In: *New J. Phys.* 19 (2017). DOI: 10.1088/1367-2630/aa8e52.

[118] M. T. DePue et al. "Transient compression of a MOT and high intensity fluorescent imaging of optically thick clouds of atoms". In: *Optics Communications* 180 (1-3 2000), pp. 73–79. DOI: 10.1016/S0030-4018(00)00701-X.

[119] G. Croft. "Investigating and Comparing Atomic Loading Methods of a 3D Prism Magneto-Optical Trap: Masters Thesis". 2016.

[120] LewVac. *Viewports and Glass Components Catalogue*. Accessed: 01-12-2020. URL: https://www.lewvac.co.uk/download-pdf-catalogues/.

[121] M. Cadoret et al. "Combination of Bloch Oscillations with a Ramsey-Bordé Interferometer: New Determination of the Fine Structure Constant". In: *Physical Review Letters* 101.23 (2008). ISSN: 1079-7114. DOI: 10.1103/physrevlett.101.230801. URL: http://dx.doi.org/10.1103/PhysRevLett.101.230801.

[122] EPOTEK. *Glass Transition Temperature for Epoxies*. Accessed: 05-03-2021. URL: https://www.epotek.com/docs/en/Related/Tech%20Tip%2023%20Tg%20%E2%80%93%20Glass%20Transition%20Temperature%20for%20Epoxies.pdf.

[123] EPOTEK. *Cure Matters: Determining the Proper Cure Schedule*. Accessed: 05-03-2021. URL: https://www.epotek.com/wp-content/uploads/2021/01/Cure-Matters.pdf.

[124] EPOTEK. *EPO-TEK Low Outgassing Adhesives Brochure*. Accessed: 04-03-2021. URL: https://www.galindberg.se/media/1440/low-outgassing-brochure.pdf.

[125] EPOTEK. *EPO-TEK Optical Epoxy Selector Guide*. Accessed: 04-03-2021. URL: https://gentec-benelux.com/wp-content/uploads/2012/07/Epotek-Optical-Selector.pdf.

[126] R. A. Culver. "Collective strong coupling of cold potassium atoms in an optical ring cavity". University of Birmingham, 2017. URL: https://etheses.bham.ac.uk/id/eprint/7319/.

[127] PICMA. *Highly Reliable Multilayer Piezo Actuators: Suitable for Use in Space*. Accessed: 04-01-2021. URL: https://www.piceramic.com/en/piezo-technology/picma/.

[128] PICMA. *PICMA Chip Actuators: PL0xx Datasheet*. Accessed: 04-01-2021. URL: https://static.piceramic.com/fileadmin/user_upload/physik_instrumente/files/datasheets/PL0xx_Datasheet.pdf.

[129] PICMA. *Round PICMA Chip Actuators: PD0xx Datasheet*. Accessed: 04-01-2021. URL: https://static.piceramic.com/fileadmin/user_upload/physik_instrumente/files/datasheets/PD0xx-Datasheet.pdf.

[130] COMSOL. *Simulate real-world designs, devices, and processes with multiphysics software from COMSOL*. Accessed: 05-01-2021. URL: https://uk.comsol.com/?.

[131] SAES. *NEXTORR NEG - ION COMBINATION PUMP, NEXTorr Z 100 Datasheet*. Accessed: 05-01-2021. URL: https://www.saesgetters.com/products/nextorr-pumps.

[132] J. F. O'Hanlon. *A User's Guide to Vacuum Technology*. 2nd ed. Wiley, 1988. Chap. 1. ISBN: 0-471-27052-0.

[133] pro-power. *Enamelled Copper Wire Datasheet*. Accessed: 06-03-2021. URL: http://www.farnell.com/datasheets/2353651.pdf.

[134] RIO. *GRANDE 1550 nm High Power Laser Module*. Accessed: 06-02-2021. URL: https://rio-lasers.com/1550-nm-high-power-laser-module/.

[135] K. Dieckmann et al. "Two-dimensional magneto-optical trap as a source of slow atoms". In: *Phys. Rev. A* 58 (5 1998), pp. 3891–3895. DOI: 10.1103/PhysRevA.58.3891. URL: https://link.aps.org/doi/10.1103/PhysRevA.58.3891.

[136] Heung-Ryoul Noh et al. "Modulation transfer spectroscopy for 87Rb atoms: theory and experiment". In: *Opt. Express* 19.23 (2011), pp. 23444–23452. DOI: 10.1364/OE.19.023444. URL: http://www.opticsexpress.org/abstract.cfm?URI=oe-19-23-23444.

[137] J. H. Shirley. "Modulation transfer processes in optical heterodyne saturation spectroscopy". In: *Opt. Lett.* 7.11 (1982), pp. 537–539. DOI: 10.1364/OL.7.000537. URL: http://ol.osa.org/abstract.cfm?URI=ol-7-11-537.

[138] D. J. McCarron, S. A. King, and S. L. Cornish. "Modulation transfer spectroscopy in atomic rubidium". In: *Measurement Science and Technology* 19.10 (2008), p. 105601. DOI: 10.1088/0957-0233/19/10/105601. URL: https://doi.org/10.1088/0957-0233/19/10/105601.

[139] Fei Zi et al. "Laser frequency stabilization by combining modulation transfer and frequency modulation spectroscopy". In: *Appl. Opt.* 56.10 (2017), pp. 2649–2652. DOI: 10.1364/AO.56.002649. URL: http://ao.osa.org/abstract.cfm?URI=ao-56-10-2649.

[140] D. Z. Anderson. "Alignment of resonant optical cavities". In: *Appl. Opt.* 23.17 (1984), pp. 2944–2949. DOI: 10.1364/AO.23.002944. URL: http://ao.osa.org/abstract.cfm?URI=ao-23-17-2944.

[141] R. W. P. Drever et al. "Laser Phase and Frequency Stabilization Using an Optical Resonator". In: *Appl. Phys. B* 31 (1983), pp. 97–105. URL: https://link.springer.com/article/10.1007/BF00702605.

[142] M. Bader et al. "Efficient coupling to an optical resonator by exploiting time-reversal symmetry". In: *New Journal of Physics* 15.12 (2013), p. 123008. DOI: 10.1088/1367-2630/15/12/123008. URL: https://doi.org/10.1088/1367-2630/15/12/123008.

[143] Thorlabs. *Polarization-Maintaining Single Mode Optical Fiber*. Accessed: 06-03-2021. URL: https://www.thorlabs.com/newgrouppage9.cfm?objectgroup_id=1596.